Quantitative Optical Sensing for Non-Invasive Clinical Characterization of Biological Tissues

by

William Robert Lloyd III

A dissertation submitted in partial fulfillment
of the requirements for the degree of
Doctor of Philosophy
(Biomedical Engineering)
in The University of Michigan
2014

Doctoral Committee:

Professor Mary-Ann Mycek, Chair
Professor Stephen E. Feinberg
Professor James M. Scheiman
Professor Zhen Xu

Dedication

In loving memory of my father, William Robert Lloyd II.

Acknowledgements

This dissertation was made possible with the help and support of many people. First, I thank my dissertation advisor Prof. Mary-Ann Mycek. You provided me with an opportunity to pursue graduate studies, completing a dream I did not know possible. You helped me become an experimental scientist, encouraged my independent thinking, and pushed me to address problems in full. I am a scientist today because of your tutelage. Second, I thank all of my committee members and the collaborators of the Mycek Lab: Dr. Jim Scheiman, you provided endless support, encouragement, and passion as I learned and pursued clinical data collection; Dr. Stephen Feinberg, you showed me what true passion means as a scientist and a clinician; and Dr. Zhen Xu, your excitement for the work presented in this dissertation made me even more excited to get back into the lab and perform more studies.

There are also many more collaborators of the Mycek lab to thank, including Dr. Michael Morris, Dr. Cynthia Marcelo, Dr. Shiuhyang Kuo, Dr. H. Myra Kim, Dr. Roderick Kim, Dr. Hiroko Kato, Dr. Diane Simeone, Dr. Barbara McKenna, Dr. Ahren Rittershaus, Sheryl Korsnes, Dr. Michael Mulholland, Dr. Kevin Nguyen, Dr. Rebecca Minter, Dr. Jeremy Taylor, Dr. Oliver Lee, Dr. Greg Gillispie, and Kurt Peterson. I thank all of my fellow lab mates, including Dr. Robert Wilson, Dr. Malavika Chandra, Dr. Ching-Wei Chang, Leng-Chun Chen, Sakib Elahi, Seung Yup Lee, Emma Salomonsson, Kehan Zhang, and Wenbo Wang.

I thank those who helped me develop as a teacher, including Dr. Rachael Schmedlen, Dr. Tershia Pinder-Grover, Dr. Shanna Daly, the CRLT staff, and my fellow ETCs.

I thank those who helped me pursue an education not only in creativity and innovation, but also in business: Dr. Jeff DeGraff, Staney DeGraff, Dr. Michael Tschirhart, and Sarah Hussong.

This dissertation would not have been possible without the love and support of my mother, my grandparents, my family, my friends, and in particular, my wife. My family has been the solid foundation needed to support crazy dreams and make help make them a reality. My wife has been my best friend and the ever present support system needed through the ups and downs of this dissertation work. Thank you all from the bottom of my heart.

Today is a good day.

Funding Acknowledgements

Chapter 1

This work was supported in part by the National Institutes of Health (NIH R01-DE-019431), the Wallace H. Coulter Foundation (to M.-A. M.), and the U.S. Department of Education (GAANN Fellowship to W.R.L).

Chapter 2-4

This work was supported in part by the National Institutes of Health (NIH CA-114542), the National Pancreas Foundation, the Wallace H. Coulter Foundation, the U.M. Comprehensive Cancer Center, and grants from the U.M. Medical School Translational Research Program and the American Society for Gastrointestinal Endoscopy.

Chapter 5

The project was supported in part by National Institutes of Health grants R43-EB-007866 (to G. D. G. and M.-A. M.) and R01-CA-114542 (to M.-A. M.) and by grant 08-48 from the Montana Board of Research and Commercialization Technology (to G. D. G.).

Chapter 6

This work was supported in part by U.S. National Institutes of Health (R01-DE-019431, to M.-A.M. and S.E.F.) and U.S. Department of Education (GAANN Fellowship, to W.R.L. and S.F.E.).

Chapter 7

This work was supported in part by the National Institutes of Health (NIH R01-DE-019431), the Wallace H. Coulter Foundation (to M.-A. M.), and the U.S. Department of Education (GAANN Fellowship to W.R.L).

Table of Contents

Dedication ii

Acknowledgements iii

Funding Acknowledgements v

List of Figures xiv

List of Tables xxiii

Abstract xxiv

Chapter 1. Introduction 1

1.1 Optical spectroscopy 1

1.2 Clinical and biological measurement challenges that reflectance spectroscopy is suited to address 2

1.2.1 Technical implementation of reflectance spectroscopy 2

1.3 Clinical and biological measurement challenges that fluorescence spectroscopy is suited to address 4

1.3.1 Technical implementation of fluorescence spectroscopy 4

1.4 Experimental design for reflectance and fluorescence spectroscopy 8

1.4.1 Excitation source 8

1.4.2 Emission detector 10

1.4.3 Optical sample properties 10

1.4.4 Additional experimental considerations 13

1.4.5 Environmental conditions 14

1.4.6 Background artifacts – absorption and fluorescence 14
1.4.7 Temperature, pH, and oxygenation 15
1.4.8 Spectroscopic optical data 15
1.4.9 Fiber-optic probe spectroscopy 20
1.4.10 Example Applications 29
1.4.11 Clinical need for non-invasive optical diagnostics 29
1.5 Dissertation Objectives 30
1.6 Dissertation Overview 32
Chapter 2. Verification and validation of a photon-tissue interaction model..... 33
2.1 Introduction 33
2.2 Experimental methods 36
2.2.1 Prototype instrumentation 36
2.2.2 Tissue-simulating phantom measurements with two fiber-optic probes 37
2.2.3 Clinical human pancreatic tissue data acquisition protocol, histopathological "gold standard," data pre-processing, and data exclusion 37
2.3 Photon-Tissue Interaction (PTI) model 39
2.3.1 Semi-empirical reflectance equations 39
2.3.2 Calibration of PTI model for different fiber-probe properties 42
2.3.3 Verification of PTI model with tissue-simulating phantom measurements 43
2.3.4 Effect of scattering parameters on PTI reflectance model of human pancreatic tissues 46
2.4 Consistency of PTI model of human pancreatic tissue when blood concentration varies…… 49

2.4.1 Degree of difference between repeated measurements at each human pancreatic tissue site 49

2.4.2 Procedure to fit PTI model to measured human pancreatic tissue reflectance spectra..... 50

2.4.3 Consistency of scattering properties extracted from repeated measurements at each human pancreatic tissue site 50

2.4.4 Potential for clinical diagnostic significance 54

2.5 Conclusions..... 55

Chapter 3. *In vivo* optical spectroscopy for improved detection of pancreatic adenocarcinoma: a feasibility study 56

3.1 Introduction..... 56

3.2 Clinical optical spectroscopy measurements of *in vivo* human pancreatic tissues 58

3.2.1 Reflectance and Fluorescence Lifetime Spectrometer (RFLS) 58

3.2.2 *In vivo* and *ex vivo* data collection protocol..... 59

3.2.3 In vivo optical data set 60

3.3 Steady-state reflectance spectroscopy analysis..... 61

3.4 Feasibility of optical spectroscopy on human pancreatic tissues *in vivo*..... 61

3.5 Optical reflectance differences between normal and adenocarcinoma tissues *in vivo*..... 62

3.6 Quantitative reflectance analysis with spectral ratios classifier and PTI model.... 63

3.7 Discussion and conclusions 64

Chapter 4. Improved detection of pancreatic disease with time-resolved fluorescence spectroscopy 66

4.1 Introduction 66
4.2 Materials and Methods 67
4.2.1 Clinically-compatible time-resolved fluorescence spectrometer 67
4.2.2 Optical Data Set 68
4.2.3 Data Pre-Processing and Exclusion Criteria 69
4.2.4 Time-resolved fluorescence analysis methods 70
4.3 Tissue classification protocol 71
4.3.1 Calculating average fluorescence decay parameters for each measured site 71
4.3.2 Statistical analysis tests independence of tissue types 71
4.3.3 Multinomial logistic analysis 71
4.3.4 Receiver operating characteristic curves 72
4.3.5 Method to compute classification results 72
4.4 Results 73
4.4.1 Average fluorescence decays distinguish normal, chronic pancreatitis, and adenocarcinoma tissues 73
4.4.2 Bi-exponential and Laguerre expansions fitting methods characterize differences between normal, chronic pancreatitis, and adenocarcinoma 74
4.4.3 Fluorescence decay analysis classifies normal, chronic pancreatitis, and adenocarcinoma both *ex* and *in vivo* 75
4.4.4 Endoscopically-compatible probe measures fluorescence decay data consistent with proof-of-principle fiber-optic probe 78
4.5 Discussion and conclusions 79

Chapter 5. Instrumentation to rapidly acquire fluorescence wavelength-time matrices of biological tissues 83

5.1 Introduction 83

5.2 Instrumentation and experimental methods 86

5.2.1 Clinically-compatible instrumentation 86

5.2.2 Optical configurations (fiber optics vs. free space) 88

5.2.3 Sample preparation 89

5.3 System characterization - reference fluorophores in fluid solution 90

5.3.1 Signal-to-noise as function of acquisition time 90

5.3.2 Wavelength-resolved fluorescence 92

5.3.3 Time-resolved fluorescence and extraction of fluorescence lifetimes 93

5.4 Tissue-simulating phantom study 97

5.5 Discussion 101

5.6 Conclusions 103

Chapter 6. Non-invasive assessment of implanted tissue-engineered constructs success *in situ* by quantitative diffuse reflectance spectroscopy 105

6.1 Introduction 105

6.2 Materials and methods 106

6.2.1 Construct culture protocol - Ex Vivo Produced Oral Mucosal Equivalents (EVPOME) 106

6.2.2 Study design – implantation cohort development and characterization ... 107

6.2.3 Construct implantation protocol – murine model 112

6.2.4 Tissue diffuse reflectance spectroscopy instrumentation 112

6.2.5 Diffuse reflectance spectroscopy measurement protocol 115
6.2.6 Optical data set and pre-processing 115
6.2.7 Quantitative reflectance spectral analysis 116
6.2.8 Histology scoring by expert panel 118
6.2.9 Statistical analysis 119
6.3 Results 119
6.3.1 Glucose readings are non-invasive, but inherent measurement variability limits ability to distinguish control from stressed constructs 119
6.3.2 Histology sections are able to distinguish control from stressed constructs, but are destructive 120
6.3.3 Reflectance spectra distinguish constructs sorted by experimental condition and post-implantation histology score 121
6.3.4 Reflectance parameters distinguish constructs sorted by experimental condition and histology score 123
6.4 Discussion 124
6.5 Conclusion 126
Chapter 7. Clinical translation and commercialization of optical spectroscopy technology……. 127
7.1 Clinical applications 127
7.2 Clinical design considerations 128
7.2.1 Regulatory issues 128
7.2.2 Integration with hospital environment 130
7.2.3 Clinical trials 131

7.3 Commercialized clinical fluorescence technologies 133

7.4 Conclusions 135

Chapter 8. Conclusions and future directions 137

8.1 Major contributions of this dissertation 137

8.2 Future work 145

References 150

List of Figures

Figure 1.1. Jablonski diagram sketch demonstrating the simplified three-step fluorescence process. (A) An excitation photon is absorbed by a fluorophore, raising the energy of an electron to an excited state. (B) The electron undergoes internal energy conversion to the base level of the excited state. (C) The excited electron decays to the ground state, emitting a fluorescence photon with energy equal to the energy difference between the states. 5
Figure 1.2. Normalized spectral tissue fluorescence measured from three common tissue fluorophores, including extracellular matrix collagen and intracellular biomolecules NAD(P)H and FAD. 7
Figure 1.3. Fluorescence spectroscopy is characterized by excitation photons (blue arrow) entering a tissue at wavelength λ_{ex}, propagating according to the tissue optical properties (absorption coefficient μ_{ai}, scattering coefficient μ_{si}; i=layer, all μ=f(λ)) at the excitation wavelength, being absorbed and isotropically re-emitted as fluorescence by a fluorophore (F_1, F_2; green and red stars), and fluorescence photons propagating back to the tissue surface according to the tissue optical properties at the emission wavelength. Tissue optical properties are frequently different in each layer of a multi-layered tissue, impacting the photon trajectories in each layer. Upon exiting from the tissue surface, the photons (green and red arrows) can be collected by fiber-optic probes and sent to a detector. The detected fluorescence intensity spectrum contains information about the fluorophores in each tissue layer. Measured data can be analyzed to characterize the sample and extract tissue information, including fluorophore concentrations and tissue optical properties..... 12
Figure 1.4. Wavelength- and time-resolved fluorescence data from a standard calibration fluorophore (Rhodamine 6G) is shown. (A) A three-dimensional matrix is composed of fluorescence time-resolved decays at user-selected wavelengths and a resulting wavelength-resolved spectrum. Time-resolved decays can be extracted and analyzed at each user-input wavelength, including the peak fluorescence intensity wavelength. In a complex sample with multiple fluorophores, decays can be extracted and analyzed at several wavelengths, yielding different decay dynamics vs. wavelength that reveal the relative proportion of each fluorophore in the sample. (B) The fluorescence decay at the wavelength of peak fluorescence intensity was extracted and analyzed via a least-squares iterative fit to a single exponential decay. Minimal residual shows a high quality fit [24]. (Used with permission)..... 19
Figure 1.5. Fiber-optic probes for tissue spectroscopy have been developed using a variety of geometries, as illustrated here [64]. (A) Probe that uses a single fiber for both excitation and detection. The excitation light propagates into the turbid media and creates a glow ball of excitation light; detected fluorescence photons also originate within the glow ball. (B) Probe with a single source fiber and multiple detector fibers positioned at various distances from the excitation fiber. This probe can detect photons that traveled

deeper into the tissue than in (A), with larger depth penetration for increased center-to-center spacing. Average classical photon path are shown between each fiber by the parabolic volumes. (C) A ring fiber bundle is employed to detect the same fluorescence information as in (B), but more fluorescence is detected with multiple source or detection fibers. Additionally, several center-to-center fiber spacing can be employed to detect different sample depths. Each concentric ring of fibers (gray and black) represents collection fibers with a fixed center-to-center spacing relative to the central white fiber. Employing concentric rings of fibers for excitation or emission detection can increase the measured fluorescence intensities. Fiber rings can be employed for either excitation or detection, with modifications interrogating different photon paths. (D) A vertical offset is introduced between the fiber probes and the sample surface to predominately excite and detect from a more superficial depth than in either (A) or (B). (E) Probe in which the fibers are angled relative to the sample. Angled excitation and detection promotes the detection of photons to propagate to shallower paths and thus detected fluorescence originates from shallower tissue depths. (F) A ball lens is employed to excite fluorescence in the upper layer of a sample. The detected fluorescence has been shown to be from a more superficial layer than that in (A) and (B) [78]. (G, H) Beveled fibers are employed that function similar to the angled fiber in (E) without needing to change probe orientation relative to tissue surface. (H) Beveled fibers can be designed to detect fluorescence from different sample layers or depths [79]. 24

Figure 2.1. Conceptual illustration (to scale) of the distribution of 400 nm photons (left) and 700 nm photons (right) launched into a pancreatic adenocarcinoma tissue site with the fiber-optic probe configuration used in clinical studies (three adjacent identical fibers with diameter 600 μm, arranged in a triangular configuration). The probe appears tilted to show the bottom face of the fibers, but the optical axis of the probe was placed perpendicular to the tissue surface for all measurements reported in this study. The distribution of photons within the tissue (orange and yellow glowball) is related to scattering from morphological tissue features (shown here as purple-stained cell nuclei and pink-stained extracellular collagen fibers). The structural tissue components (such as cell nuclei and extracellular collagen fibers) responsible for wavelength-dependent scattering of incident light are not expected to change during short periods of data acquisition, even when hemoglobin concentration and blood oxygenation (and hence, wavelength-dependent absorption) are changing. Therefore, quantitative optical spectroscopy (with PTI modeling) should enable accurate and consistent scattering property extraction even when tissue absorption is changing due to variations in blood content. The histology images are from [102]. 34

Figure 2.2. Conceptual illustration of the photon-tissue interaction (PTI) model employed to extract pancreatic tissue properties from measured reflectance spectra. The inset of the best fit PTI model is from [23]..... 41

Figure 2.3. PTI model accurately scales reflectance measurements from tissue-simulating phantoms with 5 μM hemoglobin to those from phantoms with 20 μM hemoglobin. Measurements were obtained using fiber-optic probes with (a) 600 μm diameter fibers with center-to-center spacing of 660 μm and (b) 200 μm diameter fibers with center-to-center spacing of 220 μm. Both phantoms also included scattering from polystyrene microspheres with 9 μm diameter. PTI model fits extracted tissue optical parameters, including scatterer diameter and concentration, concentration of absorbers, and

anisotropy. PTI model best-fits (shown) extracted scatterer diameter to within 1% and absorber concentration to within 17%. 45
Figure 2.4. Demonstration of PTI model scaling measured canonical normal with 600/660 probe to measured reflectance obtained with 200/220 probe from a phantom with different absorption than the canonical normal. In this demonstration, the canonical normal was measured from a liquid phantom composed of 9 μm diameter polystyrene microspheres and 5 μM blood in deionized water with the 600/660 probe. The measured reflectance was measured from a liquid phantom of 9 μm microspheres, but with 20 μM blood and measured with the 200/220 probe. Scatterer diameter was extracted to < 1% error and absorber concentration was extracted to < 6% error. 46
Figure 2.5. Effect of changes in two different scattering parameters on PTI reflectance model $R_{PTI}(\lambda)$ of human pancreatic tissue: (a) varying values of the morphological parameter attributed to collagen ρ_c and (b) varying values of the mean morphological parameter <L>. Changing the morphological parameter attributed to collagen has a subtle effect on the reflectance lineshape from 450-525 nm, while changing the mean morphological parameter size has a much more notable effect on the reflectance in this region. 47
Figure 2.6. Demonstration of PTI reflectance models $R_{PTI}(\lambda)$ for various combinations of tissue scattering parameters (a), shown alongside average measured data from human pancreatic tissues [31] (b). When the morphological parameter attributed to collagen fibrils is increased to three times that of normal pancreatic tissue but the mean morphological parameter is left unchanged (dot-dashed green line in (a)), there is a notable similarity between the PTI model and the measured data from chronic pancreatitis (dot-dashed green line in (b)), relative to normal (blue lines in (a) and (b)). When the mean morphological parameter is increased to 1.25 times that of normal tissue, and the morphological parameter attributed to collagen fibrils is kept at three times that of normal tissue, the PTI model (dashed red line in (a)) looks similar to the average measured reflectance from adenocarcinoma (dashed red line in (b)), relative to normal. The increase in morphological parameter attributed to collagen fibrils provides a subtle change in the reflectance from 450-525 nm, while the increase in nuclear morphological parameter size is responsible for the more pronounced change in the reflectance in this region. The error bars in (b) represent the standard error. 48
Figure 2.7. Pairs of reflectance measurements (solid blue and green curves) acquired from two different pancreatic adenocarcinoma sites ((a) and (b)), shown with the corresponding fits of the PTI model to the measured spectra from 430-500 nm (dashed red and orange curves). For the site shown in (a), the two measured spectra were very similar, and the values of the total hemoglobin concentration [Hb]tot, the morphological parameter L/Lo, and the mean reduced scattering coefficient $<\mu_s'>$ extracted from the two spectra were identical ([Hb]tot = 1 μM, L/Lo = 1.3, $<\mu_s'>$ = 18.7 cm^{-1}). For the site shown in (b), the two measured spectra were significantly different (likely due to changes in absorption caused by the draining of blood from the freshly excised tissue), and the [Hb]tot values extracted from the two spectra differed by 15 μM ([Hb]tot1 = 16 μM, [Hb]tot2 = 1 μM), but the values of the morphological parameter L/Lo and mean reduced scattering coefficient $<\mu_s'>$ extracted from the two spectra were still identical (L/Lo = 1.3, $<\mu_s'>$ = 18.7 cm^{-1}). This result illustrates the ability of the PTI model to extract

consistent values of tissue scattering parameters even when the blood content of the tissue changes over time. 51
Figure 2.8. Histograms of differences in extracted values of the total hemoglobin concentration (Δ[Hb]tot) and morphological parameter (ΔL/Lo) for (a, b) the 16 pancreatic tissue sites with similar repeated reflectance measurements and for (c, d) the 26 pancreatic tissue sites with significantly different repeated reflectance measurements. (For ease of view, the bar at the far left of (c) represents two sites with Δ[Hb]tot values of -135 μM and -280 μM, respectively.) When the two reflectance measurements were not significantly different, the magnitude of Δ[Hb]tot (a) was less than 10 μM for 15 of 16 sites (94%), and the average difference between the two extracted L/Lo values (b) was less than 1%. When the two reflectance measurements were significantly different, the magnitude of Δ[Hb]tot (c) was 10 μM or greater for 21 of 26 sites (81%), but the average difference between the two extracted L/Lo values (d) was still less than 7%. 54
Figure 3.1. Pancreatic tissue optical measurement protocol, designed to mimic fine-needle aspiration (FNA) procedures by introducing the optical probe via a hollow angiocatheter. (1) In vivo: at this stage of surgery, tissue was still perfused with some blood and was near body temperature. The sterilized fiber-optic probe (6 m length) extended from the RFLS in the non-sterile field to the patient in the sterile field. At each selected site, the surgeon inserted a 14 gauge angiocatheter (B Braun Medical) ~1 cm into the tissue, removed the stylet from the angiocatheter, and inserted the fiber-optic probe. Data acquisition for each site was < 45 s, with each modality acquired in < 1 s. (2) In vivo and ex vivo measurements were acquired at the same tissue site by marking the site prior to resection. (2, right) Each optical measurement was estimated to interrogate ~1 mm3 of tissue. Repeatability was tested by collecting two successive optical measurements at each site, with up to two tissue sites measured per patient. Tissue sites were biopsied for histopathologic analysis. 58
Figure 3.2. Optical measurements from a tissue site in vivo and ex vivo for (A) steady-state reflectance and (B) steady-state fluorescence. Measurements of the same tissue site contained similar features, attributed to similar tissue composition and morphology [23], and differed only slightly between 400-475 nm due to the anticipated blood content variations. The site was histopathologically confirmed to be adenocarcinoma..... 62
Figure 3.3. Representative *in vivo* reflectance measurements from human pancreatic adenocarcinoma (blue solid: A, B), (A) normal human tissue (green dashed), and (B) human pancreatic cancer tumor xenograft in a non-obese diabetic/severe combined immunodeficiency (NOD/SCID) mouse (red dashed) [31]. In the diagnostically important wavelength range between 455-525 nm (shaded), adenocarcinoma tissues have greater relative reflectance than normal tissues, consistent with extensive *ex vivo* studies [5,23,31,101,130]. 63
Figure 3.4. Quantitative analysis of *in vivo* reflectance data is consistent with *ex vivo* results and can distinguish between normal human pancreas and pancreatic adenocarcinoma. (A) The $R_{470\ nm}/R_{650\ nm}$ ratio for *in vivo* data (gray box plot) analyzed the pronounced spectral feature at 470 nm which clearly distinguished adenocarcinoma from normal tissues. The blue and green overlays show the analysis for an extensive *ex vivo* data set [23], which shows the same trend as that observed *in vivo*. Minor differences between *ex vivo* and *in vivo* results were attributed to the limited experimental control of local blood content during *in vivo* measurements. (B) PTI model best fit (red, dotted) to

the *in vivo* adenocarcinoma data in **Figure 3.2** (blue) (4% fit error between 450 – 530 nm). (C) A PTI-extracted morphological parameter (L/L_0, related to changes in cellular nuclear size and shape) from *in vivo* measurements clearly distinguished adenocarcinoma from normal pancreas, consistent with results from an extensive *ex vivo* data set [23]. *In vivo* measurements from adenocarcinoma tissues modeled with an *ex vivo* "canonical normal" (from [23]) showed comparable results to employing an *in vivo* "canonical normal. Error bars represent standard error. 64
Figure 4.1. (A) A Fluorescnece Lifetime Spectrometer collected fluorescence decays from pancreatic tissues with a free-space fiber-optic probe. (B) *Ex vivo* data set and *in vivo* pilot study measurements were measured with a large fiber-optic probe for proof-of-principle studies. To demonstrate compatibility with future endoscopic procedures, optical fiber diameter was reduced by $1/3^{rd}$. The endoscopically-compatible fiber-optic probe was emlpoyed during a *ex vivo* feasibility study of 1 normal patient site. The third channel was not employed in this study, but was used in previous studies for reflectance spectroscopy measurements. Abbreviations - ND: neutral density filter, L: collimating lenses, LP: long-pass filter at 500 nm, APD: avalanche photodiode. 68
Figure 4.2. Time-resolved fluorescence decays distinguish normal, chronic pancreatitis, and adenocarcinoma tissues from (top row) *ex vivo* and normal from adenocarcinoma tissues from (bottom row) *in vivo* measurements. Fluorescence decays are shown with (left column) linear and (right column) logarithmic y-axis for improved comparison of data. Fluorescence decays were normalized to their peak, the peak from all decays of each tissue type aligned, and the aligned decays averaged for comparison. Fluorescence decays measured from adenocarcinoma and chronic pancreatitis tissues are broader than corresponding measurements of normal tissues. Error bars represent standard error. 73
Figure 4.3. Fluorescence decay fitting parameters (top row) A1 and (bottom row) LEC1 distinguish measurements from normal, chronic pancreatitis, and adenocarcinoma tissues (left column) *ex vivo*. Extracted quantitative fitting parameters from (right column) *in vivo* decays were consistent for normal and adenocarcinoma tissues. Relative differences in fitting parameters of normal, chronic pancreatitis, and adenocarcinoma tissues indicate decay broadening from normal to chronic pancreatitis to adenocarcinoma tissues (**Figure 4.2**). Statistical analysis was not performed on *in vivo* data due to limited measured sites. For *in vivo* data, the line from normal sites represents the mean extracted parameter from two sites. 74
Figure 4.4. Receiver operator characteristic curves were computed for the 5 tissue groupings: (1, top left) A v (CP & N), (2, top middle) A v N, (3, top right) (A & CP) v N, (4, bottom left) A v CP, and (5, bottom middle) CP v N. (top row) To distinguish adenocarcinoma from either benign or normal tissues, receiver operating characteristic curves had highest area under the curve (AUC) when varying diagnostic threshold to the sum of P(A) and P(CP). (bottom row) To distinguish chronic pancreatitis from either adenocarcinoma or normal tissues, receiver operating characteristic curves had highest AUC when varying diagnostic threshold to P(A). Overall, A1 was the most useful diagnostic parameter to distinguish adenocarcinoma from benign tissues, whereas LEC1 helped improve classification of chronic pancreatitis tissues. 76
Figure 4.5. Two fluorescence decay fitting parameters, A1 and LEC1, classified adenocarcinoma, chronic pancreatitis, and normal tissues. A1, the percent contribution of the long lifetime component extracted with a bi-exponential decay model, best

distinguished adenocarcinoma from benign tissues, whereas LEC1, the percent contribution of the first Laguerre expansion function, best distinguished adenocarcinoma from chronic pancreatitis tissues. Red lines show manual classification threshold to distinguish adenocarcinoma from benign tissues (for A v (N&CP), A v CP, and A v N). Green lines show manual classification threshold to distinguish chronic pancreatitis and diseased from normal tissues (for CP v N and (A&CP) v N). 77
Figure 4.6. *In vivo* fluorescence decays accurately distinguish normal from adenocarcinoma tissues. An extensive *ex vivo* data set was employed to train the classification algorithm to distinguish the *in vivo* measurements. With measured sites from the pilot feasibility study (2 normal and 5 adenocarcinoma), time-resolved fluorescence distinguish both normal sites and 4/5 adenocarcinoma sites with A1 and 3/5 adenocarcinoma sites with LEC1..... 78
Figure 4.7. As part of a feasibility study, one *ex vivo* human pancreatic tissue normal site was measured with a proof-of-principle and an endoscopically-compatible fiber-optic probe. Results show good agreement between the two measurements, indicating that no fluorescence information is lost with an endoscopically-compatible fiber-optic probe. .. 79
Figure 5.1. Fluorescence wavelength-time matrix (WTM) of 1 μM Rhodamine 6G in ethanol acquired with fiber-optic probes for light delivery and detection. The WTM contains both wavelength-resolved and time-resolved fluorescence data. 85
Figure 5.2. Schematic of the instrumentation developed for rapid acquisition of fluorescence WTMs, using fiber-optic probes for light delivery and detection (set-up 4, **Table 5.1**). WTMs were also obtained with three other set-ups (**Table 5.1**): (1) right-angle free-space geometry, in place of the fiber-probes, for light delivery and detection; (2) free-space light delivery and a fiber-probe for fluorescence detection; (3) a fiber-probe for light delivery and right-angle free-space geometry for detection. 86
Figure 5.3. Signal-to-noise characterization of the system, performed on a stock solution of fluorescent beads: (a) standard deviation of measured fluorescence intensity (green curve), compared to prediction of Poisson theory (blue curve), as a function of acquisition time; (b) normalized fluorescence decay curves for 5 laser pulses averaged (red curve, corresponding to red circle in (a)) and 1250 laser pulses averaged (purple curve, corresponding to purple circle in (a)). The arrow in (a) denotes data acquisition with 125 laser pulses averaged; the standard deviation of the relative peak intensity at this point is ~0.25 (a.u.) with a peak signal intensity of ~28 (a.u.), yielding a SNR greater than 100..... 92
Figure 5.4. Fluorescence spectra of rhodamine 6G (blue curve), rose bengal (red curve), and fluorescein (green curve), measured with the fiber-based system set-up 4 and normalized to the area under the curve. Each curve is the average of three measurements; the error bars represent the standard deviation. 93
Figure 5.5. Time-resolved fluorescence decay curves measured on solutions of rhodamine 6G ((a), (d)), rose bengal ((b), (e)), and fluorescein ((c), (f)). Panel (a) plots 36 averaged rhodamine 6G fluorescence decays, panel (b) plots 36 averaged rose bengal fluorescence decays, and panel (c) plots 24 averaged fluorescein fluorescence decays (four system set-ups per fluorophore, three emission wavelengths for rhodamine 6G and rose bengal, two emission wavelengths for fluorescein). The error bars represent standard deviation. In panels (d), (e), and (f), one representative decay curve for each fluorophore measured with set-up 4 was fit to a single exponential decay. 95

Figure 5.6. Wavelength-resolved (a) and time-resolved (b) fluorescence from tissue-simulating phantoms with varying scattering coefficients (measured with a source detector separation of 0.66 mm). Three sites on each phantom were measured. The spectra represent the average of the three sites, with error bars representing standard deviation. Panel (a) also includes spectra from pure gelatin and from a solution of rhodamine B in deionized water. 99
Figure 5.7. Measured time-resolved fluorescence decay curves from two phantoms with biologically-relevant scattering coefficients at a source-detector separation of 4.66 mm (a), compared with the predictions of diffusion theory (b). Each curve in (b) is a convolution of the diffusion theory result with the instrument response function of the corresponding tissue-simulating phantom. For the sake of comparison, the experimental results and the diffusion theory predictions were time-shifted to align the rising shoulders of the curves. In both panels, the time-resolved decay from the medium with the higher scattering coefficient (red dashed curve) was noticeably broader than the decay from the medium with the lower scattering coefficient (blue solid curve). 100
Figure 6.1. Study design. 108
Figure 6.2. Representative hematoxylin and eosin (H&E) sections are shown from (A-C) control/healthy and (D-F) stressed/compromised constructs (A,D) pre- and (B-C,E-F) post-implantation sorted by experimental condition (control versus stressed) and histology score (healthy versus compromised). (A) Pre-implantation control histology section shows the three-layered EVPOME structure, with a top keratin layer (K), a middle living cell layer (LC), and a bottom dermal equivalent layer (DE). Mature healthy (majority of control) constructs developed keratin and living cell layers atop the dermal equivalent, whereas compromised (majority of stressed) constructs did not. Compared to (A) pre-implantation control/healthy constructs, (B,C) post-implantation control/healthy constructs showed (B,C) continued development of the keratin and living cell layers after 1 week and (C) visible revascularization after 3 weeks[16] post-implantation. Alternatively, stressed/compromised constructs had undefined keratin and living cell layers (D) pre-, (E) 1 week, and (F) 3 weeks post-implantation. 110
Figure 6.3. Pre-implantation construct success was characterized by histology and percent glucose consumption. (left column) Sorted by pre-implantation histology score, 100% of control constructs and only 25% of stressed constructs had a pre-implantation histology score > 2. (right column) Sorted by percent glucose consumption, only 61% of control constructs and 5% of stressed constructs had a percent glucose consumption > 5%. When sorted by cohort, pre-implantation histology score distinguished control from stressed constructs *(*p = 0.03 for constructs to be implanted for 1 week, p = 0.01 for constructs to be implanted for 3 weeks)*,* whereas percent glucose consumption did not (p = 0.12 for constructs to be implanted for 1 week, p = 0.09 for constructs to be implanted for 3 weeks)..... 111
Figure 6.4. Diffuse reflectance spectroscopy instrumentation selectively interrogated mature EVPOME constructs. A standoff fiber-optic probe enabled rapid, portable, and repeatable measurements. Broadband light was delivered to and collected from the construct with a beveled fiber-optic probe, shown in cross-sectional and side view. A ray traced model, employed in ZEMAX® with tissue optical properties[18] of dermal equivalent, estimated the optical interrogation volume[18] in mature constructs. Cross-sectional view shows the (red) 7 excitation beveled fibers around a (blue) common

detection fiber. Side view shows simulated (green and red) excitation photons overlap with (blue) emission photons within the constructs keratin, living cell, and dermal equivalent layers without interrogating the native tissue. One excitation fiber ray is colored green to illustrate the interactions of rays from different excitation fibers more clearly..... 114
Figure 6.5. Representative DRS measurements at 2.0 mm standoff from (left) 1 week and (middle) 3 weeks post-implantation constructs compared to (right) dermal equivalent that was pre-soaked in phosphate buffered saline. (gray overlays) The primary wavelengths employed for spectral intensity classification correspond to (right) hemoglobin absorption bands[19], cellular and collagen scattering (slope from 650-760 nm), and the peaks and valleys of (left) principal component 6 (PC6). As expected, (right) hemoglobin absorption was lowest from (left) 1 week post-implantation stressed and greatest from (middle) 3 weeks post-implantation control constructs. 118
Figure 6.6. Pre-implantation histology scores from control and stressed constructs predicted post-implantation histology scores 1 week post-implantation, but not 3 weeks post-implantation. (left) Post-implantation histology scores from 1 week post-implantation constructs distinguished control from stressed constructs (p = 0.02). (right) At 3 weeks post-implantation, majority of constructs had average post-implantation histology score between 2 and 3. While histology score distinguished control and stressed constructs (p-value = 0.03), the decrease in histology score for control constructs indicated advanced stages of wound healing, where low histology scores indicated the invasion of host cells. Gray dotted lines indicate employed thresholds to characterize healthy and compromised constructs based on panel histology score (for **Figure 6.7**). 121
Figure 6.7. Diffuse reflectance measurements were normalized to peak, averaged, and renormalized to peak. These average diffuse reflectance measurements from (left column) 1 week and (right column) 3 weeks post- implantation constructs clearly distinguish measurements from constructs sorted by (left column) experimental condition and (right column) post-implantation histology score. The absorption bands near ~422 nm and ~540-570 nm were attributed to hemoglobin absorption [173], whereas the higher intensity regions near between 650-760 nm were attributed to sample scattering properties [168]. As expected, average reflectance spectra differed most when classifying constructs according to post-implantation histology, which accounted for stressed constructs that grew well *in vivo*. Gray overlays emphasize primary wavelength ranges of interest from **Figure 6.4**. Error bars represent standard error..... 122
Figure 6.8. *In vivo*, non-invasive, and label-free reflectance spectra, characterized by 3 reflectance parameters, distinguish 1 week post-implantation constructs at the batch level after sorting by experimental condition (control versus stressed) and histology score (healthy versus compromised). Statistically significant parameters indicate that DRS characterizes tissue-engineered construct success *in vivo*. Error bars represent standard error..... 123
Figure 7.1. Schematic of the 'translational pipeline' from device discovery through FDA approval. An emphasis is placed on the iterative process during device development and clinical trials [196]. The goal of a common translational pipeline is to improve and standardize the approval process for medical imaging technologies. With faster approval times, and thereby expedited returns on investment, investors should be more apt to fund

clinical imaging technology companies developing fluorescence instrumentation. (Adapted with permission from [196]). 130

List of Tables

Table 1.1 Approximate ranges for optical properties of biological tissue [14,35,36]..... 13
Table 2.1. Tissue parameters that can be characterized by photon-tissue interaction (PTI) model of reflectance..... 39
Table 4.1. Analyzable *ex* and *in vivo* data set. 69
Table 5.1. Set-ups employed to acquire fluorescence WTMs..... 88
Table 5.2. Lifetime values obtained from standard fluorophore solutions. 97
Table 6.1. Number of batches, constructs, sites, and measurements in data set after employing exclusion criteria. Batches indicate control and stressed constructs cultured from one distinct primary human cell donor..... 116

Abstract

It is well known that changes in tissue morphology and/or biochemistry can affect tissue function. Characterizing these changes in tissue function through non-invasive and label-free assessment can inform clinical practice and improve patient outcomes. Optical spectroscopic techniques (including reflectance, fluorescence, and Raman scattering) coupled with advances in fiber-optic probe technologies, have enabled development of "free-space" portable spectroscopy systems that are suitable for studying functional changes in biological tissues *in vivo*. In this dissertation, we employ non-invasive, quantitative, label-free, portable, and clinically-compatible reflectance and fluorescence spectroscopic technology for use in two clinical challenges: (1) improved detection of pancreatic disease and (2) post-implantation monitoring of tissue-engineered construct wound healing in an *in situ* murine model.

(1) Currently, pancreatic cancer is most commonly detected at its latest stages. As a result, only 6% of pancreatic cancer patients survive 5 years after diagnosis, making it the 4th leading cause of cancer death in the United States. To improve detection of pancreatic cancer, we studied the diagnostic utility of optical spectroscopy to detect pancreatic disease in 5 Stages, with Stages 1 and 2 previously reported. Stage 1 showed that *ex vivo* measurements of human adenocarcinoma tissue correspond well to *in vivo* measurements from a tumor xenograft in a murine model. Stage 2 showed that malignant tissues measured *ex vivo* distinguish malignant and benign tissues. In this dissertation, we

discuss Stages 3-5. In Stage 3, a photon-tissue interaction (PTI) model was verified with measurements from tissue-simulating phantoms and validated with measurements from a subset of *ex vivo* human tissues collected in Stage 2. We show that a calibrated PTI model consistently extracts biologically-relevant optical tissue scattering parameters in the presence of variable hemoglobin absorption. In Stage 4, we perform the first ever, to our knowledge, *in vivo* feasibility study employing optical steady-state spectroscopy to detect malignant tissues during open surgery. In Stage 5, we investigate time-resolved fluorescence spectroscopy *ex* and *in vivo* to improve pancreatic disease classification. Furthermore, we show the first ever human pancreatic tissue measurements with an endoscopically-compatible fiber-optic probe.

(2) Regulatory approval for tissue-engineered combinational devices, including tissue constructs developed for human implantation, requires reliable methods to assess post-implantation wound healing *in vivo*, of which none currently exist. In this dissertation, we investigate diffuse reflectance spectroscopy to detect hallmarks of graft wound healing, including tissue revascularization, cell proliferation, and cell density, based on construct absorption and scattering properties.

Chapter 1.
Introduction

1.1 Optical spectroscopy

Optical spectroscopy is a widely employed technique in chemical and biomedical applications for non-invasive specimen interrogation and monitoring that can be performed on both living and stained/sectioned samples [1]. A variety of spectroscopic techniques have been developed for fluorescence applications in quantitative clinical tissue diagnostics [2-4], including several involving cancer diagnostics [5-8]. The methods developed for clinical tissue sensing are translatable to applications in regenerative medicine, since similar excitation sources, optical delivery systems, and photon detectors can be employed for sensing in tissue-engineered constructs with minimal modifications [9]. Furthermore, these techniques can be employed to optically measure human tissues, providing the experimental groundwork to study tissue-engineered constructs both during development and *in vivo*, after human implantation.

When interrogating human tissues, safety is paramount. Optical spectroscopy measurements cause minimal to no damage with controlled laser powers; therefore, measurements can be taken multiple times, at multiple sites, and performed for repeated measurements of human tissues and for assessing tissue-engineered constructs during culturing of a sample, prior to release of a tissue-engineered construct for clinical use, and after implantation. In particular, optical spectroscopy is able to meet the specific needs for the monitoring and analysis of human tissues and tissue-engineered cell-scaffold constructs, including analyzing a complex three-dimensional structure with local

heterogeneities, being adaptable to measuring a variety of constructs – including living samples for label-free optical assessment of tissue-engineered constructs and translatable to *in vivo* measurements post-implantation [10].

In this dissertation, we focus on clinical applications of reflectance and fluorescence spectroscopy for quantitative, optical biopsy to address two clinical challenges: (1) improved detection of pancreatic disease and (2) non-invasive assessment of tissue engineered constructs. Such optical spectroscopies have shown promise in clinical applications for rapid, non-invasive, label-free, quantitative, and safe interrogation of human tissue. Furthermore, these optical technologies are compatible with remote sensing applications requiring miniature probes, including endoscopy and oral surgery.

1.2 Clinical and biological measurement challenges that reflectance spectroscopy is suited to address

Reflectance spectroscopy is suited for rapid and non-invasive sensing in bulk tissues as a diagnostic tool (*e.g.*, distinguishing healthy from compromised tissue), analyzing variations in local tissue absorption (*e.g.*, measuring local concentration of deoxygenated and oxygenated hemoglobin), and interrogating local tissue structure (*e.g.*, assessing cellular structures like nuclei or mitochondria) [11,12]. Advantages to reflectance sensing include the ability for real-time, non-invasive assessment of local changes in tissue absorption and morphology, both potential indicators of compromised tissues.

1.2.1 Technical implementation of reflectance spectroscopy

The interaction of light and human tissues is complex. In the simplest model, light interacts with tissues through wavelength-dependent scattering and absorption events.

Scattering events occur when an index of refraction mismatch reflects light within a tissue, occurring from common, endogenous biological components like extracellular matrix or cell nuclei. Reflectance occurs if the scattered excitation light has preserved energy. That is, the light was elastically scattered without a change in wavelength. These elastic scattering events are wavelength-dependent, meaning that relative intensity of scattered light varies with wavelength, resulting from the wavelength-dependence of the scattering phase function [11]. Therefore, the detected reflectance spectrum contains unique spectral contributions from scatterers encountered during their photon path length in the tissue. Alternative to scattering, absorption events occur when light is specifically converted to heat energy in accordance with Beer's law by absorptive biomolecules, which reduce the light intensity at specific wavelengths proportional to absorber concentrations.

Models employing *a priori* information about tissue composition can resolve scattering properties (*e.g.*, the average morphology and density of a scatterer like cell nuclei) and absorption properties (*e.g.*, the concentration and oxygenation of hemoglobin). Qualitative or quantitative assessment of local oxygenated and deoxygenated hemoglobin concentrations can be used as indirect measures of tissue viability and graft success [12].

Diagnostic utility of optical spectroscopy is contained within the balance of tissue scattering and absorption, simultaneously providing biologically-relevant tissue information comparable to histology. Reflectance spectroscopy can be employed for rapid and non-invasive assessment of local tissue morphology. In biological tissues, light is preferentially forward scattered, encountering numerous scattering events before being emitted from the tissue for detection [11]. As a result, the experimental set-up of

excitation and detection geometries can impact measured spectra, discussed in more detail in the following sections.

1.3 Clinical and biological measurement challenges that fluorescence spectroscopy is suited to address

Biomedical applications of fluorescence spectroscopy include bulk tissue diagnostics (*e.g.*, distinguishing healthy from non-viable tissue), determining the relative quality of a sample (*e.g.*, measuring cellular growth rate), and assessing local biochemical changes (*e.g.*, characterizing the binding state of nicotinamide adenine dinucleotide (NADH)) [1]. Advantages of fluorescence sensing include the ability to assess and monitor human tissues and tissue-engineered constructs in a non-invasive, non-destructive, and locally selective manner.

1.3.1 Technical implementation of fluorescence spectroscopy

Several physical processes can occur when light is absorbed by a sample [1]. **Figure 1.1** shows a Jablonski diagram detailing the stages of one such process, fluorescence, which occurs when an excitation photon is absorbed by a sample fluorophore.

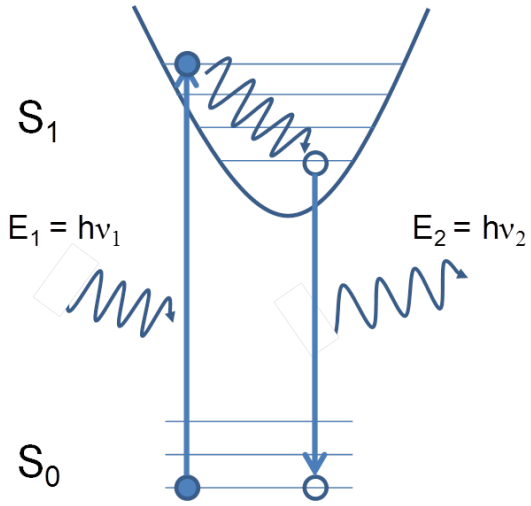

Figure 1.1. Jablonski diagram sketch demonstrating the simplified three-step fluorescence process. (A) An excitation photon is absorbed by a fluorophore, raising the energy of an electron to an excited state. (B) The electron undergoes internal energy conversion to the base level of the excited state. (C) The excited electron decays to the ground state, emitting a fluorescence photon with energy equal to the energy difference between the states.

The fluorescence photon is emitted isotropically (emitted in a random direction) with energy equal to the difference between the ground and excited energy levels of the electron. Fluorescent molecules contain different characteristic energy levels and electrons that can absorb excitation energy; therefore, each fluorescent molecule has unique and characteristic optical absorption and fluorescence emission spectra.

Fluorophores in biological systems can be divided conveniently into two groups: endogenous and exogenous. Endogenous fluorophores are naturally-occurring biological molecules that are native to cells and tissues, including the biological materials employed to develop tissue-engineered constructs and intracellular metabolites. Typically, endogenous fluorophores are low-light level emitters [13,14] compared to exogenous fluorophores, molecules that are not naturally-occurring in a sample and are added to provide contrast for fluorescence measurements. Exogenous fluorophores are widely used

to image cells and thin tissue sections, but introducing exogenous molecules into human tissues or thick, tissue-engineered constructs involves a more invasive process, which could alter metabolic viability and measurement sterility, compromising optical measurements. Therefore, when analyzing tissue-engineered constructs *via* fluorescence spectroscopy, it is common to measure only endogenous fluorescence. Careful application of exogenous fluorophores is required to provide useful fluorescence contrast and characterization in thick tissues.

Endogenous fluorophores typically report on two common components of a tissue-engineered construct: the extracellular matrix and cellular metabolism [13,15]. Typical fluorescence spectra are shown from three common endogenous fluorophores in **Figure 1.2**. Endogenous fluorophores that report on the extracellular matrix can be monitored to study the growth and development of a tissue-engineered construct. These molecules include collagen, elastin, and keratin. Endogenous fluorophores that report on cellular metabolism include nicotinamide adenine dinucleotide (NADH) and flavin adenine dinucleotide (FAD), cellular biochemicals that play a role in redox metabolism and are naturally fluorescent in their reduced (NADH) and oxidized (FAD) states. NADH is produced during cellular glycolysis, an alternative pathway to oxidative phosphorylation for adenosine triphosphate (ATP) generation that occurs in cellular mitochondria, and transported into mitochondria [16]. Then, the high energy electron carried by NADH is utilized during oxidative phosphorylation and the electron transport chain to create a proton gradient, converting NADH to NAD^+ and $FADH_2$ to FAD, while generating cellular energy, ATP. In addition, acetyl Coenzyme A (acetyl CoA) produced during glycolysis and transported into the mitochondria enters the citric acid cycle and converts

NAD^+ to NADH, converts FAD into $FADH_2$, and produces ATP. Having fluorescent molecules at local concentrations dependent upon cellular metabolic processes allows for monitoring of energy metabolism within tissues and tissue constructs.

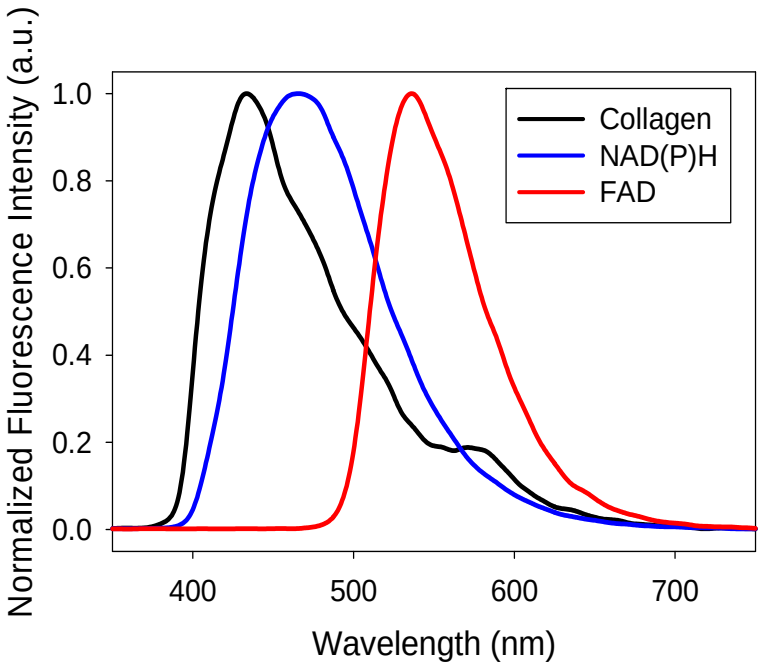

Figure 1.2. Normalized spectral tissue fluorescence measured from three common tissue fluorophores, including extracellular matrix collagen and intracellular biomolecules NAD(P)H and FAD.

The emission spectrum of each fluorophore is characteristic, with a distinct spectral line shape, but many fluorophores emit in the wavelength range from ~325 to 600 nm. Often, several fluorophores are excited with the same excitation light source and each contributes to the measured fluorescence spectra.

Exogenous fluorophores, or fluorescent probes, are fluorescent molecules that can be employed to report on spatial localization and environmental conditions of a sample [17]. Exogenous fluorescent drugs have been developed for use in photodynamic therapy [18],

monitoring pH [19], and cancer diagnostics [20], where the introduced fluorophore accumulates in the tumor region. A combined approach can also be employed with both endogenous and exogenous fluorophores for enhanced contrast [21].

Introducing exogenous fluorophores into tissues can help to characterize the molecules present and their micro-environment, but often compromises the sterility and integrity of the sample, thereby introducing safety and toxicity concerns [22]. Therefore, works discussed in this dissertation include no exogenous dyes.

1.4 Experimental design for reflectance and fluorescence spectroscopy

The design of the experimental set-up determines the sample volume that will be studied, the fluorophores that will be excited, and how the emitted photons will be detected. Therefore, careful consideration needs to be given to the experimental set-up employed, the excitation source chosen, the detector employed, as well as the sample optical properties to measure the most useful data.

1.4.1 Excitation source

All optical measurements require an excitation source, most commonly a laser, light-emitting diode, or lamp. Excitation sources have a variety of characteristic properties that determine the optical data measured. First, sources can be continuous, for collection of spectrally-resolved reflectance or fluorescence data, or pulsed, for collection of wavelength- and time-resolved data. Pulsed sources can be on the order of nanoseconds for single photon excitation or on the order of femtoseconds for multiphoton excitation or time-correlated single photon counting (TCSPC). Second, each source has a characteristic wavelength corresponding to its peak power output. Lastly, pulsed sources have a pulse

repetition rate (*i.e.* number of pulses per second) and corresponding duty cycle (*i.e.* the pulse duration relative to the time between successive pulses).

To collect reflectance spectra, excitation wavelengths must be selected to preferentially interrogate the diagnostically-relevant tissue scatterers and absorbers. For maximizing diagnostic utility, reflectance spectra are often collected over a broad wavelength range (spanning hundreds of nanometers) that have characteristic contributions from specific tissue scatterers and absorbers related to tissue disease state. For the diagnostic applications discussed in this dissertation, reflectance spectra were collected at visible wavelengths between 400-760 nm to interrogate tissue scattering from cell nuclei and extracellular matrix and absorption from hemoglobin and tissue pigments [23].

To collect fluorescence spectra, excitation wavelength must be selected to preferentially excite the fluorophores of interest in a construct [13], with consideration given to sources of background signal or artifacts that may be present. For the diagnostic applications discussed in this dissertation, common excitation source wavelengths used are in the UV-visible range to interrogate concentrations and local biochemistry of collagen, elastin, FAD, and NADH.

To collect time-resolved fluorescence decays, in addition to excitation wavelength, the laser pulse repetition rate and duty cycle need to be considered. A common practice in fluorescence measurements is to average a set number of measurements to increase the output signal-to-noise ratio. Therefore, to acquire data in a rapid fashion, higher pulse repetition rate sources allow for more measurements to be taken in a shorter time, permitting averaging of more fluorescence data collections and thus higher signal-to-noise ratios [24]. However, the detector must be optimized to work with such an

excitation source. The duty cycle must also be considered, including excitation pulse intensity and duration, so that the excitation source generates sufficient fluorescence without harming or damaging the sample [25].

1.4.2 Emission detector

Emitted optical light can be collected with wavelength resolution or time resolution (or both). Each modality provides information about the concentration and microenvironment of a sample and each employs different detection schemes.

For wavelength-resolved data, common detector configurations are spectrographs coupled to a charge-coupled device (including intensifiers (ICCD) or electron multiplying charge-coupled device (EMCCD) [26]) for detection. For time-resolved data, common detectors include photo-multiplier tubes [24], avalanche photo-diodes [27], and streak cameras [28]. Two common collection techniques are time-correlated single photon counting (TCSPC) [29] and direct fluorescence decay recording via a digitizing oscilloscope [2,6,30].

Additionally, to collect both wavelength- and time-resolved fluorescence simultaneously, two common methods exist that employ either one or a combination of the previously mentioned detectors. First, the fluorescence emission light can be beam-split and directed at two separate detectors, one each for wavelength and time detection [31]. Second, an emission monochromator can selectively step through the desired wavelength regime with a measured time-resolved decay at each selected wavelength [24].

1.4.3 Optical sample properties

All tissue-engineered constructs and tissues have optical properties that will affect the optical signal measured from the sample. In particular, we will discuss five optical

properties: the scattering coefficient (μ_s), absorption coefficient (μ_a), fluorophore absorption coefficient (μ_{afx}), anisotropy (g), and absorption quantum yield (Φ) [32,33]. These properties all influence any photon propagation within the sample.

Figure 1.3 shows two photon paths with different center-to-center source to detector spacing. Increasing source to detector spacing preferentially detects scattered photons with longer average photon paths (photons that have traveled deeper within a tissue) than would smaller spacing, evidenced by an optical contribution from Layer 2. The scattering coefficient is the reciprocal of the average path length a photon travels between scattering events. The absorption coefficient is the reciprocal of the average path length a photon travels before being absorbed by a non-fluorophore. The fluorophore absorption coefficient is the reciprocal of the average path length an excitation photon travels before being absorbed by a fluorophore. Multiple fluorophore absorption coefficients are needed for a sample with multiple fluorophores, and multiple scattering coefficients (modeled as a linear combination of each) are needed for a sample with multiple fluorophores.

The tissue anisotropy is the mean cosine of the scattering angle of a photon within a sample. Anisotropy is determined by the phase function used to model a tissue, and anisotropy values range from 0 to 1, with higher values representing more forward scattering media [34]. The quantum yield of a fluorophore defines the efficiency with which a fluorophore absorbing an excitation photon undergoes the fluorescence process. Each fluorophore has a different quantum yield, which also depends on the excitation wavelength employed. In addition, each fluorophore has a fluorescence lifetime, τ, which relates to the radiative decay of a fluorophore.

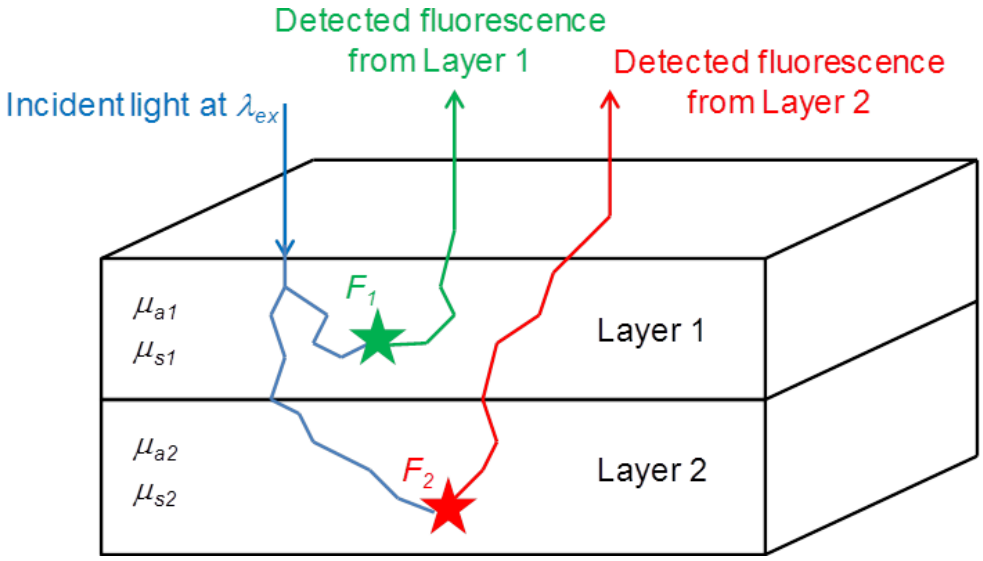

Figure 1.3. Fluorescence spectroscopy is characterized by excitation photons (blue arrow) entering a tissue at wavelength λ_{ex}, propagating according to the tissue optical properties (absorption coefficient μ_{ai}, scattering coefficient μ_{si}; i=layer, all μ=f(λ)) at the excitation wavelength, being absorbed and isotropically re-emitted as fluorescence by a fluorophore (F_1, F_2; green and red stars), and fluorescence photons propagating back to the tissue surface according to the tissue optical properties at the emission wavelength. Tissue optical properties are frequently different in each layer of a multi-layered tissue, impacting the photon trajectories in each layer. Upon exiting from the tissue surface, the photons (green and red arrows) can be collected by fiber-optic probes and sent to a detector. The detected fluorescence intensity spectrum contains information about the fluorophores in each tissue layer. Measured data can be analyzed to characterize the sample and extract tissue information, including fluorophore concentrations and tissue optical properties.

Table 1.1 introduces common values of the optical properties that can be employed to mathematically model a tissue construct that contains any combination of four common endogenous fluorophores discussed in the applications of this chapter: NADH, FAD, keratin, and collagen. These values can be measured experimentally or obtained from literature. These optical parameters can be employed in mathematical models to predict photon propagation and optimize experimental setups. The values for each optical property are dependent on the components of the sample and the wavelength of light

employed to interrogate the sample, with different values used for modeling excitation and fluorescence light.

Table 1.1 Approximate ranges for optical properties of biological tissue [14,35,36].

	NADH	FAD	Keratin	Collagen	Tissue
Φ	0.02 – 0.1	0.03	0.25	0.1 – 0.4	-
τ (ns)	0.4 – 2.5	3.0	4.0	4.5 – 6	-
μ_{afx} (cm^{-1})	~ 0.2 – 6.1	~ 0.9	~ 0.5	~ 0.3 – 1.5	-
μ_a (cm^{-1})	-	-	-	-	0.1 – 30
μ_s (cm^{-1})	-	-	-	-	40 – 500
g					0.85 - 0.98

Φ: fluorescent quantum yield, τ: fluorescent lifetime, μ_a: absorption coefficient, μ_s: scattering coefficient,
μ_{afx}: fluorophore absorption coefficient, g: anisotropy

1.4.4 Additional experimental considerations

To avoid altering or damaging specimens, careful consideration must be given to the experimental conditions employed for optical excitation and detection. Photobleaching is a phenomenon that can cause a fluorophore to be permanently damaged and unable to undergo fluorescence events [37]. In fluorescence spectroscopy measurements, photobleaching is seen as a reduction in detected fluorescence over repeated measurements of a sample [38]. Methods to reduce photobleaching include reducing the excitation laser energy or limiting the excitation time.

Another consideration is the pressure with which the optical-probe is brought into physical contact with the tissue specimen. Probe pressure has been shown to impact optical spectroscopic measurements including measured fluorescence [39,40] and

reflectance [41]. Measurements are impacted from increased probe pressure resulting from tissue compression, possibly influencing local construct scattering and absorption properties. Therefore, a setup with minimal, controlled probe pressure is best suited to minimize possible affects for fluorescence measurements.

1.4.5 Environmental conditions

Controlled environmental parameters, like the background signal, temperature, pH, and oxygenation levels, are required to create repeatable measurements that accurately reflect the sample conditions. All of these experimental variables can change over time; therefore, to accurately compare measurements, measurement time should be kept to a minimum.

1.4.6 Background artifacts – absorption and fluorescence

Background artifacts can be inherent to a sample or originate due to the experimental setup, including absorbing chromophores, room lights, and culture media. Chromophores are molecules that do not fluoresce, but instead absorb excitation or emission photons, thus distorting measured optical spectra. To limit background artifacts, spectra should be background corrected to account for room lights prior to each measurement [31] and acquisition time should be minimized.

Culture media present when measuring cells or constructs can produce background fluorescence or cause excitation attenuation due to absorption from any of the variety of nutrients, cofactors, and other molecules present. There are two common techniques to limit the influence of culture media: employ phenol-red free media [42,43] or prior to measurement, wash the sample construct in phosphate buffered saline (PBS) [44],

although this alters the sample's physiological conditions and could impact measured fluorescence compared to native culture conditions.

Additional background fluorescence can occur when trying to measure human tissues, cells atop a highly-fluorescent collagen scaffold, or once a construct is implanted into a patient, when blood absorption becomes a determining factor in the amount of signal attenuation. Analyzing the effects of both hemoglobin concentration and oxygenation quenching has been developed on tissue samples with spectral filtering modulation [45]. Similar background signal artifacts can be present when studying exogenous fluorophores, where endogenous fluorescence is a background artifact that should be accounted for during analysis [46].

1.4.7 Temperature, pH, and oxygenation

Common protocols developed for tissue-engineered constructs include culturing constructs in an incubator at 37°C with controlled pH and oxygenation to promote cell growth [47]. Often, measurements are made under sufficiently different or unmonitored environmental conditions. These environmental factors can significantly impact the subsequent fluorescence measurements, including temperature variations [48], pH [49,50], and oxygenation in cell studies [51] and tissue studies [52]. Oxygenation has also been shown to be an effective quencher of fluorescence [53].

1.4.8 Spectroscopic optical data

Often, qualitative and quantitative differences are observed in both wavelength- and time-resolved reflectance and fluorescence data. Traditionally, most researchers collect wavelength-resolved data, because wavelength-resolved instrumentation is readily commercially available and spectral data is often sufficient for accurate sample analysis.

However, time-resolved data, and in particular the collection of time-resolved fluorescence data discussed in this dissertation, is very useful when measured fluorophores have overlapping emission spectra (*e.g.,* free/bound NADH and FAD) or to isolate time-resolved fluorescence decays from a wavelength-regime where the fluorophore of interest has a higher signal contribution than the background signal. Both modalities can be employed to extract useful biological information from the studied sample, often being employed in parallel to extract maximum fluorescence information from a sample.

1.4.8.1 Wavelength-resolved data

Wavelength-resolved spectra can highlight local changes in fluorophore concentration, environmental changes, sample morphology attributed to scattering changes, and absorber concentrations [1]. Each fluorophore has a distinct absorption spectrum and a corresponding emission spectrum. In samples with multiple fluorophores, the measurement is a linear combination of each fluorescence emission spectrum. In tissues, many fluorophores present have well characterized wavelength-resolved fluorescence spectra. Therefore, these molecules can be preferentially excited with prior knowledge of their absorption spectra and analyzed post-measurement with published literature spectra or measurements on purified endogenous fluorophores [23] when photon propagation effects are also considered [27]. Similarly, scattering biomolecules and tissue absorbers (*e.g.*, hemoglobin and pigments) have distinct absorption spectrum that can be resolved with reflectance spectroscopy and post-measurement analysis.

1.4.8.2 Time-resolved data

Each fluorophore has characteristic time-resolved kinetics, represented by the fluorescence lifetime, tau (τ). The fluorescence lifetime is the average time spent by a fluorophore in the excited state and has been well characterized [54] for common biological components. Fluorescence is a radiative decay process that occurs typically on the order of nanoseconds [1]. Measured fluorescence decay data is the convolution of the intrinsic fluorescence decay and the instrument response function (a measurement characterizing the pulse profile of a detected excitation laser pulse). The most common fluorescence decay model is a linear combination of exponential decays, although alternative fitting algorithms can be employed, including stretched exponential [55], Laguerre deconvolution technique [56], and phasor analysis [57].

Extracting lifetime parameters can be rather straightforward, but interpretation can be difficult. Each fluorophore has a natural variability in its measured lifetime due to the complex sample environmental conditions that can affect decay behavior. Additionally, the number of parameters used to fit data can lead to high quality fits, which may or may not be unique. In a sample containing multiple fluorophores, the resulting lifetime measurement is a linear combination of each individual lifetime and the fluorescence quantum yield in the wavelength range studied [58].

1.4.8.3 Wavelength- and time-resolved data

Wavelength- and time-resolved fluorescence data can be collected simultaneously in order to provide additional sample information without adding to measurement time [27]. Depending on the application, both methodologies can be employed initially to determine if one data domain is sufficient, although both methodologies can be advantageous to

improve sample analysis and characterization [30,31]. Furthermore, tri-modal optical systems can be developed that sequentially collect wavelength-resolved reflectance, wavelength-resolved fluorescence, and time-resolved fluorescence data. Majority of data collection in this dissertation was performed with such a system, named the Reflectance and Fluorescence Lifetime (RFLS) spectrometer [27,31].

With the RFLS, steady-state reflectance, steady-state fluorescence, and one time-resolved fluorescence decay is measured for all collected wavelengths. The collected data shows promise for collecting diagnostically useful optical parameters (see Chapter 4). In Chapter 5, we discuss instrumentation that could improve the accuracy and diagnostic utility of the time-resolved collection of the RFLS through the simultaneous collection of wavelength- and time-resolved fluorescence data [24]; sample data is shown in **Figure 1.4**. Each data collection contains wavelength-resolved spectra and numerous time-resolved decays. **Figure 1.4A** is a three-dimensional matrix composed of both wavelength- and time-resolved fluorescence intensity data. Time-resolved decays can be extracted at each measured wavelength. In **Figure 1.4B**, the fluorescence decay was extracted at the wavelength of peak fluorescence intensity and fit to a single-exponential decay with a least-squares iterative fit. Extracted lifetime parameters compared very well to expected literature lifetimes [24]. The breadth of collected fluorescence data and high quality, accurate fit illustrates the promise for using time-resolved fluorescence instruments to monitor tissue-engineered constructs with multiple fluorophores present and varying environmental conditions.

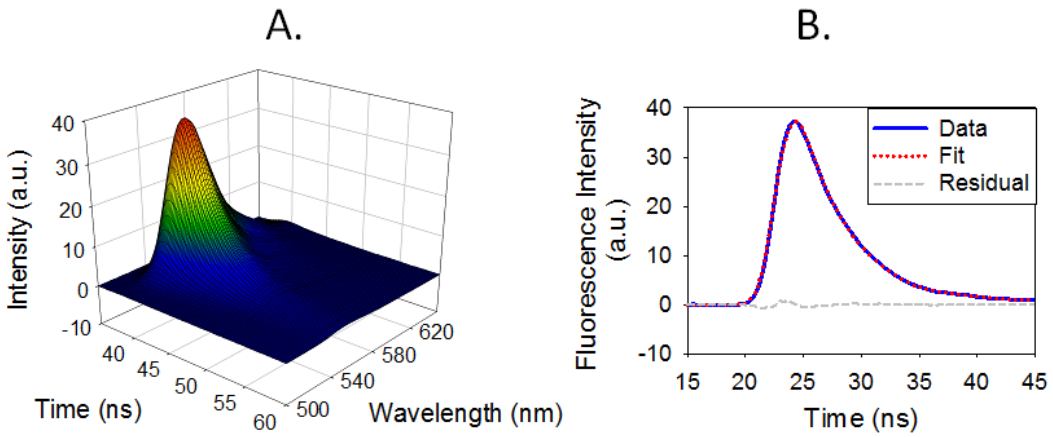

Figure 1.4. Wavelength- and time-resolved fluorescence data from a standard calibration fluorophore (Rhodamine 6G) is shown. (A) A three-dimensional matrix is composed of fluorescence time-resolved decays at user-selected wavelengths and a resulting wavelength-resolved spectrum. Time-resolved decays can be extracted and analyzed at each user-input wavelength, including the peak fluorescence intensity wavelength. In a complex sample with multiple fluorophores, decays can be extracted and analyzed at several wavelengths, yielding different decay dynamics vs. wavelength that reveal the relative proportion of each fluorophore in the sample. (B) The fluorescence decay at the wavelength of peak fluorescence intensity was extracted and analyzed via a least-squares iterative fit to a single exponential decay. Minimal residual shows a high quality fit [24]. (Used with permission)

1.4.8.4 Optical data analysis

A variety of analysis techniques can be employed to correct optical data and extract information potentially useful for sample classification and viability determination, including the tissue fluorophores present, their relative concentrations, their microenvironment, and the scattering and absorption coefficients of the sample. Many classification techniques have been applied to tissue fluorescence spectroscopy such as principal component analysis [59], linear discriminate analysis [4], partial least squares discriminate analysis [60], semi-empirical algorithms [23], and fluorescence ratio algorithms [31]. Techniques range in complexity from relatively simple to technically sophisticated in nature, and which to employ is application dependent. Often, several

techniques are evaluated before identifying the algorithm optimal for a specific application.

1.4.8.5 Correcting optical data

Many factors can impact the quality of fit and extraction of sample parameters from measured data. Of these, particularly notable are optical attenuation artifacts that can affect the spectral line-shape or influence the time-resolved measurements from a sample. Therefore, many techniques have been developed to correct measured tissue optical data for common attenuation artifacts [61], including blood absorption and oxygen quenching with fluorescence measurements [45] and in combination with reflectance measurements [23,62,63]. Carefully applying these techniques can enable the reconstruction of intrinsic optical data, thereby improving the quality and capabilities of data analysis.

1.4.9 Fiber-optic probe spectroscopy

Fiber-optic probes are employed for optical spectroscopy applications that are incompatible with free space light delivery and detection. Under these conditions, remote sensing with fiber-optic probes is convenient because it is non- or minimally-invasive, non-destructive, portable, and adaptable to measure a variety of samples, including future use in common clinical applications such as endoscopy or remote tissue sensing in space confined human cavities, such as the mouth. Many fiber-optic probes have been developed for use in biological tissue diagnostics, offering capabilities for tissue-construct monitoring [64]. Additionally, probes allow repeated measurements with selective sample interrogation, can be scanned over the sample volume to characterize a large tissue surface relatively quickly, and require little user training prior to use. The

probe geometries discussed below are not limited to a signal modality, being widely applicable for numerous spectroscopic applications, including fluoresce and reflectance spectroscopy discussed in this dissertation.

1.4.9.1 Quantitative models for probe design

Mathematical models have been developed to quantify fluorescence measurements from tissue samples [63] and tissue-engineered samples [65], including models based on the diffusion approximation [66], semi-empirical models [23,67], and Monte-Carlo (MC) simulations [32,33,68,69]. Accurate models provide the means of predicting measured fluorescence prior to experimentation, affording the opportunity to optimize probe design. These models are only as accurate as the input parameters [70] and only useful if the optimal probe design can be manufactured. For label-free sensing in tissue engineering applications, endogenous fluorophores and common tissue scattering and absorption properties have been well characterized and literature values can be employed as model inputs [13,54].

MC codes have been especially important in the development of optical spectroscopy applications, instrumentation setups, and appropriate fiber-optic probes [33,71]. An accurate MC code provides a flexible framework that can be employed to easily and accurately model a new optical setup or to predict the expected optical data obtained from measuring a new sample with input excitation and collection parameters. The MC approach can follow photon propagation for small path lengths (as small as 10-100 μm [71]), making it possible to model configurations where the same fiber is employed for both excitation and detection. MC models can be successfully applied to photon propagation in small tissue volumes, a regime where other models based on transport

equations lose accuracy [63]. MC codes for fluorescence have been successfully developed to model human tissue [69] as well as tissue-engineered constructs [72]. Before spending the time and resources for probe development, having the ability to predict the optimal probe design can be an invaluable tool.

1.4.9.2 Probe Design

Fiber-optic probe geometries have been developed and employed for a wide range of biomedical optical spectroscopy sensing applications [64,73,74]. Probe design is dependent upon the optical technique being employed; however, many probe geometry concepts can be adapted for different modalities. For example, ball lenses have been used for both fluorescence [75] and Raman spectroscopy [76].

Several important choices are made when designing a probe, including the number of excitation and emission fibers and their diameters, the excitation and collection geometry, and the method for coupling the fiber-optic probes to the sample. Also, careful consideration must be given to the fluorophores under investigation, where they are located in the sample, the sample volume to study, the scattering and absorption properties of the sample, background signal present, environmental factors (temperature, pH, oxygenation, probe pressure), and any external size constraints on the fiber-probe geometry.

Figure 1.5 provides an overview of several fiber-probe geometries that can be employed for the detection of fluorescence from tissue-engineered constructs. In particular, arrangements are included with fiber probes normal to the tissue surface with varying configurations for excitation and collection (**Figure 1.5A-1.5D**), with angled fibers (**Figure 1.5E**), with a ball lens (**Figure 1.5F**) and with beveled fibers (**Figure 1.5G and**

1.5H). Probes best used for measuring fluorescence from bulk tissues are located in the top row of **Figure 1.5**. Probes best used for measuring fluorescence from controlled depths within a tissue are located in the bottom row of **Figure 1.5**.

Figures 1.5A and **1.5B** illustrate the two simplest fiber-probe geometries to employ for experiments in scattering media. The excitation photons enter the tissue according to the optical fiber's numerical aperture, but due to light scattering in the medium, this creates an optical glow ball dependent on the scattering coefficient of the sample, but on the same order of size as the fiber diameter. Detected fluorescence photons are most likely to originate within this glow ball volume [32,77].

When employing the optical setup in **Figure 1.5B**, the source to detector fiber separation has a significant impact on the path detected photons travel. Here, the detected fluorescence photons are most likely to travel along a parabolic shape, with the depth traveled related to the source to detector fiber separation, also dependent on scattering coefficient.

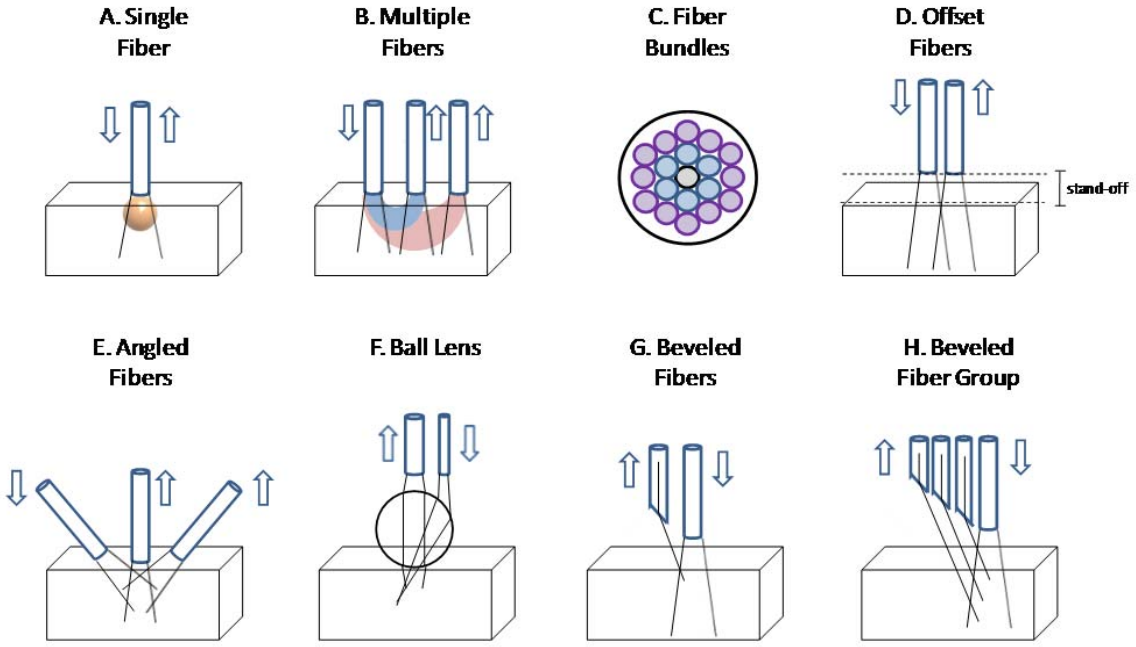

Figure 1.5. Fiber-optic probes for tissue spectroscopy have been developed using a variety of geometries, as illustrated here [64]. (A) Probe that uses a single fiber for both excitation and detection. The excitation light propagates into the turbid media and creates a glow ball of excitation light; detected fluorescence photons also originate within the glow ball. (B) Probe with a single source fiber and multiple detector fibers positioned at various distances from the excitation fiber. This probe can detect photons that traveled deeper into the tissue than in (A), with larger depth penetration for increased center-to-center spacing. Average classical photon path are shown between each fiber by the parabolic volumes. (C) A ring fiber bundle is employed to detect the same fluorescence information as in (B), but more fluorescence is detected with multiple source or detection fibers. Additionally, several center-to-center fiber spacing can be employed to detect different sample depths. Each concentric ring of fibers (gray and black) represents collection fibers with a fixed center-to-center spacing relative to the central white fiber. Employing concentric rings of fibers for excitation or emission detection can increase the measured fluorescence intensities. Fiber rings can be employed for either excitation or detection, with modifications interrogating different photon paths. (D) A vertical offset is introduced between the fiber probes and the sample surface to predominately excite and detect from a more superficial depth than in either (A) or (B). (E) Probe in which the fibers are angled relative to the sample. Angled excitation and detection promotes the detection of photons to propagate to shallower paths and thus detected fluorescence originates from shallower tissue depths. (F) A ball lens is employed to excite fluorescence in the upper layer of a sample. The detected fluorescence has been shown to be from a more superficial layer than that in (A) and (B) [78]. (G, H) Beveled fibers are employed that function similar to the angled fiber in (E) without needing to change probe orientation relative to tissue surface. (H)

Beveled fibers can be designed to detect fluorescence from different sample layers or depths [79].

1.4.9.3 Fiber-optic probe geometries

An important concern when selecting experimental probe geometry is the sample depth interrogated. The exact sample volume interrogated can be determined by employing Monte Carlo or diffusion photon propagation models. However, rough approximations can be provided for the upper and lower rows of **Figure 1.5**. For the upper row, sample depth analyzed is on the order of the center-to-center fiber spacing employed [80,81] (*i.e.* ~1 mm^3 sample volume analyzed with 600 μm diameter probes at small center-to-center spacing). For the bottom row, experimental set-ups are designed to mimic confocal microscopes with thin sectioning capabilities [74,79] (*i.e.* preferentially isolating a measurement top-layer thickness on the order of < 500 μm).

1.4.9.3.1 Fibers perpendicular to tissue

One of the simplest probe designs employs a single optical fiber (or multiple optical fibers) oriented perpendicular to the tissue surface [9,68,82]. When such a probe is placed in contact with tissue, excitation photons create a glow ball (**Figure 1.5A, B**), with photon excited volume diameter related to the scattering coefficient of the sample that has a diameter on the order of magnitude of the probe diameter, dependent on the scattering coefficient. Common applications involve bulk samples where fluorescence is detected from a large sample volume.

For a single fiber, a shallower sample layer is studied and more signal is generally detected, as the light photons travel a shorter path before detection [68]. For multiple probe geometries, the excitation photons generating detected fluorescence photons travel

a longer and relatively deeper path prior to detection, encountering more scatterers, absorbers, and fluorophores in optical paths that are parabolic in shape, based on the sample optical scattering properties [83]. Detection depth depends on the diameter of the fibers employed and the center-to-center probe spacing (**Figure 1.5B**), with smaller fiber diameters and smaller center-to-center spacing detecting shallower depths.

A MC study to analyze the effects of numerical aperture, fiber diameter, source-collection fiber separation distance, and fiber-tissue spacer thickness in multi-fiber probes geometries designed for fluorescence spectroscopy [68] predicted several experimental effects. These include that increases in numerical aperture could increase the detected signal without changing the origin of fluorescence. For example, increasing the probe to tissue surface standoff distance promotes probing a more superficial depth, shrinking both excitation and collection fibers promotes detecting fluorescence from a superficial depth, and increased center-to-center source detector fiber-optic probe spacing results in homogenous sample fluorescence measurements because detected photons have a wide-range of optical paths before being collected. Each finding should be considered when designing or implementing a fluorescence spectroscopic measurement with a multi-fiber setup.

1.4.9.3.2 Angled fibers

As with the probes described above, angled probes can be designed using Monte Carlo codes and validated on tissue-simulating phantoms before use on tissues. Angled excitation or collection fibers can be employed to achieve depth selectivity within a sample [72,84] and to increase depth selectivity in multilayered epithelial tissues [84,85].

Such probe geometries employed are easily translatable to tissue-engineered constructs which mimic similar tissue geometries.

Another approach to angle the excitation light is to employ beveled fibers, similar to the sketch in **Figure 1.5H**. This model was employed for elastic light scattering [79], but the probe design could be employed for fluorescence spectroscopy with minimal alterations. The model tested a developed probe with 110 μm diameter beveled fibers (35°, 40°, 45°). Predictions showed that depth resolution between ~350 μm and ~1200 μm could be achieved and confirmed with a three-layer scattering phantom and that a 40° bevel angle was optimal for depth resolving measurements on tissue-simulating phantoms mimicking oral precancer and *in vivo* on normal human oral mucosa. Beveled fibers could be manufactured to mimic the angled fiber results while not increasing the outer diameter of a stand-along probe due to the bending radius of the tilted fiber, a setup that can be employed when sectioning is desired but the probe outer diameter is a limiting design factor.

1.4.9.3.3 Lens-coupled fibers

Fiber-optic probes coupled with lenses (such as an objective lens or ball lens) can be employed to achieve fluorescence depth selectivity. These setups often attempt to mimic the depth selection of a microscope without requiring the additional expense and bulk of microscopy equipment. Advantages to employing such setups include a smaller fiber bundle setup that is desirable for clinical measurements. Similar probes have been employed for Raman spectroscopy [76].

When compared to measurements with fibers perpendicular to the sample, employing a ball lens was found to extract 3.8 times and 0.74 times as much fluorescence from the top

and bottom layers, respectively [78]. This experiment highlights that fiber-optic probe and optical lens geometries can lead to greater optical interrogation from superficial sample depths, useful when interrogating an epithelial cancer or thin tissue-engineered construct. Fiber-optic probes incorporating both beveled fibers and ball lenses have been designed and simulated for fluorescence spectroscopy measurements with improved depth-resolution [86]. Depth-selective probes have also been employed to analyze samples at a constant, superficial depth for reflectance spectroscopy [74]. With minimal to no changes in design, this probe could be employed for fluorescence. Confocal and multiphoton-excitation fluorescence spectroscopy

Inhomogeneous tissue-engineered samples, such as layered constructs, require spectroscopic techniques that preferentially excite fluorophores in a single layer of the construct, possibly at some preferred depth. These specifications are difficult to achieve using fiber-optic probes. Conventional applications to achieve sample sectioning include histology (destructive in nature) or other methods of sample staining. However, living tissue-engineered constructs can be analyzed with confocal and multiphoton-excitation fluorescence spectroscopy in a non-destructive and non-harming manner. Therefore, confocal and multiphoton spectroscopies have been employed to optically section thick biological samples down to thicknesses comparable to a cellular layer (a few μm), [87], thereby reducing the presence of background fluorescence from additional layers [88,89]. Confocal and multiphoton-excitation fluorescence spectroscopies are newly applied in the field of regenerative medicine, with few reported studies. Neither of these applications will be discussed in this dissertation, but are important to consider for future work due to the improved spatial resolution possible.

1.4.10 Example Applications

Following is a brief introduction to studies performed with optical spectroscopy. It is meant as an overview of the types of studies performed and not a thorough scientific review.

Applications of optical spectroscopy include sensing alterations in extracellular matrix collagen, including changes related to polymerization and temperature (attributed to alterations in collagen content), thermal stressing of collagen constructs to detect reversible or irreversible changes to collagen [90], detecting the viscoelasticity of tissue-engineered cartilage samples by monitoring type II collagen [91,92], and monitoring articular cartilage samples by studying extracellular collagen and intracellular NADH [27]. Furthermore, an important application of fluorescence spectroscopy is to monitor cellular or tissue metabolism. It has been reported that NADH and FAD are natural biomarkers for cellular metabolism. In addition, a ratiometric method to evaluate cellular metabolism was developed with NADH and FAD fluorescence [16]. Therefore, characterizing the fluorescence properties of these endogenous fluorophores is the first step toward the accurate quantification of cellular viability.

1.4.11 Clinical need for non-invasive optical diagnostics

Optical spectroscopy provides a useful tool for interrogating human tissues *in vivo* and tissue-engineered constructs, enabling targeted, selective, quantitative, and non-invasive techniques to assess tissue health and disease status. While optical spectroscopy has been widely investigated as a diagnostic technique to assess tissue status, it has only recently been applied to studies in regenerative medicine. For improved human disease detection,

a primary obstacle is improving quantitative detection of cancer at early stages before the disease has become incurable [93]. For tissue engineering, a primary obstacle for the clinical translation of "cell-scaffold products" is known to be "the development of appropriate *in vitro* and *in vivo* testing and characterization methods [10]."

1.5 Dissertation Objectives

With an understanding of the advantages and common uses of optical spectroscopy, this dissertation details employing steady-state reflectance, steady-state fluorescence, time-resolved fluorescence, or combinations thereof to address two clinical challenges: (1) improved detection of pancreatic disease and (2) assessing wound healing of *in situ* tissue-engineered constructs.

Specific Aim 1: To verify and validate a semi-empirical model of steady-state reflectance for quantitative optical assessment of pancreatic disease from tissue-simulating phantoms and *ex vivo* human pancreatic data. A photon-tissue interaction (PTI) model was previously developed and employed to extract optical absorption and scattering parameters from human *ex vivo* pancreatic tissues. Here, we will verify the PTI model with measurements of tissue-simulating phantoms with varying absorption and scattering properties and validate the model with measurements of *ex vivo* human pancreatic tissues with varying absorption over repeated measurements at unique sites.

Specific Aim 2: To assess *in vivo* feasibility of optical spectroscopy, analyzing diagnostic utility of steady-state reflectance, steady-state fluorescence, and time-resolved fluorescence measurements. The first-ever *in vivo* optical spectroscopic measurements of human pancreatic tissues will be collected with clinically-compatible instrumentation during open surgery. Diagnostic utility of *in vivo* measurements will be assessed with site-matched *in* and *ex vivo* measurements of steady-state reflectance, steady-state fluorescence, and time-resolved fluorescence. For the first time, diagnostic utility of time-resolved fluorescence measurements of *ex* and *in vivo* measurements will be assessed with a rigorous classification model.

Specific Aim 3: To design and develop instrumentation for rapid collection of wavelength-time matrices. Clinically-compatible instrumentation will be developed to collect wavelength-time matrices, three-dimensional data sets containing numerous wavelength-resolved fluorescence decays. Future potential to assess *in vivo* biological tissues will be discussed.

Specific Aim 4: To assess post-implantation wound healing of tissue-engineered constructs with diffuse reflectance spectroscopy. For the first time, depth-sensitive diffuse reflectance spectroscopy will be employed to assess post-implantation construct wound healing in an *in situ* murine model to distinguish healthy from compromised constructs.

1.6 Dissertation Overview

Chapter 2 describes the verification and validation of a photon-tissue interaction model, verifying the model with measurements from tissue-simulating phantoms and validating the model with measurements from *ex vivo* human pancreatic tissues.

Chapter 3 describes the first-ever *in vivo* steady-state optical spectroscopy measurements of human pancreatic tissues during open surgery, comparing the diagnostic utility of *in vivo* measurements to a previously-collected *ex vivo* data set.

Chapter 4 describes the first-ever analysis of an *ex* and *in vivo* time-resolved fluorescence data set from human pancreatic tissues. A rigorous classification model was employed to account for intrapatient correlations during tissue classification.

Chapter 5 describes the development of novel, clinically-compatible instrumentation to collect wavelength-time matrices for enhanced time-resolved characterization of biological tissues.

Chapter 6 describes the assessment of post-implantation tissue-engineered construct wound healing in an *in situ* murine model with diffuse reflectance spectroscopy and corresponding analysis to distinguish healthy from compromised constructs post-implantation.

Chapter 7 describes the regulatory approval process for optical spectroscopic technology, outlining the necessary steps from idea conception, device development, human trials, and finally to clinical use.

Chapter 8 concludes the dissertation, emphasizing scientific contributions described in this dissertation and future work.

Chapter 2.
Verification and validation of a photon-tissue interaction model

2.1 Introduction

Reflectance spectroscopy has the potential to provide quantitative, minimally invasive tissue assessment for biomedical applications, such as detection of cancer [5,7,20,23,63,94-98], atherosclerosis [99], and monitoring of brain injuries [100], by providing tissue parameters related to optical scattering (including scatterer size and concentration) and absorption (including hemoglobin concentration and blood-oxygen saturation). These parameters can be extracted from reflectance data via mathematical models, including models developed from diffusion theory, Monte Carlo simulations, or semi-empirical equations [1]. Previously, we showed that a semi-empirical Photon-Tissue Interaction (PTI) reflectance model has the potential to extract diagnostically-relevant parameters related to tissue morphology (**Figure 2.1**) and biochemistry in the human pancreas [23,101]. The model mathematically transforms an average measured "canonical normal" pancreatic tissue reflectance spectrum into an accurate model for pancreatitis (by increasing the collagen concentration) and adenocarcinoma (by increasing the collagen concentration and the mean size of the cell nuclei).

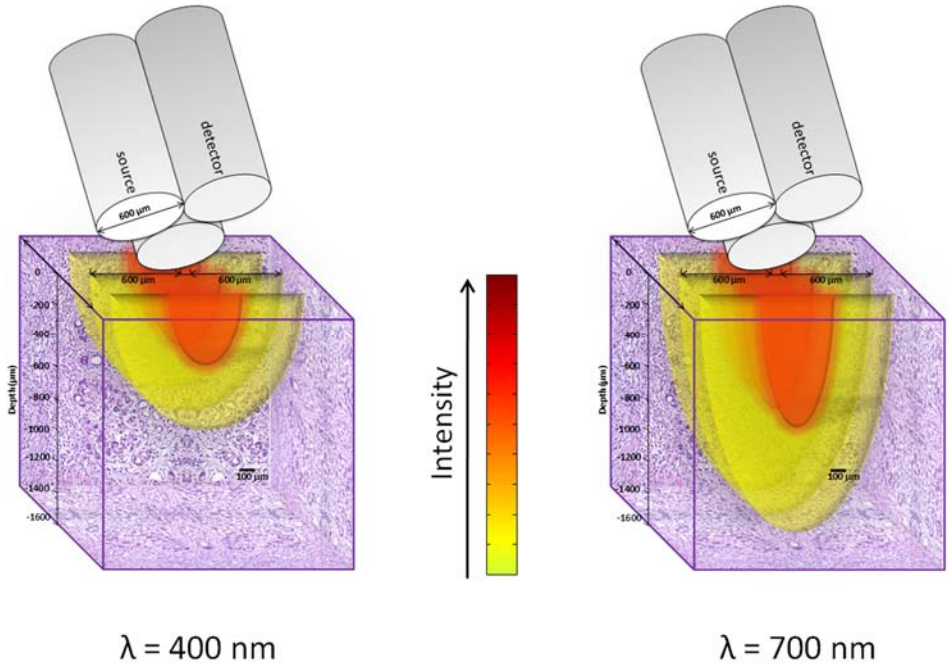

Figure 2.1. Conceptual illustration (to scale) of the distribution of 400 nm photons (left) and 700 nm photons (right) launched into a pancreatic adenocarcinoma tissue site with the fiber-optic probe configuration used in clinical studies (three adjacent identical fibers with diameter 600 µm, arranged in a triangular configuration). The probe appears tilted to show the bottom face of the fibers, but the optical axis of the probe was placed perpendicular to the tissue surface for all measurements reported in this study. The distribution of photons within the tissue (orange and yellow glowball) is related to scattering from morphological tissue features (shown here as purple-stained cell nuclei and pink-stained extracellular collagen fibers). The structural tissue components (such as cell nuclei and extracellular collagen fibers) responsible for wavelength-dependent scattering of incident light are not expected to change during short periods of data acquisition, even when hemoglobin concentration and blood oxygenation (and hence, wavelength-dependent absorption) are changing. Therefore, quantitative optical spectroscopy (with PTI modeling) should enable accurate and consistent scattering property extraction even when tissue absorption is changing due to variations in blood content. The histology images are from [102].

Assessing optical spectroscopic methods for tissue diagnostics [7] involves analyzing extracted tissue parameters to calculate their predictive accuracy for diagnostic classification [5,7,23,94-96,103]. Reported studies have analyzed a single measurement

for each tissue site [94,95], averaged repeated measurements [104], or considered multiple measurements acquired from the same site to be independent [5,7]. However, quantifying the precision of quantitative optical spectroscopy over the time-course of measurement is important for both *in vivo* studies of human tissue (where blood is dynamically flowing through the tissue, and measurements may be impacted by fiber-probe pressure and the puncture of a needle-based probe [105]) and *ex vivo* studies (where blood is draining from the tissue and becoming more oxygenated over time). Variations in blood content that occur *in vivo* can be linked to hypoxia and tissue vasculature [106,107], which are important considerations in clinical studies. Therefore, precise *ex vivo* quantification of tissue scattering parameters in the presence of notable changes to tissue hemoglobin concentration provides a proof-of-principle that the optical method should also be able to quantify these parameters *in vivo* (where the tissue scattering should be the same as that measured *ex vivo*, but the absorption could change significantly due to differences in blood content).

Here, we apply the PTI model to data collected from tissue-simulating phantoms and freshly excised pancreatic tissues. In Section 2.2, we describe the data acquisition procedures employed in this study. In Section 2.3, we validate the PTI model on tissue-simulating phantoms and then describe how individual tissue absorption and scattering parameters affect the PTI modeled reflectance of human pancreatic tissues. In Section 2.4, we show that tissue scattering parameters extracted from human pancreatic tissue reflectance measurements remain consistent even for tissue sites at which repeated measured spectra appear very different due to blood draining from the tissue over the course of measurement. Section 2.5 gives the conclusions of the paper.

2.2 Experimental methods

2.2.1 Prototype instrumentation

Prototype clinically-compatible instrumentation [27,31] was developed, as described in detail previously [5,31], to acquire reflectance spectra from tissue-simulating phantoms and human pancreatic tissues. Human pancreatic tissue measurements were obtained within 30 minutes of surgical resection at the University of Michigan (U-M) Medical Center. The human tissue study received approval from the Institutional Review Board of the U-M Medical School, and written consent was obtained from all patients.

Briefly, a tungsten-halogen lamp was employed as the reflectance source and light from the lamp was directed onto the surface of the sample with a source optical fiber. Reflectance photons were collected by a separate detector fiber placed adjacent to the source fiber (**Figure 2.1**). The probe also included a third optical fiber for collection of fluorescence photons (not described in this report). Light from the detector fiber was coupled to a spectrograph-coupled intensified charge-coupled device (ICCD) for spectral detection. The ICCD was wavelength-calibrated with a mercury-argon lamp (Oriel Instruments) with known emission wavelengths. The spectral response of the instrument was determined by measuring the spectrum of a tungsten-halogen lamp (Oriel Instruments, National Institute of Standards and Technology traceable) and dividing the measured spectrum by the theoretical spectrum from Oriel Instruments. Measured data were divided by the spectral response for calibration. The instrumentation also included components to acquire fluorescence data, although fluorescence data analysis is outside the scope of this report.

2.2.2 Tissue-simulating phantom measurements with two fiber-optic probes

For measurements on tissue-simulating phantoms, we employed two different fiber-optic probes: a probe containing fibers of 600 μm diameter (600/660 probe) and a probe containing fibers of 200 μm diameter (200/220 probe). The 660 and 220 denote the center-to-center spacing between source and detection fibers. Both probes had the configuration shown in **Figure 2.1**. The 200 μm diameter fiber-probe was designed for compatibility with *in vivo* pancreatic fine-needle aspiration.

Tissue-simulating phantoms were developed to mimic scattering and absorption properties of normal pancreatic tissues. The phantoms were mixtures of polystyrene microspheres (9 or 12 μm diameter, Bangs Labs) and hemoglobin (5 μM, 10 μM, 15 μM, 20 μM, and 25 μM concentrations, Sigma-Aldrich). Phantoms were measured in a 1 cm quartz cuvette, and measurements occurred at least 2 cm from the cuvette bottom to eliminate boundary effects. The absorption spectrum of a 5 μM solution of the hemoglobin (in deionized water) was measured with a spectrophotometer.

2.2.3 Clinical human pancreatic tissue data acquisition protocol, histopathological "gold standard," data pre-processing, and data exclusion

Optical data were acquired from pancreatic tissues from each of 9 patients within 30 minutes of excision. The spectrum of the light source was measured by placing a reflectance standard (Labsphere) in front of the instrument. Excess blood was wiped off of the tissue with gauze as needed, the on-site pathologist identified sites of interest on the excised tissue, and the optical probe was placed on those tissue sites for data acquisition. Some of these sites were beneath the surface of the tissue; in these cases the tissue was cut in order to provide access for the fiber-probe. At each site, the probe was

held in position by hand and monitored closely by the pathologist and the person taking the measurement. Repeated optical measurements (reflectance and fluorescence) were made at each site (with the exception of one site having only a single reflectance measurement) without removing the probe between measurements. The acquisition time for a single reflectance measurement was 1 second (obtained by averaging 10 measurements of 100 ms each), and the time between repeated reflectance measurements on a given site was approximately 30 seconds. When all measurements at a given site were completed, the probe was removed and the pathologist immediately excised a portion of the tissue from that site for standard histopathologic analysis. In this manner, optical measurements were obtained at multiple tissue sites from each patient and each tissue site had a specific histopathology reading, which served as the "gold standard" for the study.

Prior to data analysis, reflectance spectra were background-subtracted, corrected for the instrument response, and divided by the lamp spectrum (which was also background-subtracted and corrected for the instrument response). Then, all calibrated spectra were smoothed and normalized to peak intensity. Data analysis was performed on sites from which two usable measurements were acquired. Non-usable measurements (fluorescence signal-to-noise ratio < 25, or reflectance intensity at 550 nm < 10% of that at 650 nm, such that key scattering-related features were washed out due to extremely high levels of blood) were discarded. An additional five sites were removed due to artifacts from room lights. The resulting usable reflectance data set from 9 patients contained 42 sites (10 normal, 19 chronic pancreatitis, 13 adenocarcinoma) and 84 measured spectra (2 per

site). Chronic pancreatitis indicates chronically injured tissue that may also be inflammed.

It is important to note that in this study, variations in tissue blood content could not be experimentally controlled. Absorption-related variations were observed in the two reflectance spectra acquired at each site. These variations were presumably caused by changes over time in the concentration and oxygenation of blood in the freshly-excised tissues, known to occur during and to have impact upon post-resection measurements of optical spectra [31,108].

2.3 Photon-Tissue Interaction (PTI) model

2.3.1 Semi-empirical reflectance equations

A PTI model using semi-empirical reflectance equations [41,109] (as described previously [23,101]) was employed to extract parameters attributed to absorption- and scattering (**Table 2.1**) from the measured reflectance spectra. **Figure 2.2** illustrates the components of the PTI model.

Table 2.1. Tissue parameters that can be characterized by photon-tissue interaction (PTI) model of reflectance.

Scattering	Absorption
Morphological parameter related to cell nuclei, $<L>$	Total hemoglobin concentration, $[Hb]_{tot}$
Refractive index of cell nuclei, n_s	Blood-oxygen saturation, SO_2
Morphological parameter related to collagen fibers, ρ_c	Mean blood vessel radius, r_{bl}

As shown in **Figure 2.2**, the starting point of the PTI model is an average measured "canonical normal" reflectance spectrum, $N_{measured}(\lambda)$, obtained by averaging all reflectance measurements from histopathologically normal pancreatic tissue sites in the data set. This "canonical normal" spectrum is then mathematically transformed to produce a PTI model spectrum $R_{PTI}(\lambda)$ that can be fit to an individual reflectance measurement of "unknown" tissue type. This mathematical transformation takes the form:

$$R_{PTI}(\lambda) = N_{measured}(\lambda)\frac{R_{empirical}(\lambda)}{N_{empirical}(\lambda)} \qquad (2.1)$$

In **Eq. (2.1)**, $R_{empirical}(\lambda)$ and $N_{empirical}(\lambda)$ are quantities (obtained from semi-empirical equations) whose ratio is employed to scale the "canonical normal" reflectance into a PTI model prediction that can be fit to a reflectance measurement from an "unknown" tissue type. Both of these semi-empirical equations take the following general form $R(\lambda)$ [41,109]:

$$R(\lambda) = \mu_s'(\lambda)\exp\left(-\frac{C_{corr}\mu_a(\lambda)b}{\left[C_{corr}(\lambda)\mu_a(\lambda)\mu_s'(\lambda)\right]^c}\right) \qquad (2.2)$$

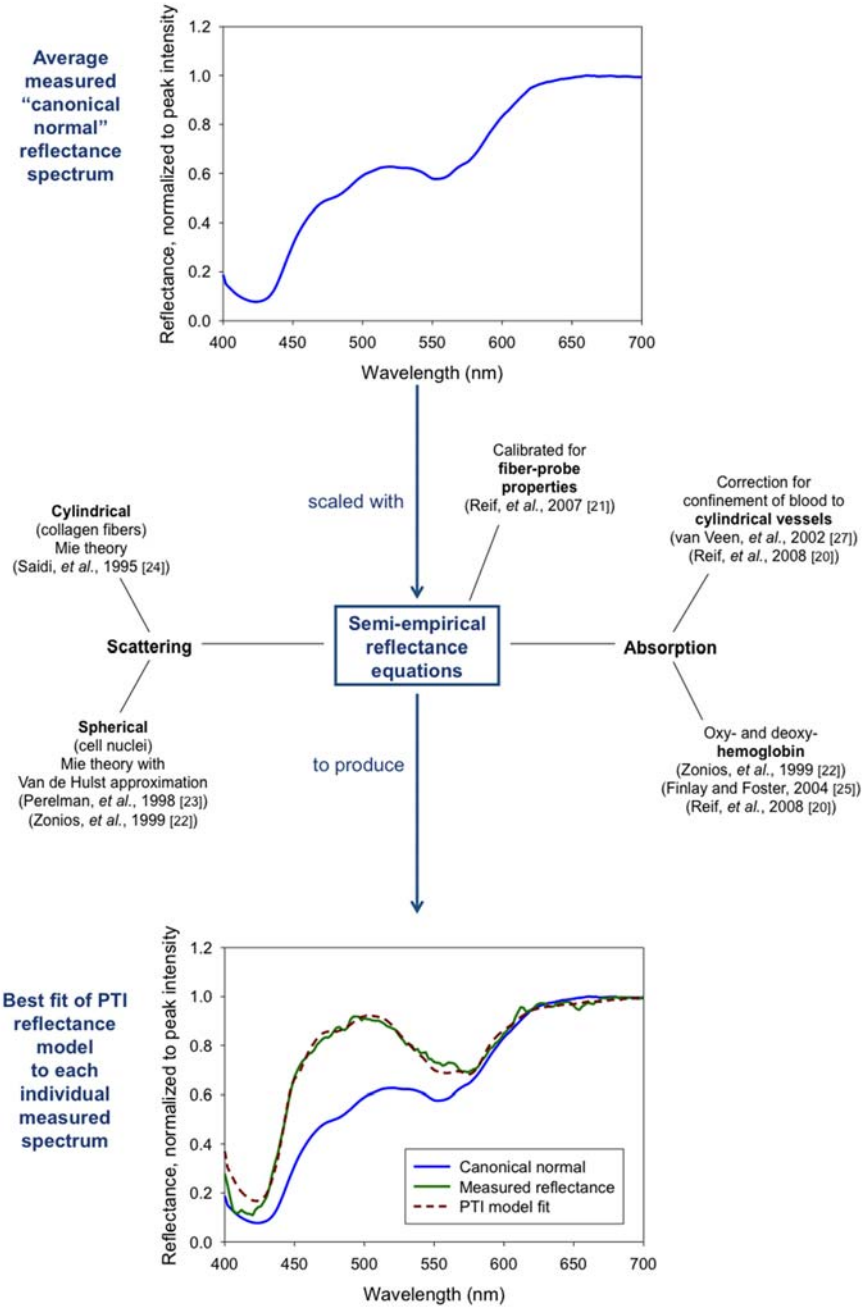

Figure 2.2. Conceptual illustration of the photon-tissue interaction (PTI) model employed to extract pancreatic tissue properties from measured reflectance spectra. The inset of the best fit PTI model is from [23].

In **Eq. (2.2)**, $\mu_a(\lambda)$ is the tissue absorption coefficient and $\mu_s'(\lambda)$ is the reduced scattering coefficient, defined as $\mu_s'(\lambda) = \mu_s(\lambda)(1-g)$, where g is the anisotropy [101]. The variables

b and *c* are related to tissue and fiber-probe properties [109]. Tissue scattering was attributed to cell nuclei (modeled as spheres [94,110] with mean diameter $<L>$ and refractive index n_s = 1.375) and collagen fibers (modeled as cylinders [111] with concentration $\rho_c = 3\text{x}10^6$ fibers/cm^2). Tissue absorption was attributed to oxy- and deoxy-hemoglobin [41,94,112], with a correction factor $C_{corr}(\lambda)$ that accounted for the confinement of blood to cylindrical blood vessels [113] with mean radius r_{bl} (set to 7 μm). From each reflectance measurement, a morphological parameter L/L_o and the total hemoglobin concentration $[Hb]_{tot}$ were extracted [23,101]. The morphological parameter ratio characterized changes in cellular morphology by analyzing spectral features attributed to cell nuclei diameter [101]. The value of L/L_o was previously shown to be larger for adenocarcinoma than for normal pancreatic tissue or pancreatitis, a result that agreed with histopathological observation [23,101].

2.3.2 Calibration of PTI model for different fiber-probe properties

The first step in fitting the PTI model to the reflectance data from tissue-simulating phantoms was to empirically obtain the calibration coefficients *b* and *c*. These coefficients were determined by scaling the reflectance from the phantom with 5 μM hemoglobin to that from the phantom with 10 μM hemoglobin. In this fitting procedure, the absorber (hemoglobin) and scatterer (polystyrene microsphere) concentrations, as well as the scatterer size and refractive index, were set to their true values in the PTI model. The scattering coefficient $\mu_s(\lambda)$ of the microspheres was calculated with Mie theory, using the refractive index of polystyrene reported in [27]. During the fitting calibration, the parameters *b* and *c* were freely varied between 0.05 and 0.99, while the

anisotropy g for the phantom with 10 μm hemoglobin was freely varied between 0.5 and 0.99. A constrained optimization algorithm extracted the values of b, c, and g for each probe configuration. The best fit between the PTI model and the measured reflectance had an error in fit of <1% for the 600/660 and <3% for the 200/220 probe (error function $E_R = \Sigma|R_{measured}(\lambda) - R_{PTI}(\lambda)|/\Sigma(R_{measured}(\lambda))$ from 400-760 nm). The values of b, c, and g extracted from these fits were b = 0.71, c = 0.28, and g = 0.875 for the probe with 600 μm diameter fibers and b = 0.72, c = 0.50, and g = 0.875 for the probe with 200 μm diameter fibers. These sets of coefficients were then used in the PTI model to extract phantom absorption and scattering properties (Section 2.3.3). For analysis of human pancreatic tissue reflectance measurements (Sections 2.3.4 and 2.4), the values of b and c were set to 0.22 and 0.2, respectively, following our previous publications [5, 6].

2.3.3 Verification of PTI model with tissue-simulating phantom measurements

To verify the ability of the PTI model to extract accurate absorption and scattering properties, two different tests were performed. First, for both fiber-probes described in Section 2.2.2, the reflectance measurement from the phantom with polystyrene microspheres and 5 μM hemoglobin (the "canonical normal" measurement for this study) was scaled to model the reflectance measurement from the phantom with polystyrene microspheres and either 10, 15, 20, or 25 μM hemoglobin (**Figure 2.3**). For each probe, the measured reflectance from the two experimental trials only deviated by ~2%, so the average of the two measurements was fit with the PTI model. The extracted values of b, c, and g for each probe (Section 2.3.2) were employed in this fitting procedure. **Figure 2.3(a)** shows the best fit of the PTI model to the averaged reflectance obtained with the

600 μm diameter probe (mean percent error in fit < 2%). **Figure 2.3(b)** shows the best fit of the PTI model to the averaged reflectance obtained with the 200 μm diameter fiber-probe (mean percent error in fit < 4%). The extracted diameter of the scatterers was accurate to within 1% for all hemoglobin concentrations, and the extracted concentration of the absorber was accurate to within 17%. The discrepancy between the percentage error in the absorption and the percentage error in the scattering was attributed to cross-talk between the absorption concentration parameter and the scatterer concentration parameter N_s. Fitting results extracted consistent optical scattering and absorption parameters from measurements of tissue-simulating phantoms with 12 μm diameter polystyrene microspheres (data not shown).

Second, the reflectance measurement obtained with the 600 μm fiber probe from the phantom with 9 μm diameter polystyrene microspheres and 5 μM hemoglobin was scaled to model the reflectance obtained with the 200 μm fiber probe from the phantom with 9 μm diameter polystyrene microspheres and 20 μm hemoglobin. The measured reflectance from the two experimental trials only deviated by < 4%, so the average of the two measurements was fit with the PTI model. For this case, the extracted values of b, c, and g for *both* probes (Section 2.3.2) were employed in the same PTI fitting procedure, and **Figure 2.4** shows the best fit of the PTI model to the averaged reflectance (mean percent error in fit < 5%). The extracted diameter of the scatterers was accurate to within 1% and the extracted concentration of the absorber was accurate to within 6%.

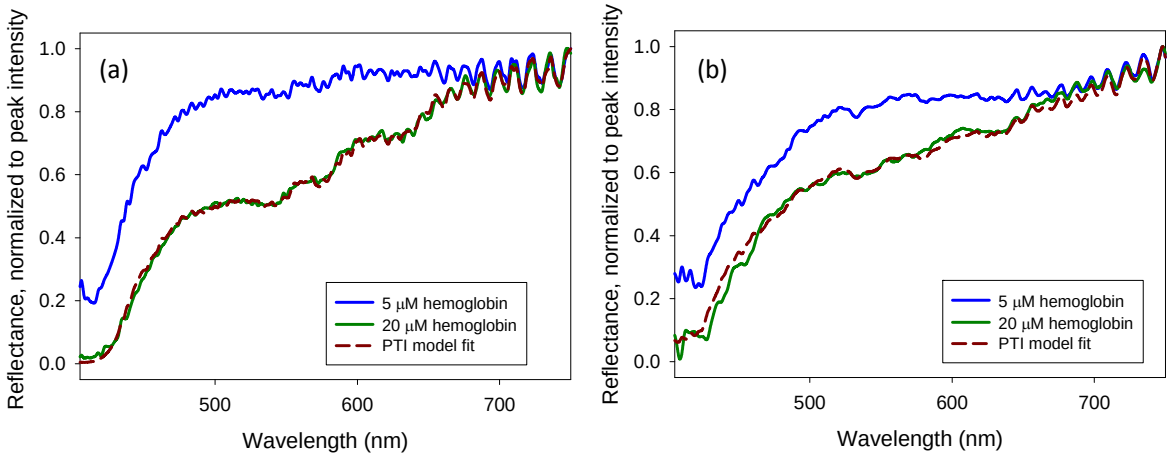

Figure 2.3. PTI model accurately scales reflectance measurements from tissue-simulating phantoms with 5 μM hemoglobin to those from phantoms with 20 μM hemoglobin. Measurements were obtained using fiber-optic probes with (a) 600 μm diameter fibers with center-to-center spacing of 660 μm and (b) 200 μm diameter fibers with center-to-center spacing of 220 μm. Both phantoms also included scattering from polystyrene microspheres with 9 μm diameter. PTI model fits extracted tissue optical parameters, including scatterer diameter and concentration, concentration of absorbers, and anisotropy. PTI model best-fits (shown) extracted scatterer diameter to within 1% and absorber concentration to within 17%.

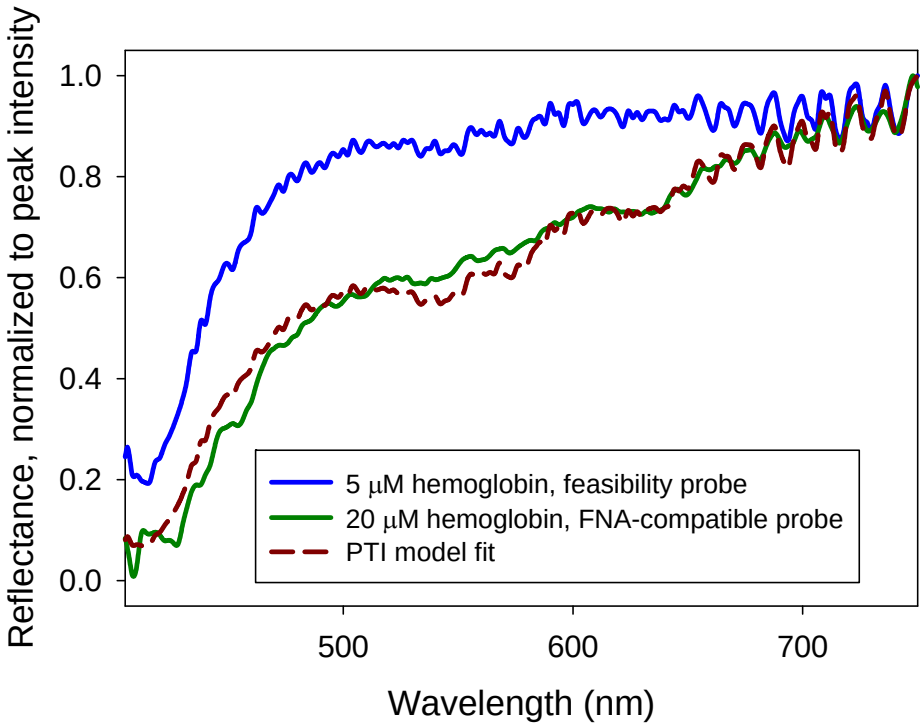

Figure 2.4. Demonstration of PTI model scaling measured canonical normal with 600/660 probe to measured reflectance obtained with 200/220 probe from a phantom with different absorption than the canonical normal. In this demonstration, the canonical normal was measured from a liquid phantom composed of 9 μm diameter polystyrene microspheres and 5 μM blood in deionized water with the 600/660 probe. The measured reflectance was measured from a liquid phantom of 9 μm microspheres, but with 20 μM blood and measured with the 200/220 probe. Scatterer diameter was extracted to < 1% error and absorber concentration was extracted to < 6% error.

2.3.4 Effect of scattering parameters on PTI reflectance model of human pancreatic tissues

Figure 2.5 illustrates how **Eqs. (2.1)** and **(2.2)** can be employed to mathematically transform an average measured "canonical normal" human pancreatic tissue spectrum (obtained here by averaging 20 reflectance measurements from normal pancreatic tissues) into a PTI reflectance model $R_{PTI}(\lambda)$ for pancreatic tissues with different scattering properties. In **Figure 2.5(a)**, the morphological parameter attributed to collagen fibrils ρ_c

is varied, and in **Fig. 2.5(b)**, the mean morphological parameter <*L*> is varied. In both cases, the region of the spectrum from 450-525 nm is most prominently affected.

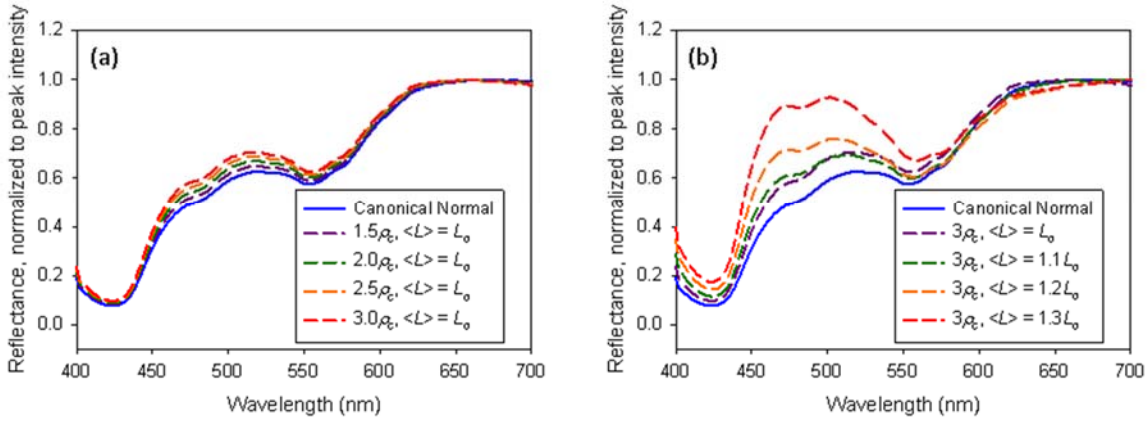

Figure 2.5. Effect of changes in two different scattering parameters on PTI reflectance model $R_{PTI}(\lambda)$ of human pancreatic tissue: (a) varying values of the morphological parameter attributed to collagen ρ_c and (b) varying values of the mean morphological parameter <L>. Changing the morphological parameter attributed to collagen has a subtle effect on the reflectance lineshape from 450-525 nm, while changing the mean morphological parameter size has a much more notable effect on the reflectance in this region.

Using **Figure 2.5** as a guide, **Figure 2.6** shows how some key features of the reflectance spectra from the PTI model (**Figure 2.6(a)**) correspond to average measured reflectance data from human chronic pancreatitis and adenocarcinoma (**Figure 2.6(b)**, [5]). First, the mean morphological parameter size is kept constant but the morphological parameter attributed to collagen is multiplied by a factor of three, shown in the medical literature to be indicative of both chronic pancreatitis and adenocarcinoma [114]. In this case, the PTI reflectance model (dot-dashed green line in **Figure 2.6(a)**) looks similar to the average measured reflectance from chronic pancreatitis (dot-dashed green line in **Figure 2.6(b)**). *This result is consistent with the observation at histopathology that chronic pancreatitis*

is characterized by increased extracellular collagen, but no significant increase in the mean size of cell nuclei (relative to normal tissue) [101].

Next, the morphological parameter attributed to collagen fibrils is kept at three times that of normal tissue, but the mean morphological parameter size $<L>$ is increased from its initial value of L_o to a value of 1.25x L_o. For this larger value of $<L>$, one can see the similarity between the PTI reflectance model (dashed red line in **Figure 2.6(a)**) and the average measured reflectance from adenocarcinoma (dashed red line in **Figure 2.6(b)**). *This result agrees with the observation at histopathology that adenocarcinoma is characterized by increased extracellular collagen and enlarged cell nuclei (relative to normal tissue)* [101].

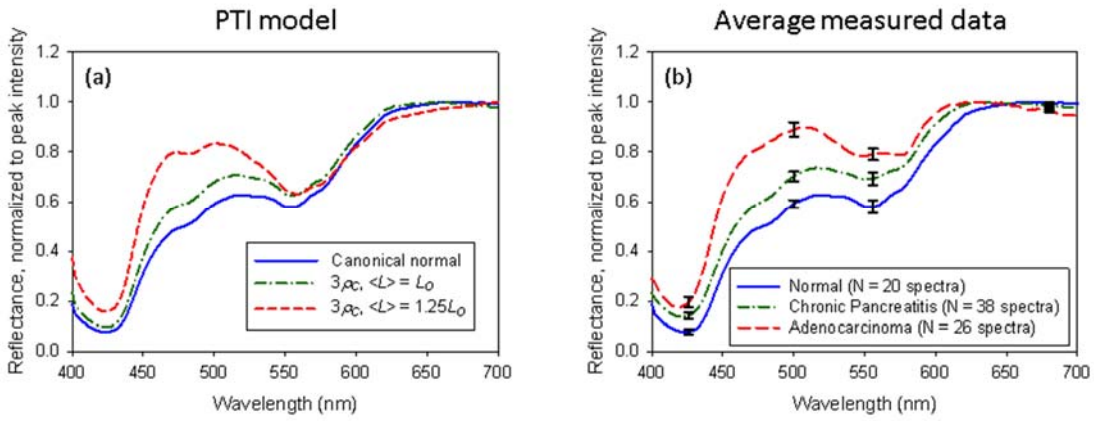

Figure 2.6. Demonstration of PTI reflectance models $R_{PTI}(\lambda)$ for various combinations of tissue scattering parameters (a), shown alongside average measured data from human pancreatic tissues [31] (b). When the morphological parameter attributed to collagen fibrils is increased to three times that of normal pancreatic tissue but the mean morphological parameter is left unchanged (dot-dashed green line in (a)), there is a notable similarity between the PTI model and the measured data from chronic pancreatitis (dot-dashed green line in (b)), relative to normal (blue lines in (a) and (b)). When the mean morphological parameter is increased to 1.25 times that of normal tissue, and the morphological parameter attributed to collagen fibrils is kept at three times that of normal tissue, the PTI model (dashed red line in (a)) looks

similar to the average measured reflectance from adenocarcinoma (dashed red line in (b)), relative to normal. The increase in morphological parameter attributed to collagen fibrils provides a subtle change in the reflectance from 450-525 nm, while the increase in nuclear morphological parameter size is responsible for the more pronounced change in the reflectance in this region. The error bars in (b) represent the standard error.

2.4 Consistency of PTI model of human pancreatic tissue when blood concentration varies

2.4.1 Degree of difference between repeated measurements at each human pancreatic tissue site

Changes in pancreatic tissue blood concentration at the measurement site will affect the optical absorption properties of the tissue. However, these changes should not significantly affect the dependence of the tissue reflectance spectrum on the disease-related alterations in tissue scattering modeled in **Figures 2.4** and **2.5**. To confirm this hypothesis, we analyzed the subset of human pancreatic tissue sites for which there was a significant degree of difference between the two repeated reflectance measurements $R_1(\lambda)$ and $R_2(\lambda)$. These sites were identified by using the manually-selected criterion $\Sigma |R_2(\lambda)-R_1(\lambda)| > 4.25$. Here, Σ denotes a sum over all wavelengths between 400 nm and 700 nm (the same range over which the PTI model was fit to each reflectance spectrum). Using these criteria, 26 of the 42 sites exhibited significant differences between the two measured reflectance spectra in the 400-450 nm and 525-600 nm ranges, where absorption from hemoglobin is known to visibly affect reflectance. These differences were attributed to variations in the amount of blood during the time-course of the experiment. For the other 16 sites, there was no significant variation between the two reflectance measurements (illustrating the capability of the instrumentation and experimental protocol to provide consistent measurements).

2.4.2 Procedure to fit PTI model to measured human pancreatic tissue reflectance spectra

The PTI model was fit to each of the two reflectance spectra acquired from all 42 sites. In the fitting procedure [23], representative parameters of the cellular nuclear refractive index n_s and morphological parameter attributed to collagen fibrils ρ_c were kept constant (at values of n_s = 1.375 and ρ_c = 9x10^6 fibers/cm^2, respectively [101,111,114]), while representative parameters of a morphological parameter L/L_o (attributed to varying size and shape of cell nuclei) was varied from 1.0 to 1.5 (in steps of 0.1), the blood-oxygen saturation SO_2 was varied from 0.1 to 0.9 (in steps of 0.1), and the total hemoglobin concentration $[Hb]_{tot}$ was varied over an expanded range (from 1 μM to 401 μM, in steps of 5 μM) to better account for the blood content of the tissue.

For each measurement, the best fit of the PTI model to the data was defined to be the fit that minimized the cost function $C_R = \Sigma|R_{measured}(\lambda) - R_{PTI}(\lambda)|$, where $R_{measured}(\lambda)$ was the measured reflectance spectrum, $R_{PTI}(\lambda)$ was the PTI reflectance model, and Σ represented a sum over all wavelengths from 400-700 nm. For each site, the values of L/L_o and $[Hb]_{tot}$ extracted from the best fits were compared for the two repeated measurements. The parameter L/L_o was used in this analysis because changes in L/L_o have previously been shown to distinguish the adenocarcinoma spectra from the normal and chronic pancreatitis spectra [101].

2.4.3 Consistency of scattering properties extracted from repeated measurements at each human pancreatic tissue site

Figure 2.7(a) shows two measured reflectance spectra (solid lines) from a single adenocarcinoma site, along with the corresponding fits of the PTI model (dashed lines) to each spectrum. According to the criterion described in Section 2.4.1, the two

measurements shown in **Figure 2.7(a)** were not considered to be significantly different. As expected, the extracted values of the morphological parameter L/L_o and the mean reduced scattering coefficient $<\mu_s'>$ were identical for the two repeated measurements.

Figure 2.7(b) shows two measured reflectance spectra (solid lines) from a second adenocarcinoma site, along with the corresponding fits of the PTI model (dashed lines) to each spectrum. Here, according to the criterion described in Section 2.4.1, the two measurements were considered to be significantly different. Indeed, the $[Hb]_{tot}$ values extracted from the fits to repeated measurements were different. However, the extracted values of the morphological parameter L/L_o and the mean reduced scattering coefficient $<\mu_s'>$ were still identical for the two measurements, demonstrating the ability of the PTI model to extract consistent values of the tissue scattering properties even when there are noticeable variations in the amount of blood at a given site.

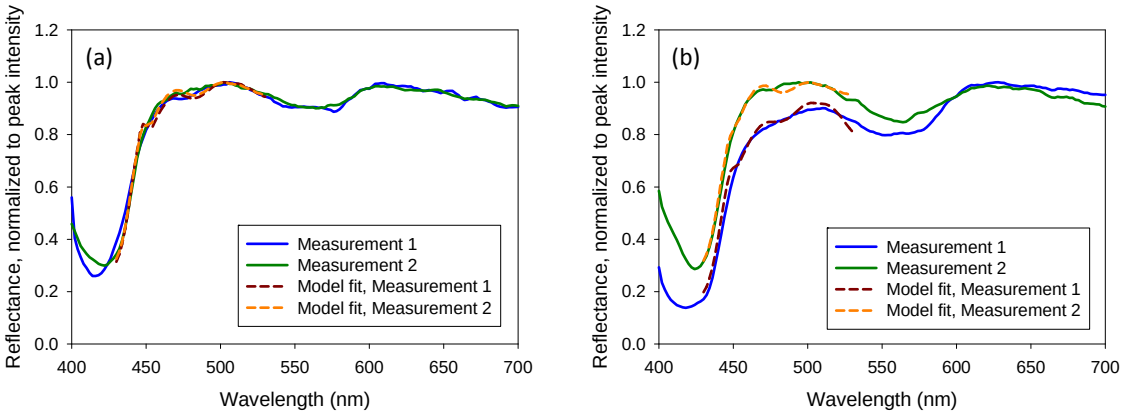

Figure 2.7. Pairs of reflectance measurements (solid blue and green curves) acquired from two different pancreatic adenocarcinoma sites ((a) and (b)), shown with the corresponding fits of the PTI model to the measured spectra from 430-500 nm (dashed red and orange curves). For the site shown in (a), the two measured spectra were very similar, and the values of the total hemoglobin concentration [Hb]tot, the morphological parameter L/Lo, and the mean reduced scattering coefficient $<\mu_s'>$ extracted from the two spectra were identical ([Hb]tot = 1 μM, L/Lo = 1.3, $<\mu_s'>$ = 18.7 cm^{-1}). For the site shown in (b), the two measured spectra were significantly different (likely due to changes in absorption caused by the draining of blood from the freshly excised

tissue), and the [Hb]tot values extracted from the two spectra differed by 15 μM ([Hb]tot1 = 16 μM, [Hb]tot2 = 1 μM), but the values of the morphological parameter L/Lo and mean reduced scattering coefficient $<\mu_s'>$ extracted from the two spectra were still identical (L/Lo = 1.3, $<\mu_s'>$ = 18.7 cm^{-1}). This result illustrates the ability of the PTI model to extract consistent values of tissue scattering parameters even when the blood content of the tissue changes over time.

Figure 2.8(a) shows a histogram of the differences between the total hemoglobin concentration values $[Hb]_{tot}$ acquired at the sites (N = 16) for which there was no significant difference between the two measured spectra (including the site shown in **Figure 2.7(a)**) according to the criterion described in Section 2.4.1. **Figure 2.8(b)** shows the corresponding histogram of the differences between the L/L_o values extracted from the two reflectance spectra extracted from each of these sites. The differences $\Delta[Hb]_{tot}$ and $\Delta L/L_o$ were defined as $[Hb]_{tot2}$-$[Hb]_{tot1}$ and $(L/L_o)_2$-$(L/L_o)_1$, respectively, where the subscripts 1 and 2 denoted the first and second measurements taken from a given tissue site. For 15 of these 16 sites (94%), the $[Hb]_{tot}$ values extracted from the two measurements differed by less than 10 μM. Furthermore, for this set of 16 sites, the average difference between the L/L_o values extracted from the two measurements was less than 1%. **Figure 2.8(b)** shows that for 15 of these 16 sites, the L/L_o values extracted from the two measurements were identical. In addition, the average difference between the $<\mu_s'>$ values extracted from the two measurements was less than 1%. *These results demonstrate the robustness of the data collection method and the stability of the PTI model of human pancreatic tissue.*

Figure 2.8(c) shows a histogram of the differences between the $[Hb]_{tot}$ values extracted from the two reflectance spectra acquired at the sites (N = 26) for which there were significant differences between the two measured spectra (including the site shown in

Figure 2.7(b)) according to the criterion described in Section 4.1. **Figure 2.8(d)** shows the corresponding histogram of the differences between the L/L_o values extracted from each of these sites. As expected, for 21 of these 26 sites (81%), the $[Hb]_{tot}$ values from the two measurements differed by at least 10 μM. However, the average difference between the L/L_o values extracted from the two measurements was less than 7%. **Figure 2.8(d)** shows that for 22 of these 26 sites (85%), the magnitude of $\Delta L/L_o$ was no greater than 0.1 (the step size for L/L_o in the PTI fitting procedure described in Section 2.4.2). The average difference between the $<\mu_s'>$ values extracted from the two measurements was less than 8%. *These results indicate that the PTI model extracted consistent values of human pancreatic tissue scattering properties even when the tissue blood content varied significantly.*

Over the entire set of 42 human pancreatic tissue sites interrogated in the study, the hemoglobin concentration varied by an average of 23 μM between the two measurements from a single site, but the mean morphological parameter and mean reduced scattering coefficient both varied by less than 6% between the two repeated measurements from a single site.

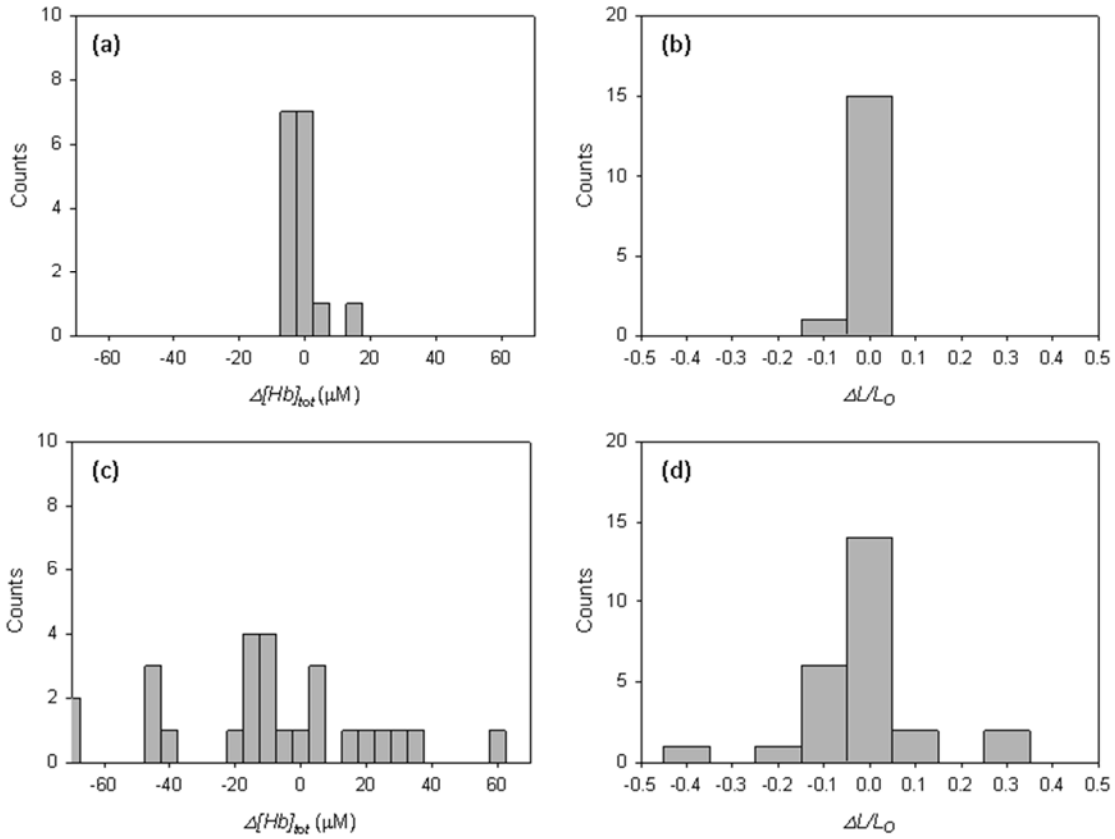

Figure 2.8. Histograms of differences in extracted values of the total hemoglobin concentration (Δ[Hb]tot) and morphological parameter (ΔL/Lo) for (a, b) the 16 pancreatic tissue sites with similar repeated reflectance measurements and for (c, d) the 26 pancreatic tissue sites with significantly different repeated reflectance measurements. (For ease of view, the bar at the far left of (c) represents two sites with Δ[Hb]tot values of -135 μM and -280 μM, respectively.) When the two reflectance measurements were not significantly different, the magnitude of Δ[Hb]tot (a) was less than 10 μM for 15 of 16 sites (94%), and the average difference between the two extracted L/Lo values (b) was less than 1%. When the two reflectance measurements were significantly different, the magnitude of Δ[Hb]tot (c) was 10 μM or greater for 21 of 26 sites (81%), but the average difference between the two extracted L/Lo values (d) was still less than 7%.

2.4.4 Potential for clinical diagnostic significance

For each human pancreatic tissue type, the five sites for which the two reflectance measurements were the *most different* from each other were determined by maximizing

the function $Diff(R_1(\lambda),R_2(\lambda)) = \Sigma(R_2(\lambda)-R_1(\lambda))$, where $R_1(\lambda)$ and $R_2(\lambda)$ were the two repeated reflectance spectra measured from each site and Σ represented a sum over the wavelengths from 400-700 nm. For this reduced data set, the mean L/L_o value for adenocarcinoma (L/L_o = 1.28) was still 22% larger than that of normal pancreatic tissue (L/L_o = 1.05) and 20% larger than that of chronic pancreatitis (L/L_o = 1.07). Using Wilcoxon rank-sum tests [29], the p-values for using L/L_o to distinguish adenocarcinoma from normal tissue ($p < 2\text{x}10^{-3}$) and to distinguish adenocarcinoma from chronic pancreatitis ($p < 7\text{x}10^{-3}$) were still statistically significant for this challenging subset of the data. These results suggest that the PTI algorithm has the potential to distinguish between different pancreatic tissue types even for tissue sites with notable variations in blood content.

2.5 Conclusions

Here, we have demonstrated the potential of quantitative tissue optical spectroscopy (using reflectance spectroscopy and a photon-tissue interaction model for data analysis) to provide consistent values of tissue scattering parameters at a given human pancreatic tissue site, even when the measured spectra at that site are varying noticeably over time due to changes in absorption from blood. The results reported here illustrate the feasibility of employing optical spectroscopy for consistent characterization of disease-related morphological and compositional changes in human pancreatic tissues, and these findings should also be applicable to a wide range of other tissue types. The optical diagnostic technique reported here, including the instrumentation and algorithms, is clinically-compatible for real-time characterization of tissue absorption and scattering *in vivo* in clinical settings, where blood concentration and oxygenation will vary over time.

Chapter 3.
In vivo optical spectroscopy for improved detection of pancreatic adenocarcinoma: a feasibility study

3.1 Introduction

Pancreatic adenocarcinoma has a five-year survival rate of only 6%, making it the 4th leading cause of cancer death in the United States (US) [115]. By 2020, pancreatic cancer is projected to become the 2nd leading cause of cancer death in the US [115]. Current diagnostic procedures are unable to accurately detect early stage disease [116], successfully diagnosing only 7% of early-stage pancreatic cancers [115]. As a result, only 20% of discovered pancreatic cancers are treatable with surgery. The challenges to accurate detection and characterization of pancreatic neoplasia include the relative inaccessibility of the organ, as well as the non-specific nature of symptoms. In particular, a stromal reaction with intense fibrosis is associated with both adenocarcinoma and chronic pancreatitis (chronically injured tissue). As a result, the sensitivity for diagnosing cancer in the setting of chronic pancreatitis (inflammation) has been reported to be only 54% when using the diagnostic procedure-of-choice for tissue acquisition in suspect pancreatic cancer, endoscopic ultrasound-guided fine-needle aspiration (EUS-FNA) [117].

Several studies have employed optical techniques for minimally invasive detection of cancer [118] in tissues including breast [7], cervix [119], colon [6,120], and esophagus [4]. Further, optical spectroscopy is compatible with clinical EUS-FNA procedures [105]. Optical techniques investigated in pancreatic tissues include optical coherence

tomography [121,122], needle-based confocal laser endomicroscopy [123], near-infrared spectroscopy [124,125], non-linear optical imaging [126], optical field effect analysis from duodenal tissues [127,128], diffuse optical tomography [129], and our own studies employing optical spectroscopy [5,23,31,101,130]. Advantages to our optical spectroscopy technology include addressing the primary medical need: improved and minimally invasive detection of pancreatic cancer in the presence of overall tissue inflammation.

Our approach examines the feasibility of optical spectroscopy for clinical pancreatic cancer diagnostics in four stages: (1) identify key features in human tissue spectra using an *in vivo* murine model (human pancreatic tumor xenograft), (2) perform *ex vivo* pilot study to optically detect human pancreatic malignancy, (3) verify and validate accuracy of a photon-tissue interaction (PTI) model, and (4) perform a human pilot study to assess feasibility *in vivo*. In Stage 1, measurements from *ex vivo* human adenocarcinoma tissues were shown to correspond well to *in vivo* measurements from a tumor xenograft [31]. In Stage 2, accurate detection of normal, chronic pancreatitis (inflamed), and adenocarcinoma tissues was achieved [5,23,101]. Malignant tissues were distinguished from benign tissues with sensitivities and specificities of 85% and 86%, respectively [5], and with statistical significance [23] in the setting of chronic pancreatitis. In Stage 3, a PTI model was employed to detect a pancreatic cancer precursor [131]. Here, we address Stage 4 by reporting the *in vivo* feasibility of optical spectroscopy to detect malignant tissues.

3.2 Clinical optical spectroscopy measurements of *in vivo* human pancreatic tissues

3.2.1 Reflectance and Fluorescence Lifetime Spectrometer (RFLS)

A Reflectance and Fluorescence Lifetime Spectrometer (RFLS) [27,31] was employed to collect optical data from human pancreatic tissues *in vivo* (**Figure 3.1**).

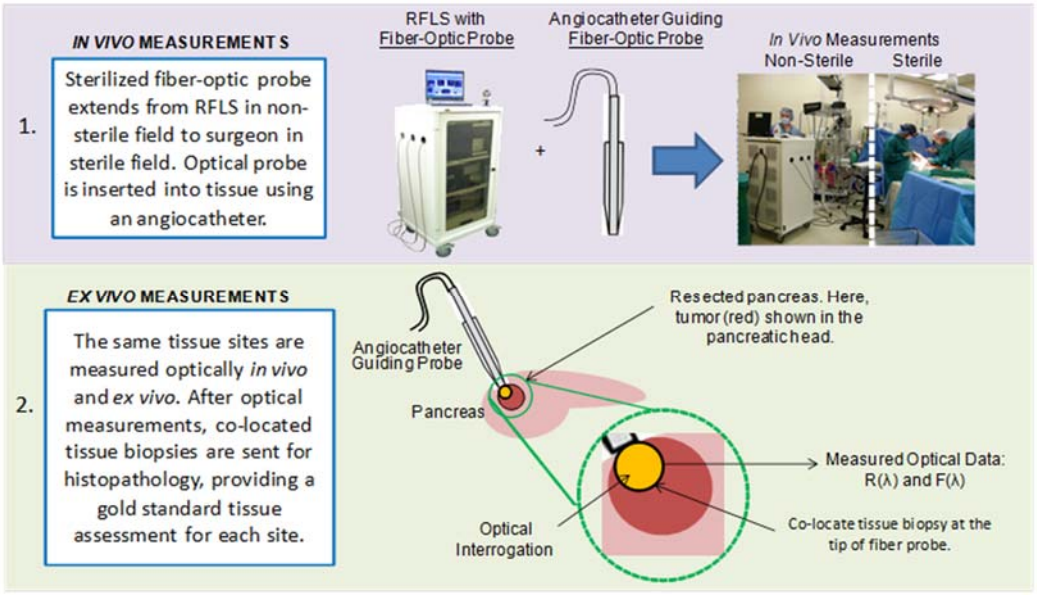

Figure 3.1. Pancreatic tissue optical measurement protocol, designed to mimic fine-needle aspiration (FNA) procedures by introducing the optical probe via a hollow angiocatheter. (1) In vivo: at this stage of surgery, tissue was still perfused with some blood and was near body temperature. The sterilized fiber-optic probe (6 m length) extended from the RFLS in the non-sterile field to the patient in the sterile field. At each selected site, the surgeon inserted a 14 gauge angiocatheter (B Braun Medical) ~1 cm into the tissue, removed the stylet from the angiocatheter, and inserted the fiber-optic probe. Data acquisition for each site was < 45 s, with each modality acquired in < 1 s. (2) In vivo and ex vivo measurements were acquired at the same tissue site by marking the site prior to resection. (2, right) Each optical measurement was estimated to interrogate ~1 mm3 of tissue. Repeatability was tested by collecting two successive optical measurements at each site, with up to two tissue sites measured per patient. Tissue sites were biopsied for histopathologic analysis.

The RFLS sequentially collected steady-state reflectance and fluorescence with a hand-held three-channel fiber-optic probe [31]. Measured spectral data were background subtracted and corrected for the spectral instrument response [5,23,31,101,130]. Reflectance measurements were acquired by delivering broadband white light from a CW tungsten halogen lamp (HL 2000FHSA, Ocean Optics) to tissue. An 850 nm short-pass filter (Semrock) protected human tissue from infrared light. Reflected photons were collected with the common detection fiber and detected by a spectrograph (MS 125, Oriel Instruments) coupled to an intensified charge-coupled device (ICCD 2063, Andor Technology).

Fluorescence measurements were acquired by delivering 355 nm pulsed laser excitation (PNV001525-140, JDS Uniphase) to the tissue. Laser energy delivered to the tissue was < 12 μJ. The fluorescence emission was collected with the common detection fiber and measured with the spectrograph-coupled ICCD.

3.2.2 *In vivo* and *ex vivo* data collection protocol

Optical measurements followed a study protocol approved by the University of Michigan (U-M) Institutional Review Board. Patients enrolled in the study provided written informed consent. Optical fiber probes were sterilized with an ethylene oxide protocol developed in accordance with U-M Hospital Central Sterile Supply. **Figure 3.1** outlines the optical measurement protocol for human pancreatic tissues. It is important to note that cancer patients undergoing surgical intervention (*e.g.*, all patients in this study) have a high pre-test likelihood of pancreatic disease. Our optical measurements of "normal" and "chronic pancreatitis" tissues were obtained from this biased patient population. Histological observations, including average diameter of cell nuclei, from our expect

pathologist confirmed that the "normal" and "chronic pancreatitis" tissues had morphological parameters consistent with an unbiased patient population. Thus, optical measurements from our biased patient population are hypothesized to be consistent with typical pancreatic tissues in patients without cancer.

In vivo and *ex vivo* optical measurements were collected from the same tissue sites (freshly-excised tissues within 30 minutes of resection [5,23,31]). Ideally, a fixed angiocatheter would mark the tissue site for *in vivo* and *ex vivo* measurements. Due to surgical complications, the angiocatheter remained in place for only 1 patient. For the other 5 patients, the point-of-entry was uniquely marked with surgical thread. The surgeon collected optical data *in vivo*. An expert pathologist oversaw *ex vivo* data collection and performed a tissue biopsy at each site immediately after optical measurements. Biopsy specimens were sent for analysis via histopathology.

3.2.3 In vivo optical data set

In total, 10 pancreatic tissue sites were measured from 6 patients with histopathological classification of pancreatic adenocarcinoma (5 sites) and normal (5 sites). Exclusion criteria were employed to remove tissue sites with excessive amounts of absorption (*e.g.*, $R_{550\ nm}/R_{650\ nm} < 0.1$) or low signal-to-noise ratio (*e.g.*, < 5). After exclusion, the *in vivo* data set included steady-state reflectance measurements from 8 (3 normal from 2 patients, 5 adenocarcinoma from 3 patients) tissue sites and steady-state fluorescence measurements from 4 (1 normal from 1 patient, 3 adenocarcinoma from 2 patients) tissue sites. Thus, steady-state reflectance measurements were analyzed quantitatively, as they constituted the largest usable data set and as previously reported results [5,23,31,101] showed that reflectance analysis alone can improve diagnosis of pancreatic malignancy.

3.3 Steady-state reflectance spectroscopy analysis

A reflectance spectral ratio classifier was developed to quickly characterize the measured tissue sites. In human pancreatic tissues, the ratiometric classifier $R_{470\ nm}/R_{650\ nm}$ was shown in prior work to vary with pancreatic disease [31].

Previously, for an *ex vivo* human pancreatic tissues data set, we reported a quantitative analysis algorithm that directly extracted optical tissue parameters [23,101]. The photon-tissue interaction (PTI) model that was fit to the optical spectra was obtained by employing a semi-empirical reflectance model [109] to scale the "canonical normal" reflectance (average of all measured normal reflectance spectra) to a model for each unknown reflectance spectrum. Here, we employed a canonical normal obtained from our *in vivo* data set (2 of 3 normal sites with comparable hemoglobin content) to model measured *in vivo* spectra from 450 - 530 nm [23,101]. This *in vivo* PTI model extended the maximum hemoglobin concentration from 25 [101] to 60 μM. Model fits to data with more than 15% error between 450 – 530 nm were excluded, including one adenocarcinoma and one normal site.

3.4 Feasibility of optical spectroscopy on human pancreatic tissues *in vivo*

For the first time, to our knowledge, tissue optical reflectance and fluorescence measurements were recorded from human pancreatic tissues *in vivo*. **Figure 3.2** shows reflectance and fluorescence spectra from a tissue site measured *in vivo* and *ex vivo* on the same patient. Measurements were recorded rapidly (< 1 s per modality) and were remarkably consistent, especially considering the anticipated large variability in tissue blood content *in vivo*.

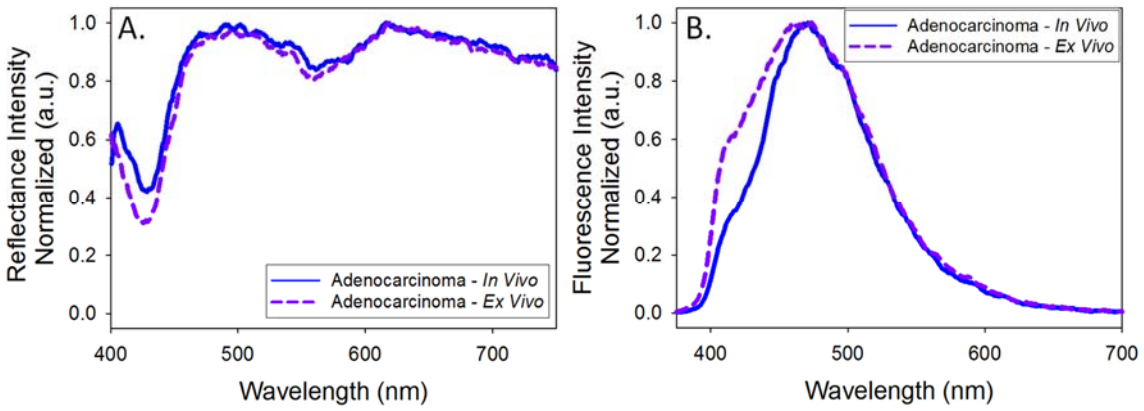

Figure 3.2. Optical measurements from a tissue site in vivo and ex vivo for (A) steady-state reflectance and (B) steady-state fluorescence. Measurements of the same tissue site contained similar features, attributed to similar tissue composition and morphology [23], and differed only slightly between 400-475 nm due to the anticipated blood content variations. The site was histopathologically confirmed to be adenocarcinoma.

3.5 Optical reflectance differences between normal and adenocarcinoma tissues *in vivo*

Figure 3.3(A) shows that for human tissues measured *in vivo*, there are significant differences between the optical reflectance spectra of normal pancreas and adenocarcinoma, notably in the shaded wavelength range 455-525 nm. This result is consistent with *ex vivo* studies [5,23,31,101,130] and is attributed to differences in scattering between tissue types [23]. Indeed, *in vivo* reflectance measurements on human pancreatic cancer xenografts grown in mice [31] (**Figure 3.3(B)**) clearly show the pronounced reflectance peak in this region.

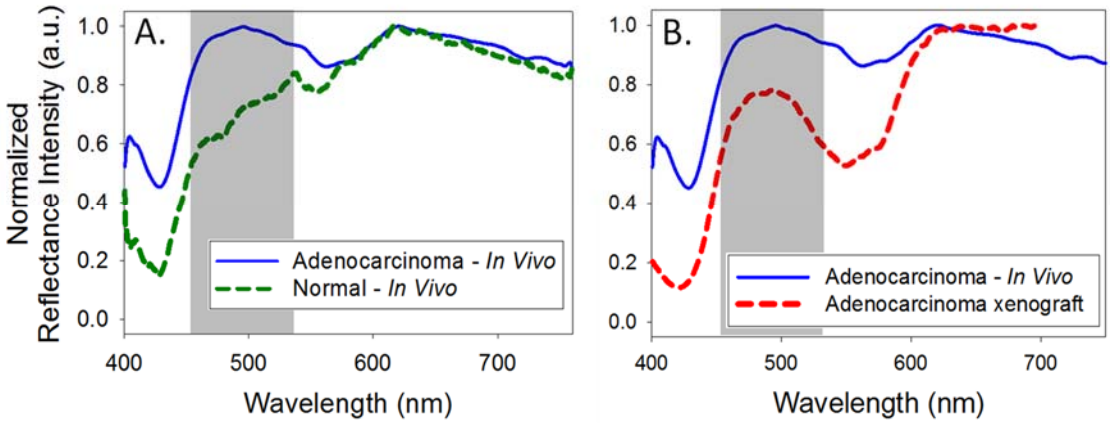

Figure 3.3. Representative *in vivo* reflectance measurements from human pancreatic adenocarcinoma (blue solid: A, B), (A) normal human tissue (green dashed), and (B) human pancreatic cancer tumor xenograft in a non-obese diabetic/severe combined immunodeficiency (NOD/SCID) mouse (red dashed) [31]. In the diagnostically important wavelength range between 455-525 nm (shaded), adenocarcinoma tissues have greater relative reflectance than normal tissues, consistent with extensive *ex vivo* studies [5,23,31,101,130].

3.6 Quantitative reflectance analysis with spectral ratios classifier and PTI model

Figure 3.4 summarizes the results of quantitative analyses applied to *in vivo* human pancreatic tissue reflectance data. *In vivo* reflectance data was consistent with *ex vivo* reflectance data (both for the *ex vivo* results obtained here and for the *ex vivo* results obtained on an extensive data set [5,23,31,101,130]) and was able to distinguish between normal human pancreas and pancreatic adenocarcinoma.

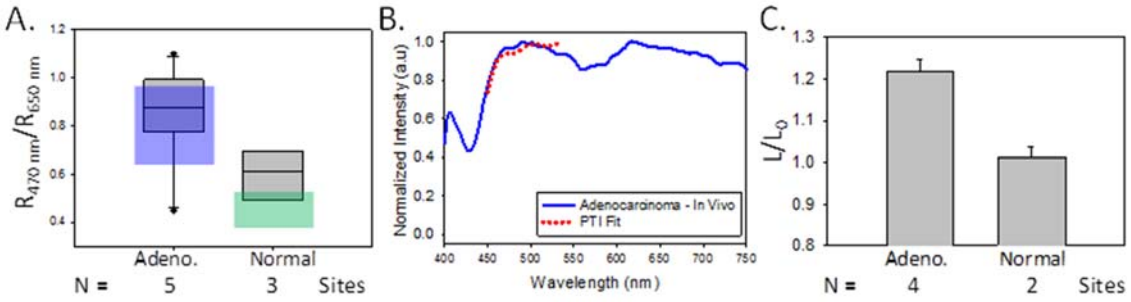

Figure 3.4. Quantitative analysis of *in vivo* reflectance data is consistent with *ex vivo* results and can distinguish between normal human pancreas and pancreatic adenocarcinoma. (A) The $R_{470\ nm}/R_{650\ nm}$ ratio for *in vivo* data (gray box plot) analyzed the pronounced spectral feature at 470 nm which clearly distinguished adenocarcinoma from normal tissues. The blue and green overlays show the analysis for an extensive *ex vivo* data set [23], which shows the same trend as that observed *in vivo*. Minor differences between *ex vivo* and *in vivo* results were attributed to the limited experimental control of local blood content during *in vivo* measurements. (B) PTI model best fit (red, dotted) to the *in vivo* adenocarcinoma data in **Figure 3.2** (blue) (4% fit error between 450 – 530 nm). (C) A PTI-extracted morphological parameter (L/L_0, related to changes in cellular nuclear size and shape) from *in vivo* measurements clearly distinguished adenocarcinoma from normal pancreas, consistent with results from an extensive *ex vivo* data set [23]. *In vivo* measurements from adenocarcinoma tissues modeled with an *ex vivo* "canonical normal" (from [23]) showed comparable results to employing an *in vivo* "canonical normal. Error bars represent standard error.

3.7 Discussion and conclusions

Pancreatic adenocarcinoma has a five-year survival rate of less than 6%, a fact that has not changed in nearly forty years [115]. This exceptionally low survival rate is attributed to the lack of accurate detection methods, which limits diagnosis to advanced stages of disease development [116,117].

Here, we presented an *in vivo* pilot study to assess the feasibility of optical spectroscopy to improve the clinical detection of pancreatic adenocarcinoma. This *in vivo* feasibility study was performed with limited experimental control over blood content using a

protocol that mimicked fine-needle aspiration, the diagnostic procedure-of-choice for tissue acquisition in suspect pancreatic cancer. Our promising results demonstrate the robustness of both the data collection and the analysis methods employed to characterize measured optical data in the presence of varying blood.

We note that our optical measurements of "normal" tissue sites are biased by the high pre-test likelihood of disease in the enrolled patients. Because these "normal" tissue sites were histologically consistent with normal human pancreas, we hypothesize that measurements from both normal tissues would be qualitatively and quantitatively similar. Future work will characterize morphological tissue parameters without employing a "canonical normal," removing dependence on *a priori* data.

From optical measurements acquired during open surgery on 6 patients, we verified the ability to collect spectrally-resolved reflectance and fluorescence rapidly (< 45 s) and repeatedly *in vivo*. From site-matched data, we examined the consistency between *in vivo* and *ex vivo* measurements and found both qualitative and quantitative (via known ratiometric [5,31] and photon-tissue interaction [23,101,130] models) agreement between the two. Further, quantified differences between adenocarcinoma and normal tissues measured *in vivo* were consistent with differences established previously using an extensive *ex vivo* dataset [5,23,31,101,130].

Overall, these results suggest that optical spectroscopy is a promising method for the improved diagnosis of pancreatic cancer *in vivo*.

Chapter 4.
Improved detection of pancreatic disease with time-resolved fluorescence spectroscopy

4.1 Introduction

Pancreatic adenocarcinoma is not reliably diagnosed in its earliest stages, resulting in a dismal five-year survival rate of only 6% [132]. The pancreatic cancer diagnostic procedure-of-choice is endoscopic ultrasound-guided fine-needle aspiration (EUS-FNA) [117,133]. In a recent clinical study, the sensitivity of EUS-FNA for detecting pancreatic adenocarcinoma in the setting of chronic pancreatitis (inflammation) was found to be only 54% [117]. A recent meta-analysis of 28 clinical studies concluded that it was not advisable to use EUS-FNA to diagnose pancreatic adenocarcinoma because malignancy "cannot be ruled out with adequate reliability [133]." Therefore, there is a significant clinical need for a method that can reliably detect early-stage pancreatic cancer in the setting of chronic pancreatitis.

Optical spectroscopy has shown potential to improve cancer diagnostics in many types of human tissues, including the breast [7], colon [94], cervix [119], esophagus [96], and lymph nodes [8, 9]. Our own studies have demonstrated the potential of steady-state reflectance and fluorescence spectroscopies for optical diagnostics in the pancreas [5,23,101]. Current state-of-care in detecting pancreatic disease would improve if technology could distinguish pancreatic disease in the following five tissue groupings: (1) malignant (adenocarcinoma) from benign (normal and chronic pancreatitis) tissues, (2) adenocarcinoma from chronic pancreatitis tissues, (3) diseased (adenocarcinoma and

chronic pancreatitis) from normal tissues, (4) adenocarcinoma from normal tissues, and (5) chronic pancreatitis from normal tissues.

Compared to the steady-state optical spectroscopy results, time-resolved fluorescence is sensitive to fluorophore microenvironment, including binding status, pH, and temperature, while generally insensitive to hemoglobin absorption [1]. Indeed, time-resolved fluorescence spectroscopy has shown potential to assist with disease diagnostics in other organs (including the brain [134,135], colon [14], heart [136], and skin [137]). Here, we employ only time-resolved fluorescence data to classify pancreatic disease with an *ex vivo* data set. This *ex vivo* data set is further employed as training data in a classification algorithm that classifies the first ever *in vivo* time-resolved decays measured from human patients.

4.2 Materials and Methods

4.2.1 Clinically-compatible time-resolved fluorescence spectrometer

Time-resolved decays were acquired from human pancreatic tissues with a clinically-compatible prototype Fluorescence Lifetime Spectrometer (FLS) [5,31]. The FLS (**Figure 4.1**) employed a fiber-optic probe (600 μm diameter) to deliver 355 nm laser light (PNV001525-140, JDS Uniphase; 1 kHz, ~16 μJ/pulse, 500-ps pulse duration) to the tissue. A second channel of the fiber optic probe (600 μm diameter, 660 μm center-to-center spacing) collected emitted fluorescent photons. A long-pass filter rejected excitation and emission light < 500 nm which prevented collagen signal (peak ~420 nm) from dominating measured fluorescence. Emission fluorescence > 500 nm was detected by an avalanche photodiode (C5658, Hamamatsu) and digitized with an oscilloscope (TDS 784A, Tektronix).

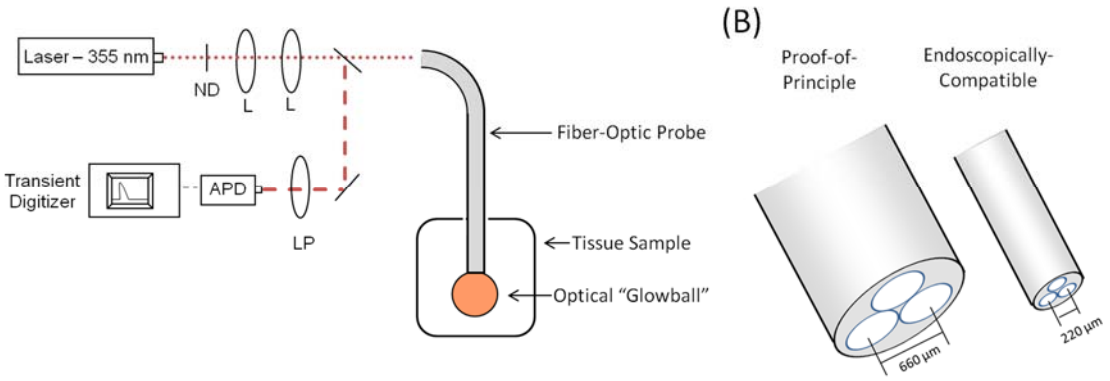

Figure 4.1. (A) A Fluorescnece Lifetime Spectrometer collected fluorescence decays from pancreatic tissues with a free-space fiber-optic probe. (B) *Ex vivo* data set and *in vivo* pilot study measurements were measured with a large fiber-optic probe for proof-of-principle studies. To demonstrate compatibility with future endoscopic procedures, optical fiber diameter was reduced by 1/3rd. The endoscopically-compatible fiber-optic probe was emlpoyed during a *ex vivo* feasibility study of 1 normal patient site. The third channel was not employed in this study, but was used in previous studies for reflectance spectroscopy measurements. Abbreviations - ND: neutral density filter, L: collimating lenses, LP: long-pass filter at 500 nm, APD: avalanche photodiode.

4.2.2 Optical Data Set

Study protocols were approved by the University of Michigan Institutional Review Board, and written informed patient consent was obtained before each measurement. Established protocols were followed for *ex vivo* [31] and *in vivo* [138] measurements. Time-resolved fluorescence decays were acquired from freshly-excised human pancreatic tissues *ex vivo* from 10 patients within 30 minutes of removal during pancreatic surgery and *in vivo* from 5 patients during open surgery with a sterilized fiber-optic probe. *In vivo* measurements were collected from embedded tissue sites by guiding the fiber-optic probe through an angiocatheter to mimic future fine-needle aspiration procedures [138]. For *ex vivo* measurements, up to 10 unique sites were measured per patient [31]. For *in vivo* measurements, up to 2 unique sites were measured per patient [138]. At each site, two

time-resolved fluorescence decays were collected sequentially. At one *ex vivo* site, only one measurement was collected. An expert pathologist specializing in gastrointestinal research supervised all measurements and collected site-matched biopsies for "gold standard" histological analysis from each measured site. These biopsies were subsequently stained, sectioned, and analyzed to determine tissue disease state. Prior to applying exclusion criteria, *ex vivo* data set comprised measurements from 29 normal (N), 16 chronic pancreatitis (CP), and 27 adenocarcinoma (A) sites and *in vivo* data set comprised measurements from 3 N and 5 A sites.

4.2.3 Data Pre-Processing and Exclusion Criteria

Prior to analysis, baseline offset was subtracted from fluorescence decays. Fluorescence decays with peak intensity prior to normalization of < 0.03 were excluded from the analyzable data set. Data sets after applying exclusion criteria are shown in **Table 4.1**. From the *ex vivo* data set, 3 N, 1 CP, and 1 A site were excluded. From the *in vivo* data set, 1 N site was excluded.

Table 4.1. Analyzable *ex* and *in vivo* data set.

	Ex Vivo		***In Vivo***	
	Patients	Sites	Patients	Sites
Normal (N)	6	26	2	2
Chronic Pancreatitis (CP)	4	16	-	-
Adenocarcinoma (A)	4	26	3	5
Total	10*	68	5	7

*Not a sum of patients, some patients had multiple tissue types measured.

4.2.4 Time-resolved fluorescence analysis methods

4.2.4.1 Instrument response function

A laser instrument response function (IRF) was measured for each patient as scattering from a solution of silica microspheres in deionized water. Fitting algorithms deconvolved the instrument response from measured fluorescence decay to extract fluorescence lifetime parameters. Employed fitting algorithms included a bi-exponential decay model [24] and the Laguerre expansion method [56].

4.2.4.2 Bi-exponential decay model

Time-resolved fluorescence decay curves were fit to a bi-exponential decay model [24], computed as $F(t) = a_1 \exp(-t/\tau_1) + a_2 \exp(-t/\tau_2)$. τ_i and a_i represent the extracted fluorescence lifetime and raw intensity contribution of fluorophore i, respectively. A_i were calculated as the percent contribution of τ_i.

4.2.4.3 Laguerre expansion method

A Laguerre expansion method modeled decay curves as a linear combination of Laguerre basis functions [56], a set of orthonormal functions that require no *a priori* assumptions about the behavior of the fluorescence decay prior to analysis [139]. Fluorescence decays were modeled as $F_{model}(t) = T\sum_{i=0}^{L-1}\left(LEC_i^{\alpha}\right)\left(b_i^{\alpha}(t)\right)$. LEC_i are the Laguerre expansion coefficients, $b_i^{\alpha}(t)$ are the Laguerre basis functions, T denotes the sampling interval, L represents the number of Laguerre functions, and α relates to how fast Laguerre functions converge to zero. Typical values of α are < 1 [56,140].

Laguerre functions modeled measured fluorescence decays by varying α and L over pre-defined grids: α from 0.5 to 0.95 with 0.025 step size and L from 3.0 to 6.0 with 1.0 step

size. The values of LEC_i and α that minimized the percent error between measured and modeled data were extracted for each time-resolved fluorescence decay

.

4.3 Tissue classification protocol

4.3.1 Calculating average fluorescence decay parameters for each measured site

For each measured *ex* and *in vivo* site, up to two decay measurements were collected. Each measurement was fit with a bi-exponential decay model and the Laguerre expansion method. If both measurements remained after employing exclusion criteria, the extracted fitting parameters were averaged to yield one set of fitting parameters per site. If a site had one measurement excluded, the extracted fitting parameters from the non-excluded site were employed in the classification algorithm.

4.3.2 Statistical analysis tests independence of tissue types

SAS® software was employed to assess the patient-level statistical independence of extracted fitting parameters from measurements of adenocarcinoma, chronic pancreatitis, and normal tissues with a Pearson's chi-squared test. Significance was determined at $p < 0.05$.

4.3.3 Multinomial logistic analysis

For the *ex vivo* data set, classification was performed with a leave one patient out analysis. With 10 studied patients, 10 unique training and test sets were employed for classification. Training sets comprised extracted fluorescence decay parameters from 9 patients to train the classification algorithm, while test sets comprised extracted fluorescence decay parameters from the 10^{th} patient. The classification algorithm, developed in SAS® software, trained a multinomial logistic model that employed

Generalized Estimating Equations (GEE) [141]. The GEE analysis accounted for correlations from intrapatient measurements. Fit coefficients from the trained multinomial logistic model were employed to evaluate the test set. Classification algorithm outputs were the predictive probabilities of each site being normal [P(N)], chronic pancreatitis [P(CP)], or adenocarcinoma [P(A)]. The predictive probabilities summed to 1.

For *in vivo* data set classification, the training set comprised all 10 *ex vivo* patients and the test set comprised all 5 *in vivo* patients. As with *ex vivo* data alone, the classification algorithm outputs were P(N), P(CP), and P(A).

4.3.4 Receiver operating characteristic curves

Output predictive probabilities were employed to compute receiver operating characteristic (ROC) curves at the site-level. For each of the 5 tissue groupings, sensitivity and specificity were calculated by employing a varying threshold on P(A) or the sum of P(A) and P(CP).

4.3.5 Method to compute classification results

Output predictive probabilities from the classification algorithm were manually thresholded to calculate sensitivity, specificity, positive predictive value (PPV), and negative predictive value (NPV). Manual thresholds were set to best classify measurements from each of the 5 tissue groups. Alternative methods could be employed to calculate thresholds, including penalty tables or simplistic thresholds (*i.e.*, linear threshold at P(A) = 0.3). Manual thresholds were selected for optimizing diagnostic utility of each classification parameter.

4.4 Results

4.4.1 Average fluorescence decays distinguish normal, chronic pancreatitis, and adenocarcinoma tissues

Figure 4.2 shows averaged fluorescence decays from pancreatic tissues *ex* and *in vivo*. Relative to normal tissues, broader fluorescence decays were measured from chronic pancreatitis and adenocarcinoma tissues. This trend was observed for both *ex vivo* and *in vivo* data sets. Broader fluorescence decays indicated greater contribution of a long lifetime fluorophore, attributed to the relative long lifetime of extracellular collagen in human tissues [27].

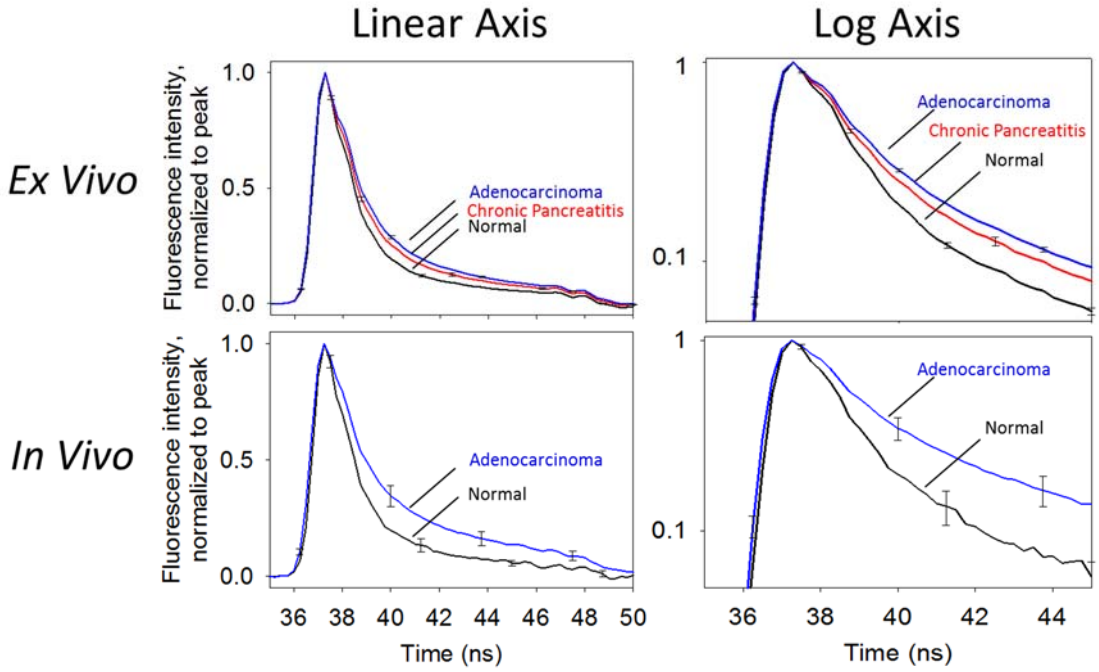

Figure 4.2. Time-resolved fluorescence decays distinguish normal, chronic pancreatitis, and adenocarcinoma tissues from (top row) *ex vivo* and normal from adenocarcinoma tissues from (bottom row) *in vivo* measurements. Fluorescence decays are shown with (left column) linear and (right column) logarithmic y-axis for improved comparison of data. Fluorescence decays were normalized to their peak, the peak from all decays of each tissue type aligned, and the aligned decays averaged for comparison. Fluorescence decays measured from adenocarcinoma and chronic pancreatitis tissues are broader than corresponding measurements of normal tissues. Error bars represent standard error.

4.4.2 Bi-exponential and Laguerre expansions fitting methods characterize differences between normal, chronic pancreatitis, and adenocarcinoma

Figure 4.3 shows extracted fitting parameters from bi-exponential decay and Laguerre expansion methods. *Ex vivo* fluorescence decays distinguish normal, chronic pancreatitis, and adenocarcinoma tissues. Extracted fluorescence decay parameters from an i*n vivo* pilot study confirm that normal and adenocarcinoma tissues quantitatively agree with *ex vivo* measurements. Extracted parameter A1 represents the relative contribution of the long lived endogenous fluorophore and LEC1 represents the relative contribution of the first Laguerre expansion function. A1 best distinguished normal from adenocarcinoma tissues, whereas LEC1 best distinguished normal from chronic pancreatitis tissues.

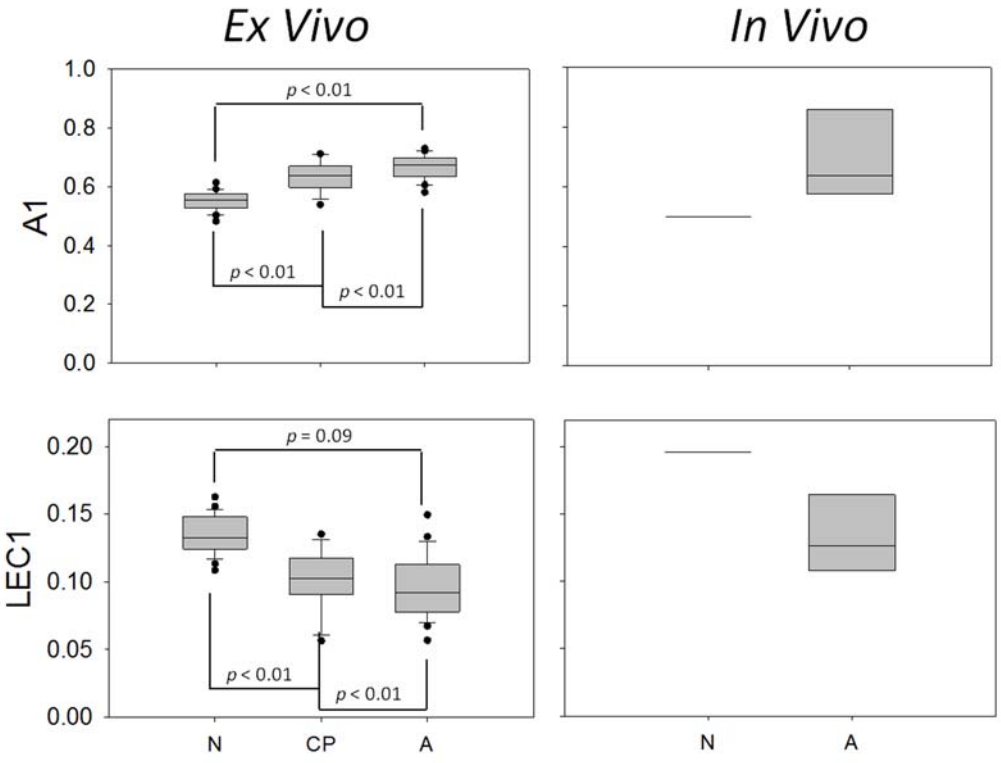

Figure 4.3. Fluorescence decay fitting parameters (top row) A1 and (bottom row) LEC1 distinguish measurements from normal, chronic pancreatitis, and adenocarcinoma tissues (left column) *ex vivo*. Extracted quantitative fitting

parameters from (right column) *in vivo* decays were consistent for normal and adenocarcinoma tissues. Relative differences in fitting parameters of normal, chronic pancreatitis, and adenocarcinoma tissues indicate decay broadening from normal to chronic pancreatitis to adenocarcinoma tissues (**Figure 4.2**). Statistical analysis was not performed on *in vivo* data due to limited measured sites. For *in vivo* data, the line from normal sites represents the mean extracted parameter from two sites.

4.4.3 Fluorescence decay analysis classifies normal, chronic pancreatitis, and adenocarcinoma both *ex* and *in vivo*

4.4.3.1 Receiver operating characteristic curves

Receiver operating characteristic curves classify malignant from benign tissues, adenocarcinoma from normal tissues, diseased (adenocarcinoma and chronic pancreatitis) from normal tissues, adenocarcinoma from chronic pancreatitis tissues, and chronic pancreatitis from normal tissues. Classification algorithm employed fitting parameters A1 and LEC1 to compute predictive probabilities. ROC curves were computed by varying diagnostic threshold as either P(A) or as the sum of P(A) and P(CP). The best classification results for each of the five tissue groupings are shown in **Figure 4.4**.

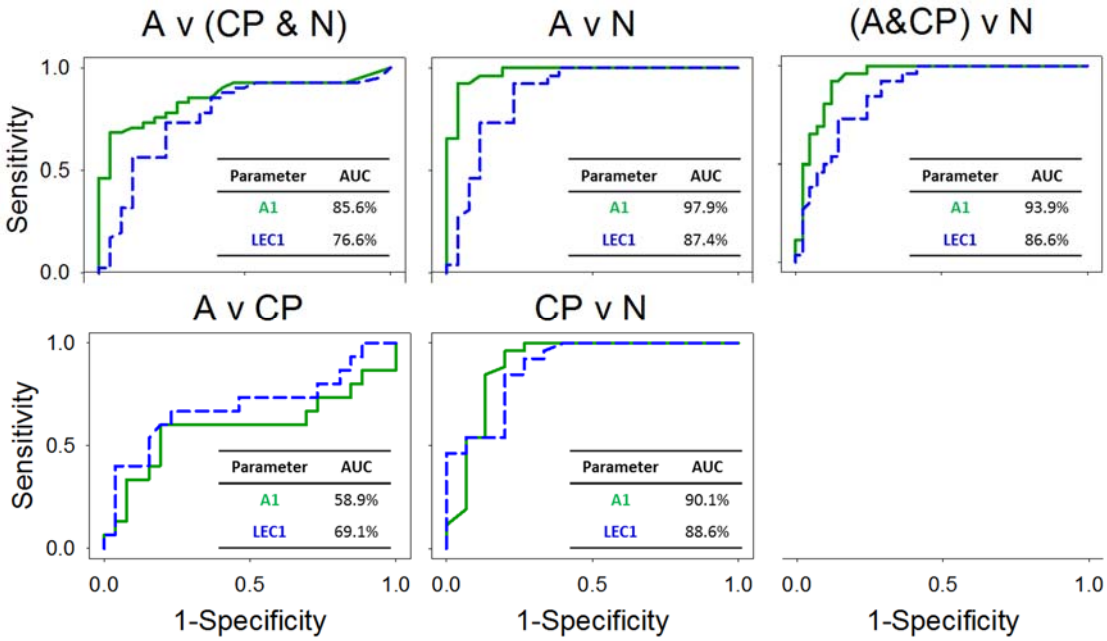

Figure 4.4. Receiver operator characteristic curves were computed for the 5 tissue groupings: (1, top left) A v (CP & N), (2, top middle) A v N, (3, top right) (A & CP) v N, (4, bottom left) A v CP, and (5, bottom middle) CP v N. (top row) To distinguish adenocarcinoma from either benign or normal tissues, receiver operating characteristic curves had highest area under the curve (AUC) when varying diagnostic threshold to the sum of P(A) and P(CP). (bottom row) To distinguish chronic pancreatitis from either adenocarcinoma or normal tissues, receiver operating characteristic curves had highest AUC when varying diagnostic threshold to P(A). Overall, A1 was the most useful diagnostic parameter to distinguish adenocarcinoma from benign tissues, whereas LEC1 helped improve classification of chronic pancreatitis tissues.

4.4.3.2 *Ex vivo* classification results: sensitivity, specificity, PPV, and NPV

Figure 4.5 shows ternary plots that were employed to distinguish normal from pancreatic disease. Ternary plots are two-dimensional scatter plots of three parameters. Here, ternary plots show the predictive probabilities P(N), P(CP), and P(A). Bi-exponential fitting parameter A1 best classified normal from adenocarcinoma tissues, whereas Laguerre expansion improves distinguishing chronic pancreatitis from normal tissues. These results indicate that two fitting methods can be sensitive to slight differences in the measured

fluorescence decays, highlighting the importance of employing more than one fitting method.

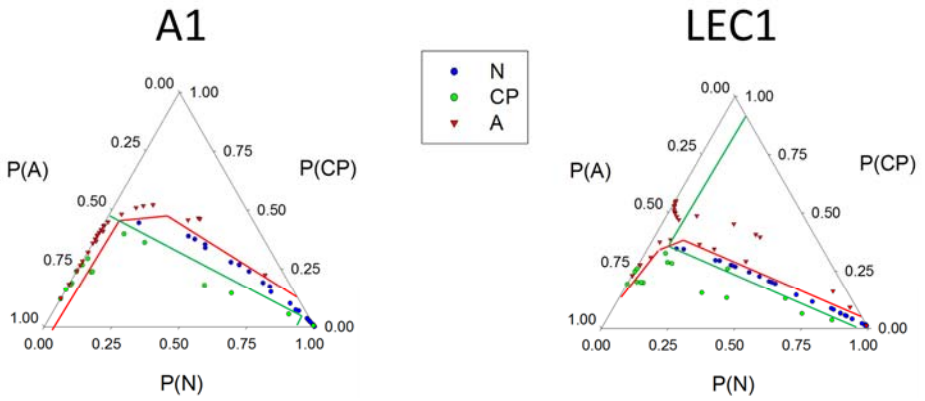

	A v (N&CP)	(A&CP) v N	A v CP	CP v N	A v N
Sens.	100%	78%	100%	93%	100%
Spec.	79%	100%	53%	100%	100%
PPV	83%	100%	79%	100%	100%
NPV	100%	62%	100%	96%	100%

	A v (N&CP)	(A&CP) v N	A v CP	CP v N	A v N
Sens.	89%	73%	96%	93%	96%
Spec.	97%	100%	80%	100%	100%
PPV	96%	100%	89%	100%	100%
NPV	93%	70%	92%	96%	96%

Figure 4.5. Two fluorescence decay fitting parameters, A1 and LEC1, classified adenocarcinoma, chronic pancreatitis, and normal tissues. A1, the percent contribution of the long lifetime component extracted with a bi-exponential decay model, best distinguished adenocarcinoma from benign tissues, whereas LEC1, the percent contribution of the first Laguerre expansion function, best distinguished adenocarcinoma from chronic pancreatitis tissues. Red lines show manual classification threshold to distinguish adenocarcinoma from benign tissues (for A v (N&CP), A v CP, and A v N). Green lines show manual classification threshold to distinguish chronic pancreatitis and diseased from normal tissues (for CP v N and (A&CP) v N).

4.4.3.3 *In vivo* data is accurately classified by *ex vivo* data set

Figure 4.6 shows ternary plots of predictive probabilities to distinguish normal from adenocarcinoma tissues *in vivo*. The classification algorithm was trained with an extensive *ex vivo* data set and applied to classify a limited *in vivo* data set measured from 5 patients. As demonstrated with *ex vivo* data, adenocarcinoma tissues are best

distinguished with bi-exponential fitting parameter A1. Measurements from additional sites are required to report any statistical or classification results with confidence.

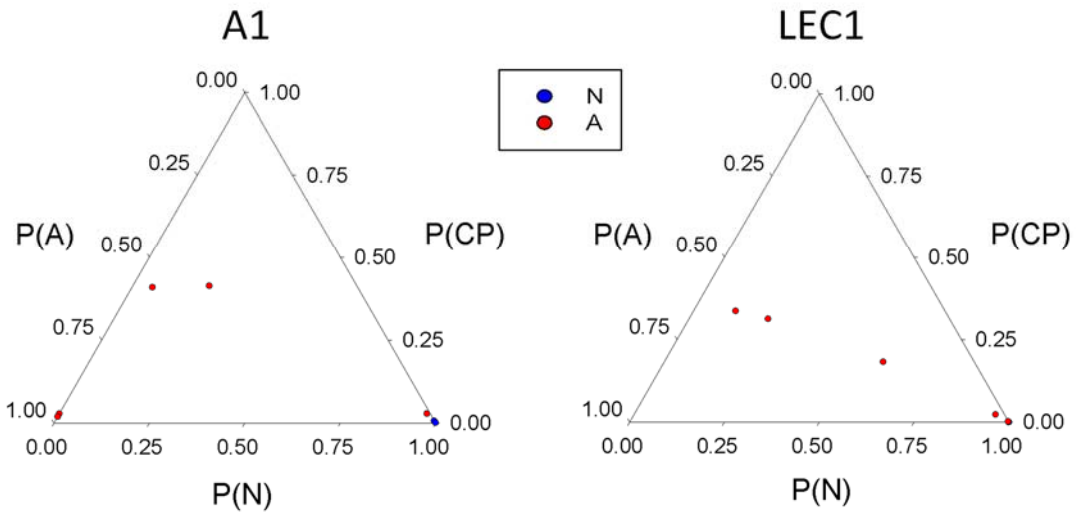

Figure 4.6. *In vivo* fluorescence decays accurately distinguish normal from adenocarcinoma tissues. An extensive *ex vivo* data set was employed to train the classification algorithm to distinguish the *in vivo* measurements. With measured sites from the pilot feasibility study (2 normal and 5 adenocarcinoma), time-resolved fluorescence distinguish both normal sites and 4/5 adenocarcinoma sites with A1 and 3/5 adenocarcinoma sites with LEC1.

4.4.4 Endoscopically-compatible probe measures fluorescence decay data consistent with proof-of-principle fiber-optic probe

An *ex vivo* feasibility study compared measured fluorescence decays with a larger, proof-of-principle probe to a 3x smaller, endoscopically compatible probe. Fluorescence decays were measured from one normal human site, shown in **Figure 4.7**. Good qualitative agreement was observed, confirming that diagnostically useful information is preserved during *in vivo* measurements. This result demonstrates the promise of time-resolved fluorescence instrumentation to detect adenocarcinoma tissues during endoscopic diagnostic procedures.

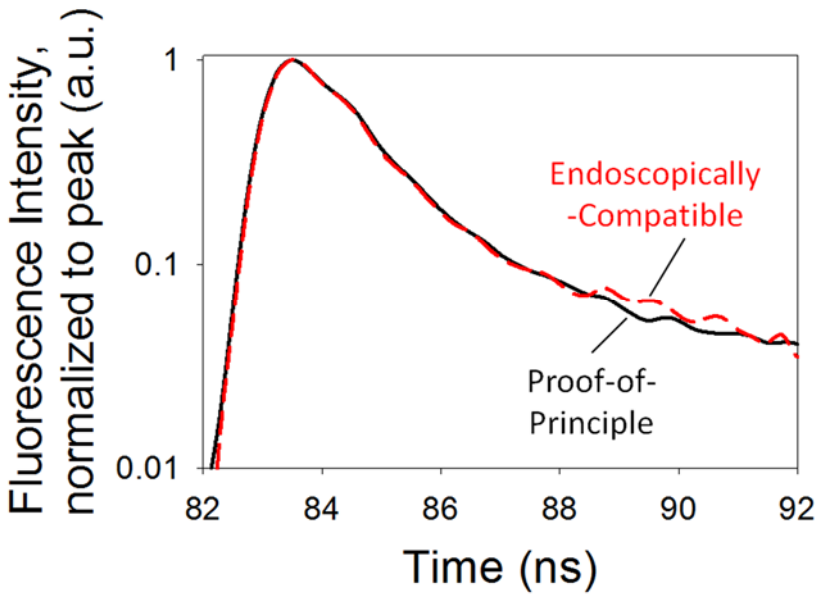

Figure 4.7. As part of a feasibility study, one *ex vivo* human pancreatic tissue normal site was measured with a proof-of-principle and an endoscopically-compatible fiber-optic probe. Results show good agreement between the two measurements, indicating that no fluorescence information is lost with an endoscopically-compatible fiber-optic probe.

4.5 Discussion and conclusions

Non-invasive, label-free, and quantitative time-resolved fluorescence data and corresponding analysis distinguished normal, chronic pancreatitis, and adenocarcinoma tissues. Compared to steady-state optical spectroscopy results, time-resolved data results are comparable to distinguish malignant from benign tissues and may be better to distinguishing normal from chronic pancreatitis.

Tissue classification was performed by accounting for intrapatient correlations. While rigorous, this classification algorithm could not account for inherent biases within the data set. For example, of the 15 chronic pancreatitis measurements in the *ex vivo* data set, 8 measurements were obtained from (1 of the 4) patients. 6 of these 8 measurements were consistent with adenocarcinoma, adding potential bias to the classification results.

Additional measurements could show if these chronic pancreatitis tissues are outliers or if more sensitive instrumentation is required for more accurate classification.

We note that all patients enrolled under this study were undergoing surgical intervention to treat suspected or confirmed pancreatic cancer. Thus, each patient had a high pre-test likelihood of pancreatic disease. Therefore, optical measurements of "normal" and "chronic pancreatitis" tissues were obtained from a patient who likely had pancreatic cancer. Histological observations, including average diameter of cell nuclei and relative concentration of collagen fibrils, from our expect pathologist confirmed that these "normal" and "chronic pancreatitis" tissues had morphological parameters consistent with tissues from patients without cancer. Thus, optical measurements from our biased patient population are hypothesized to be consistent with normal pancreatic tissues in healthy patients.

In this study, a single time-resolved decay was measured from all wavelengths > 500 nm. Therefore, local variations in broadband tissue absorber concentrations between measurements could impact the relative contributions from endogenous tissue fluorophores measured. For example, a site with excess hemoglobin would have an artificial lower fluorescence contribution from fluorophores that emit at wavelengths < ~550 nm, including collagen, due to hemoglobin absorption. To mitigate absorber-related artifacts, future studies will employ instrumentation that rapidly collects wavelength- and time-resolved data, such as wavelength-time matrices [24]. Employing such sensitive detectors for wavelength-resolved fluorescence decay collection may improve classification results.

Classification results were calculated by manually thresholding ROC curves. Therefore, threshold lines were drawn to optimize tissue classification from these *ex vivo* studies. With more measurements analyzed, tissue classification thresholds may need to be redrawn. Alternative methods could be employed to calculate unbiased thresholds, such as penalty tables or collection of additional *in vivo* fluorescence decays.

A parallel study employing only steady-state optical parameters (18 patients; 105 sites: 39 normal, 34 pancreatitis, 32 adenocarcinoma) reported a sensitivity, specificity, PPV, and NPV of 87.5%, 89.0%, 77.8%, and 94.2% for distinguishing malignant tissue (adenocarcinoma) from benign (normal and pancreatitis), 87.5%, 79.4%, 80.0%, and 87.1% for distinguishing adenocarcinoma from pancreatitis, and 70.6%, 82.1%, 77.4%, and 76.2% for distinguishing pancreatitis from normal tissue. Reported classification results (see **Figure 4.5**) employing only time-resolved fluorescence parameters show improved classification of adenocarcinoma and chronic pancreatitis tissues, including 100% sensitivity and 79% sensitivity to detect malignant from benign tissues. Therefore, time-resolved fitting parameters may improve tissue classification results for distinguishing adenocarcinoma from benign tissues, as well as distinguishing chronic pancreatitis from normal tissues. To compare the diagnostic utility of time-resolved and steady-state optical parameters, future studies will employ similar patient and site numbers.

In conclusion, we report the first-ever time-resolved fluorescence measurements from human pancreatic tissues *ex* and *in vivo.* Classification results indicate that time resolved fluorescence decays may improve tissue classification. Furthermore, we show that *in vivo*

fluorescence decays are a suitable method to detect adenocarcinoma during open surgery and compatible with endoscopic use.

Chapter 5.
Instrumentation to rapidly acquire fluorescence wavelength-time matrices of biological tissues

5.1 Introduction

The multidimensional data provided by fluorescence spectroscopy opens up the possibility of rapidly deriving quantitative diagnostic information from tissues in a minimally-invasive manner [142]. Steady-state and time-resolved fluorescence measurements have been performed with instrumentation designed for eventual translation to the clinic [2,27,143]. Steady-state fluorescence spectroscopy has been employed for cancer diagnostics in organs including the breast [7], cervix [119], esophagus [4,96], lung [144], and pancreas [5,31,101]. Time-resolved fluorescence spectroscopy has been employed for cancer diagnostics in organs including the brain [135,145], colon [6,14], esophagus [4], and lung [8]. Steady-state and time-resolved fluorescence measurements have been employed in ophthalmology for detection of conditions including macular degeneration, diabetic retinopathy, and retinal artery occlusion [146,147]. Time-resolved fluorescence measurements have also recently been used for the detection of cardiovascular disease [136] and type 2 diabetes [137].

Although steady-state fluorescence can reveal information about fluorophores in a biological tissue, the intensity of steady-state spectra are influenced by a variety of artifacts [143]. Time-resolved fluorescence measurements provide the fluorescence lifetime τ, which is the mean time spent by a fluorophore in its excited state [1]. The lifetime value is sensitive to the environment of the fluorophore, so it can vary with

changes in binding, pH, oxygen, and temperature. Importantly, lifetime measurements are not strongly dependent on intensity-based effects such as absorption, photobleaching, and changes in excitation intensity and collection efficiency [143,148]. Lifetime values for multiple fluorophores in a sample can be obtained from time-resolved fluorescence measurements, even if the steady-state spectra of the fluorophores overlap. Therefore, steady-state and time-resolved methods are both useful tools for characterization of biological tissue fluorescence.

Ideally one would maximize the amount of independent fluorescence information and the quality of the data (signal-to-noise ratio, for example) for every sample. However, clinical applications require consideration of measurement speed, portability, cost, and ease of use. The first *in vivo* endoscopic time-resolved fluorescence measurements on human patients were reported in 1998, using a portable, fiber-optic based system with a low repetition-rate laser and limited spectral resolution [6,14]. Since then, two strategies have been employed for combining spectral and temporal fluorescence data collection in a clinically compatible format. The first approach uses one laser excitation source, but two different detection platforms. The spectral and temporal data are collected in sequence, but could be obtained simultaneously. The second approach collects a full fluorescence wavelength-time matrix (WTM, **Figure 5.1**) by stepping an emission monochromator through a series of wavelengths, such that a fluorescence decay curve is produced sequentially at each of those wavelengths. Integrating the WTM over time yields a steady-state fluorescence spectrum. Integrating the WTM over wavelength yields a time-resolved fluorescence decay curve.

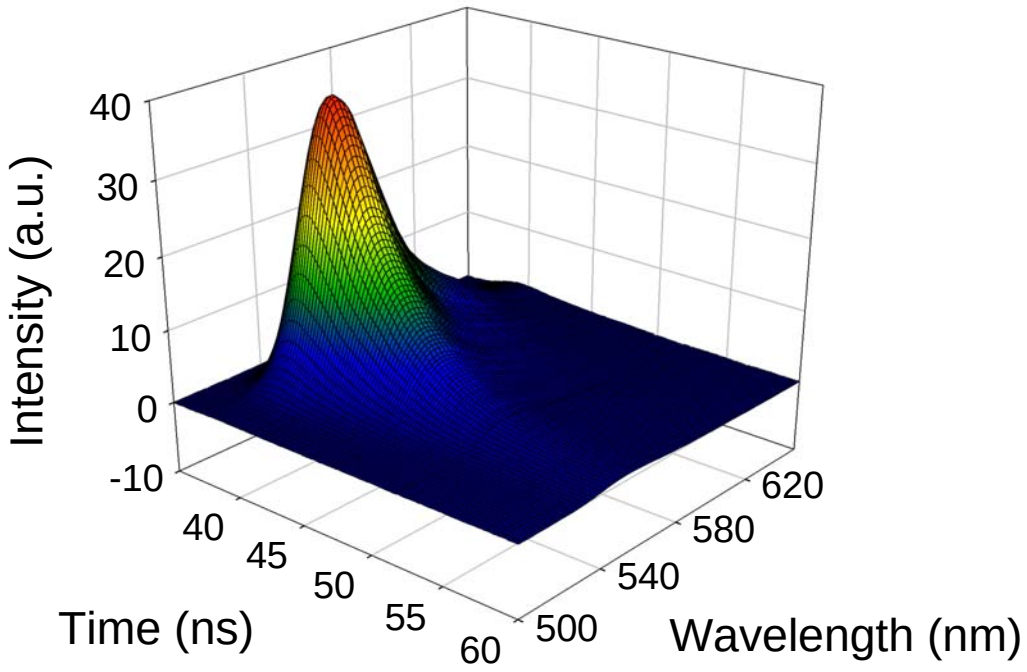

Figure 5.1. Fluorescence wavelength-time matrix (WTM) of 1 μM Rhodamine 6G in ethanol acquired with fiber-optic probes for light delivery and detection. The WTM contains both wavelength-resolved and time-resolved fluorescence data.

In this study, a specialized compact digitizer was employed to obtain WTMs from samples excited with a microchip laser, which had a repetition rate significantly higher than that used in similar spectroscopic devices [4,6,135,136]. Section 5.2 describes the technology developed for detecting fluorescence WTMs, the incorporation of this technology into a clinically compatible fiber-probe based instrument, and the experimental methods employed to assess the technology. Section 5.3 details system characterization using standard fluorophore solutions. Section 5.4 describes using the system to acquire fluorescence WTMs from tissue-simulating phantoms.

5.2 Instrumentation and experimental methods

5.2.1 Clinically-compatible instrumentation

The instrumentation (**Figure 5.2**) consisted of a 473 nm microchip laser (Lumanova, 20-030005, µFlare Blue, 3 kHz pulse repetition rate, ~2 ns pulse duration), a specialized transient digitizer (Fluorescence Innovations (FI), Inc., Bozeman, MT) for WTM measurement [149-151], a scanning monochromator (Optometrics, MC1-03), and a photo-multiplier tube (PMT) (Hamamatsu, H6780-20).

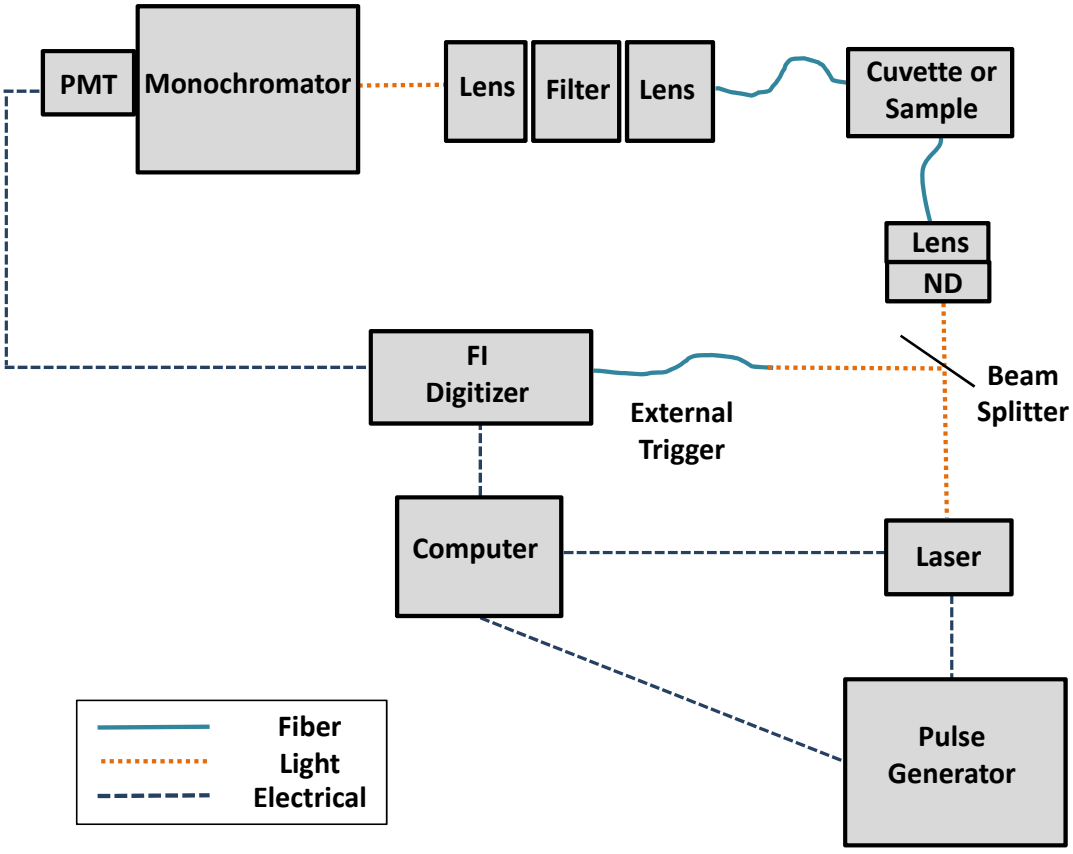

Figure 5.2. Schematic of the instrumentation developed for rapid acquisition of fluorescence WTMs, using fiber-optic probes for light delivery and detection (set-up 4, **Table 5.1**). WTMs were also obtained with three other set-ups (**Table 5.1**): (1) right-angle free-space geometry, in place of the fiber-probes, for light delivery and detection; (2) free-space light delivery and a fiber-probe for fluorescence detection; (3) a fiber-probe for light delivery and right-angle free-space geometry for detection.

The FI digitizer is an extremely compact, low power digitizer for direct waveform recording of the fluorescence decay curves. Its unique 10-bit, fast-in slow-out, analog-to-digital converter operates at 1 gigasample/second (GS/s) with a sampling depth of 128 ns. For most applications, 5X interleaving is applied to increase the effective sampling rate to 5 GS/s. This approach permits high-speed sampling without requiring equally high-speed conversion, which enables very reliable digitization. Event rates in excess of 25 kHz are possible. A graphical user interface enables user control over input parameters.

The digitizer can be employed to measure single-laser pulse collections. Additional laser pulses can be averaged to increase the signal-to-noise ratio. The time increase for measurements with additional laser pulses averaged is proportional to the increased number of laser pulses, with a small increase in pulses averaged not greatly affecting total collection time due to the rapid acquisition speed and high repetition rate laser employed. For samples with a lower concentration of fluorophores and weaker fluorescence signal, the PMT voltage can be increased prior to measurement to maximize the dynamic range of the digitizer. The detection system has a wavelength resolution of 0.01 nm and a temporal resolution of 200 ps.

The dimensions of the main system components are: 16 cm x 10.3 cm x 3.0 cm (digitizer), 9.5 cm x 4.0 cm x 7.0 cm (microchip laser), 15.2 cm x 6.4 cm x 6.4 cm (monochromator), 5.1 cm x 2.6 cm x 2.6 cm (PMT), 19.5 cm x 5 cm x 10 cm (laser power supply), and 16.5 cm x 10.5 cm x 4.5 cm (pulse generator). This small table-top footprint makes the system ideal for eventual translation to a clinical setting.

5.2.2 Optical configurations (fiber optics vs. free space)

For system characterization, four different system set-ups (**Table 5.1**) were employed to acquire WTMs from standard fluorophore solutions. Set-up 1 was a free-space right-angle geometry commonly used for cuvette-based measurements. Set-ups 2 and 3 were identical to set-up 1, except that set-up 2 used a fiber for detection and set-up 3 used a fiber for light delivery. Set-up 4 (**Figure 5.2**) was clinically compatible because it used fiber-optic probes (Fiberguide Industries, SFS600/660N, 600 μm core diameter) for light delivery and detection. For the reported studies, fiber-optic probes were inserted vertically 1 cm below the top surface of the fluorophore solution and 3 cm above the bottom of the cuvette with a 660 μm probe spacing.

Table 5.1. Set-ups employed to acquire fluorescence WTMs.

Set-up	Light delivery	Fluorescence detection
1	Direct illumination	Right-angle detection
2	Direct illumination	Fiber-optic probe
3	Fiber-optic probe	Right-angle detection
4	Fiber-optic probe	Fiber-optic probe

Focusing lenses (Thorlabs, LA4306-UV, LA4052-UV) and a 500 nm longpass filter (Semrock, FF01-488) were employed in set-ups 2 and 4 to couple and filter light from the fiber-optic probe to the monochromator. In set-up 4, fiber holders were attached to micrometer stages for controlled source-detector spacing.

5.2.3 Sample preparation

5.2.3.1 Standard fluorophore solutions

The system performance was tested (Section 5.3) by acquiring WTMs from solutions of three standard fluorophores: rhodamine 6G (Sigma, R4127), fluorescein (Sigma, 166308), and rose bengal (Sigma, 330000). Each fluorophore was made with a 1 μM concentration in ethanol. The solutions were thoroughly mixed in a cuvette prior to measurement. Signal-to-noise characterization of the system was performed with a stock solution (~1.7×10^7 beads/mL) of fluorescent beads (Invitrogen, A7303).

5.2.3.2 Tissue-simulating phantoms

Four tissue-simulating phantoms were made with different scattering coefficients. Each phantom originated from a ~1 mM solution of Rhodamine B (Sigma, R6626) in deionized water. For the first phantom, 4 mL of deionized water was combined with 4 μL of the original Rhodamine B solution. For the second phantom, 3.5 mL of deionized water was combined with 0.5 mL polystyrene microspheres (Duke Standards, 4009A, 1μm diameter) before adding 4 μL of the Rhodamine B solution. For the third phantom, 3 mL of deionized water was combined with 1 mL of polystyrene microspheres before adding 4 μL of the Rhodamine B solution. The fourth phantom was made by combining 2 mL of deionized water with 2 mL of the polystyrene microspheres before adding 4 μL of the Rhodamine B solution. Thus, the resulting concentration of Rhodamine B in each mixture was 1 μM. Each of these mixtures was then thoroughly combined with ~0.025 g of powder gelatin (Sigma, 097K0108) in a 50 mL conical tube. Then, each mixture was transferred to a 35 mm Petri dish and placed on an 80˚C hot plate for 20 minutes to dissolve the gelatin, stirring every 5 minutes. Each sample was removed from the hot

plate and returned to room temperature before refrigeration at 3°C overnight to solidify the sample. The resulting thickness of each phantom was approximately 4 mm.

An integrating sphere (RT-060-SF, Labsphere, North Sutton, NH) set-up was employed to measure the scattering coefficient for each phantom [152]. Briefly, a lamp with a Kohler illuminator (KI-120, Labsphere) was connected to a power supply (LPS-150-0660, Labsphere) to uniformly illuminate each phantom. Two configurations, one for reflectance and one for transmittance, were used; in both cases, the detected light traveled from the integrating sphere into a spectrometer (Ocean Optics, Dunedin, FL, HR2000+) via an optical fiber (Ocean Optics, P1000-2-VIS-NIR). The wavelength-resolved reflectance and transmittance of each phantom were input into an inverse adding-doubling (IAD) algorithm [153] to obtain the absorption and scattering coefficients. For the four phantoms, three of which contained microspheres, the IAD algorithm extracted negligible absorption coefficients and scattering coefficients of 10 cm^{-1}, 50 cm^{-1}, 108 cm^{-1}, and 222 cm^{-1}.

5.3 System characterization - reference fluorophores in fluid solution

5.3.1 Signal-to-noise as function of acquisition time

A stock solution of fluorescent beads was used to measure the signal-to-noise ratio of the system as a function of laser pulses averaged per waveform (**Figure 5.3**). Fluorescence decays were collected at 550 nm only and the standard deviation of fluorescence intensity from ten measurements was calculated by averaging standard deviations of intensity around the emission decay maximum (t = 36–38 ns). In **Figure 5.3 (a)**, the standard deviations (green curve) were measured with system set-up 4 (**Figure 5.2**) and were

obtained for acquisition times corresponding to 5, 125, 250, 375, 500, 750, 1000, 1250, and 1500 laser pulses averaged. The result was characteristic of Poisson noise (blue curve), which was defined as the square root of mean intensity divided by the square root of the number of laser pulses averaged, and multiplied by a factor of 0.045 to match the scale of the experimental results. The arrow in **Figure 5.3(a)** represents fluorescence acquisition with 125 laser pulses averaged. This fluorescence detection had a peak intensity of ~28 (a.u.) and a standard deviation of ~0.25 (a.u.), yielding a SNR greater than 100.

Figure 5.3(b) shows two measurements of time-resolved fluorescence: one obtained with 5 laser pulses (red curve), and the other obtained with 1250 pulses (purple curve). These two curves correspond to the circled collection points in **Figure 5.3(a)**. The two curves were similar in shape despite a 250-fold decrease in the number of laser pulses averaged.

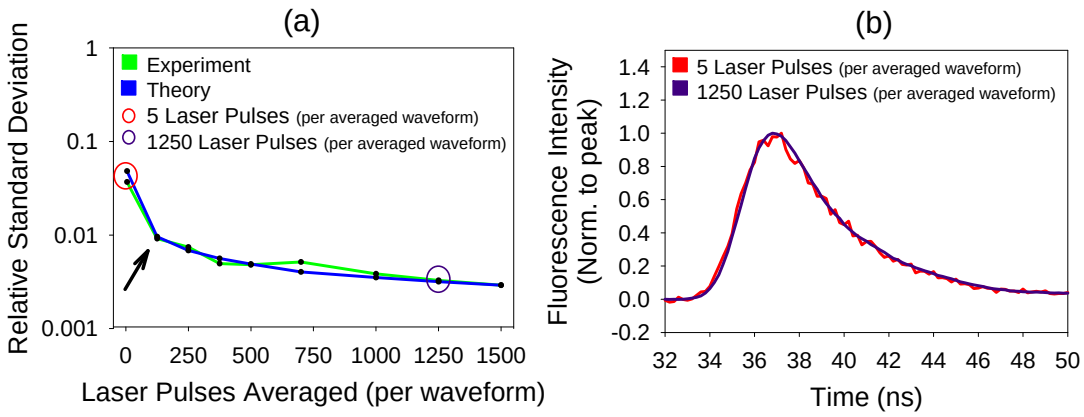

Figure 5.3. Signal-to-noise characterization of the system, performed on a stock solution of fluorescent beads: (a) standard deviation of measured fluorescence intensity (green curve), compared to prediction of Poisson theory (blue curve), as a function of acquisition time; (b) normalized fluorescence decay curves for 5 laser pulses averaged (red curve, corresponding to red circle in (a)) and 1250 laser pulses averaged (purple curve, corresponding to purple circle in (a)). The arrow in (a) denotes data acquisition with 125 laser pulses averaged; the standard deviation of the relative peak intensity at this point is ~0.25 (a.u.) with a peak signal intensity of ~28 (a.u.), yielding a SNR greater than 100.

5.3.2 Wavelength-resolved fluorescence

WTMs were acquired from the standard fluorophore solutions from 500 to 650 nm in steps of 2 nm, using 1250 laser pulses for excitation per wavelength. Time-resolved fluorescence was acquired from 0 to 127.8 ns in steps of 0.2 ns. The PMT setting was varied to keep detected signal within the operating range of the digitizer. Prior to data acquisition, the emission intensity of each sample was monitored for one minute to verify that no photobleaching occurred.

Figure 5.4 shows the time-integrated fluorescence spectrum of each standard fluorophore solution. For each fluorophore, three measurements with the fiber-based set-up (set-up 4, **Figure 5.2**) were averaged to obtain the spectra shown in **Figure 5.4**. The error bars (standard deviation) were similar in size for all four of the system set-ups (data not

shown). The collection time for each WTM was 82 seconds. The wavelength range measured was 500 to 650 nm with a 2 nm step size. For each wavelength, 1250 laser pulses were averaged to produce the time-resolved decay. These data were in good qualitative agreement (peak intensity wavelength agreed within 2 nm) with those reported in the literature [154].

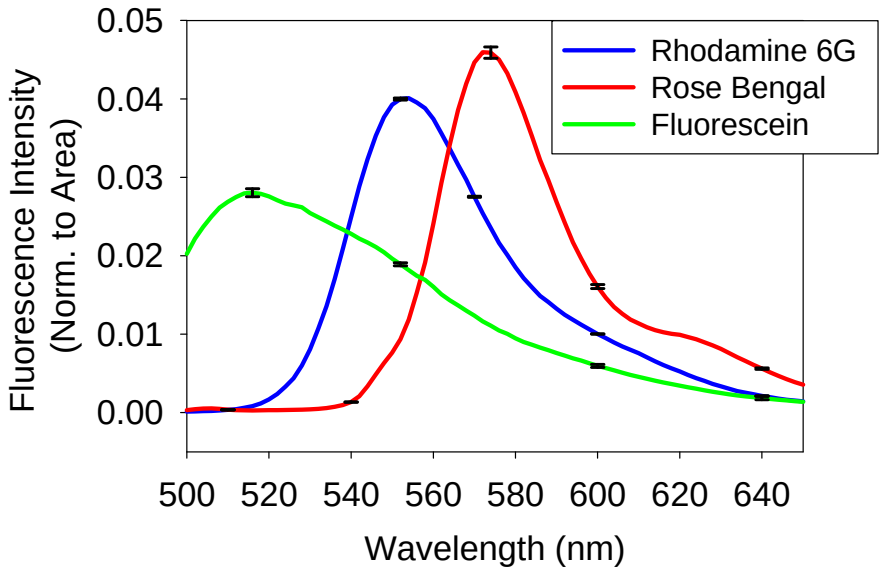

Figure 5.4. Fluorescence spectra of rhodamine 6G (blue curve), rose bengal (red curve), and fluorescein (green curve), measured with the fiber-based system set-up 4 and normalized to the area under the curve. Each curve is the average of three measurements; the error bars represent the standard deviation.

5.3.3 Time-resolved fluorescence and extraction of fluorescence lifetimes

Figure 5.5 shows time-resolved fluorescence decay curves obtained with the four system set-ups for rhodamine 6G (**Figure 5.5(a)**), rose bengal (**Figure 5.5(b)**), and fluorescein (**Figure 5.5(c)**). Each plot represents the average of the time-resolved fluorescence decays acquired for four set-ups (**Figure 5.5**) and multiple emission wavelengths. For each of these three plots, time-resolved measurements at the peak emission wavelength as

well as wavelengths corresponding to 0.6x peak intensity were averaged. Time-resolved fluorescence was obtained at three different emission wavelengths for rhodamine 6G and rose bengal. Time-resolved fluorescence from fluorescein was obtained at only two different emission wavelengths because the emission peak of fluorescein was near the first collection wavelength. The time-resolved fluorescence decays for each set-up were shifted to a common peak value for comparison, because integrating fiber-optic probes into the system set-ups changed the travel time slightly for delivered laser pulses and detected fluorescence. The error bars plot the standard deviation for each fluorophore, indicating that the measured time-resolved decays are consistent across collection wavelengths and system set-up geometries.

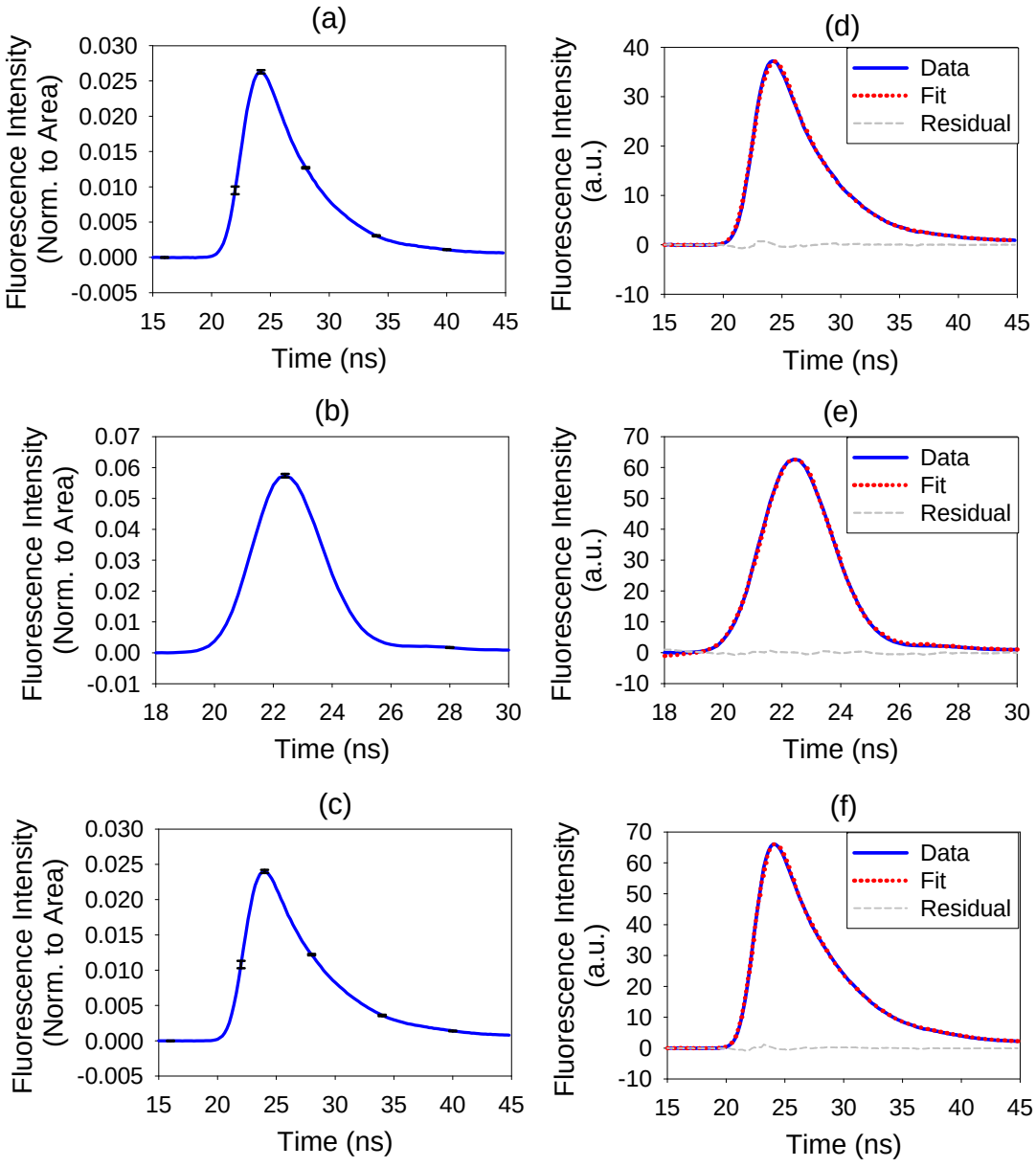

Figure 5.5. Time-resolved fluorescence decay curves measured on solutions of rhodamine 6G ((a), (d)), rose bengal ((b), (e)), and fluorescein ((c), (f)). Panel (a) plots 36 averaged rhodamine 6G fluorescence decays, panel (b) plots 36 averaged rose bengal fluorescence decays, and panel (c) plots 24 averaged fluorescein fluorescence decays (four system set-ups per fluorophore, three emission wavelengths for rhodamine 6G and rose bengal, two emission wavelengths for fluorescein). The error bars represent standard deviation. In panels (d), (e), and (f), one representative decay curve for each fluorophore measured with set-up 4 was fit to a single exponential decay.

Figure 5.5 also shows fits of representative time-resolved fluorescence curves measured with set-up 4 from rhodamine 6G (**Figure 5.5(d)**), rose bengal (**Figure 5.5(e)**), and fluorescein (**Figure 5(f)**) to a single-exponential decay $e^{-t/\tau}$, where τ is the mean fluorophore lifetime. An iterative least-squares fitting algorithm was employed to obtain these fits and extract the corresponding lifetime values [150]. In order to perform the fitting procedure, the instrument response function (IRF) was also acquired for each detection setting. The IRF was measured from a sample of deionized water in a cuvette, using neutral density filters to reduce the transmitted light energy to the sample. All data was fit using an IRF taken within 1 nm of the excitation laser wavelength (473 nm), selected because it is independent of the wavelength of the fit data and repeatable across experiments. The residuals are presented to show the quality of each fit.

Lifetime analysis was performed on the four set-ups at the peak fluorescence wavelength from each fluorophore, as presented in **Table 5.2** All data was fit as a single exponential decay with Fluorescence Analysis Fitting Software (Fluorescence Innovations (FI), Inc., Bozeman, MT). The extracted lifetimes were in good agreement with previously reported values and this agreement was consistent for each set-up. For each system set-up, three measurements were collected for each fluorophore and independently fit. The reported lifetime is the average of the three measurements plus or minus the standard deviation.

We note that the small discrepancies between lifetimes extracted for the four set-ups, as well as between the measured and literature values, could be due to differences in the way that the IRF was acquired, external factors such as temperature and pH, or impurities in the fluorophore solutions. For the measurements reported here, each fluorophore was

used directly from the manufacturer without further purification, and temperature and pH conditions were not monitored.

Table 5.2. Lifetime values obtained from standard fluorophore solutions.

Emission Wavelength (nm)	Fluorophore	Measured [a]				Literature
		Set-up 1	**Set-up 2**	**Set-up 3**	**Set-up 4**	
		Lifetime (ns)	Lifetime (ns)	Lifetime (ns)	Lifetime (ns)	Lifetime (ns)
550	Rhodamine 6G	3.977 ± 0.001	3.828 ± 0.004	3.971± 0.004	3.910 ± 0.001	3.99 ± 0.01[155]
514	Fluorescein	4.449 ± 0.004	4.603 ± 0.007	4.534± 0.002	4.620 ± 0.004	4.25± 0.01[155]
572	Rose Bengal	0.668 ± 0.014	0.676 ± 0.006	0.648 ± 0.003	0.711 ± 0.001	0.850 ± 0.030 [1]

[a]For each system set-up, three measurements were independently fit. The reported lifetimes are average plus or minus the standard deviation of these three fits.

5.4 Tissue-simulating phantom study

System set-up 4 (**Figure 5.2**) was employed to acquire WTMs from four tissue-simulating phantoms with different scattering coefficients in a range relevant to biological tissue. The measured scattering coefficients of the tissue-simulating phantoms were 10 cm^{-1}, 50 cm^{-1}, 108 cm^{-1}, and 222 cm^{-1}. A 0.66 mm fiber-probe source-detector separation was used during WTM collection for each phantom. Additional measurements with fiber-probe source-detector separations of 1.66 mm, 2.66 mm, 3.66 mm, and 4.66 mm were collected for the tissue-simulating phantoms with a scattering coefficient of 108 cm^{-1} and 222 cm^{-1}. Data was acquired from 500-700 nm (in 5 nm steps) with 1250 laser pulses averaged per wavelength. For tissue simulating phantoms with higher scattering coefficients, the PMT high-voltage was decreased for WTM measurement. The data

acquisition time for each tissue-simulating phantom was 49 seconds. This time can be substantially reduced with straightforward modifications, by decreasing the number of laser pulses averaged, or increasing the step size.

Figure 5.6(a) shows steady-state fluorescence spectra for each phantom, averaged over three sites and normalized to the area under the curve. Each of these spectra is a combination of the fluorescence spectra of gelatin (dark red curve) and Rhodamine B (dark green curve). The spectra of the four phantoms are very similar, with some small variations around 515 nm and 575 nm, where the standard deviations (error bars) are also higher. These variations may be the result of a variable gelatin fluorescence signal in the phantoms. **Figure 5.6(b)** plots time-resolved fluorescence decay curves obtained from averaging measurements at peak intensity at the three sites on each phantom. The small standard deviations (error bars) show that the decays at all three sites are similar.

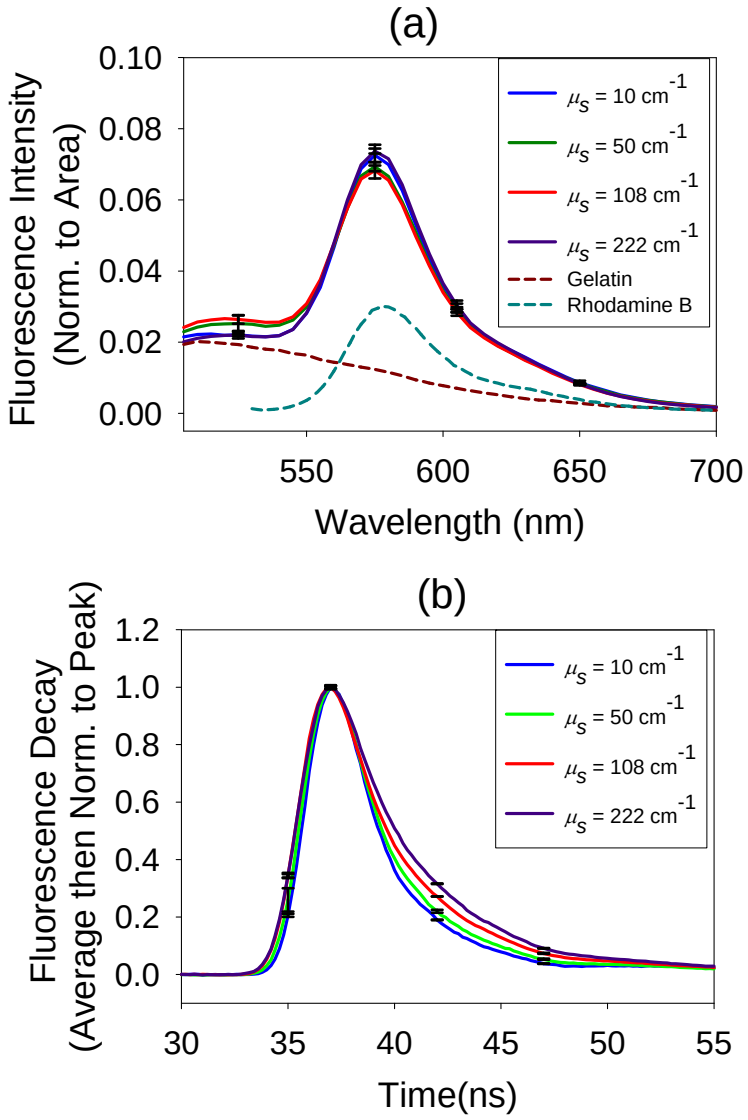

Figure 5.6. Wavelength-resolved (a) and time-resolved (b) fluorescence from tissue-simulating phantoms with varying scattering coefficients (measured with a source detector separation of 0.66 mm). Three sites on each phantom were measured. The spectra represent the average of the three sites, with error bars representing standard deviation. Panel (a) also includes spectra from pure gelatin and from a solution of rhodamine B in deionized water.

Figure 5.6(b) suggests that phantoms with increased scattering coefficients exhibited stretched waveform decay. The stretched waveform decay shown in **Figure 5.6(b)** for tissue-simulating phantoms with a μ_s of 108 cm^{-1} and 222 cm^{-1} (using a fiber-probe source-detector separation of 660 μm) was also observed for larger source detector

separations out to 4.66 mm (data not shown). The distortion of the waveform was observed for each source-detector separation measured, with the relative waveform differences between each phantom remaining the same. For the 4.66 mm source-detector separation, at which the diffusion approximation is valid, the experimentally observed trend matched the prediction of diffusion theory (**Figure 5.7**) [142]. In **Figure 5.7** the experimental results and the diffusion theory predictions were both time-shifted to align the rising shoulders of the decay curves for the two different scattering coefficients (108 cm^{-1} and 222 cm^{-1}). Additionally, both diffusion theory results were convolved with the corresponding instrument response functions from the phantom measurements. Computational studies employing Monte Carlo codes to model photon propagation are underway to further investigate the effect of increased optical scattering coefficients on the resulting transient fluorescence decay and extracted fluorophore lifetime [14,32,33].

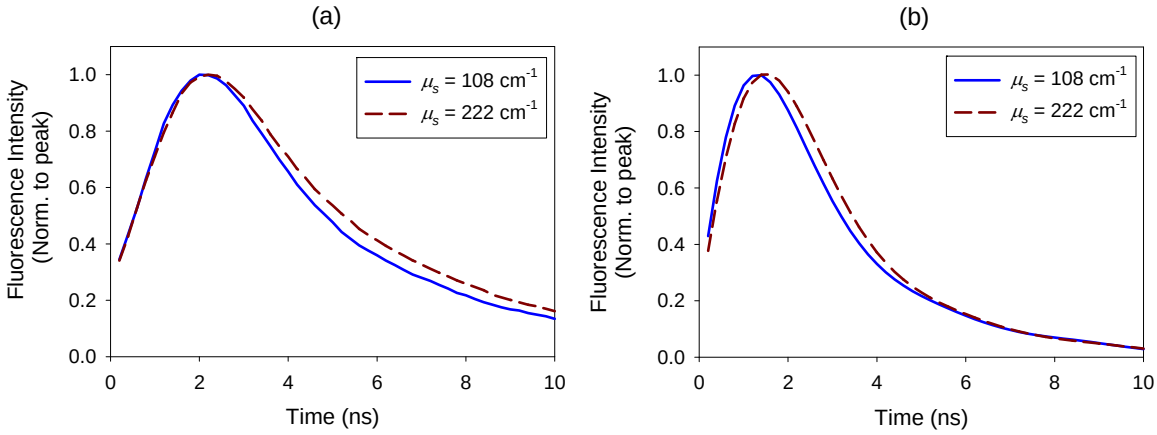

Figure 5.7. Measured time-resolved fluorescence decay curves from two phantoms with biologically-relevant scattering coefficients at a source-detector separation of 4.66 mm (a), compared with the predictions of diffusion theory (b). Each curve in (b) is a convolution of the diffusion theory result with the instrument response function of the corresponding tissue-simulating phantom. For the sake of comparison, the experimental results and the diffusion theory predictions were time-shifted to align the rising shoulders of the curves. In both panels, the time-resolved decay from the medium with the higher scattering coefficient (red dashed curve) was noticeably broader than the decay from the medium with the lower scattering coefficient (blue solid curve).

5.5 Discussion

Most clinical fluorescence instruments emphasize the spectral domain, often integrating a spectrograph and CCD camera for rapid data collection in which the entire spectrum is measured at once. In these systems, data is acquired over multiple laser shots for signal averaging. Most approaches for acquiring time-resolved fluorescence employ a pulsed laser and digital oscilloscope. The nitrogen laser is often employed because it is small, relatively low cost, and its UV wavelength (337 nm) excites endogenous fluorescence. However, the effectiveness of the nitrogen laser for rapid collection of time-resolved fluorescence is hindered by its relative low pulse repetition frequency.

In this report, we employed a 473 nm microchip laser (3 kHz repetition rate) and a specialized digitizer capable of collecting the data obtained at this rate. The system was tested on standard fluorophore solutions and tissue-simulating phantoms. WTMs from samples with fluorophore concentrations of 1 μM were acquired with speed (under 25 s for a WTM from 500 to 650 nm with a 5 nm step size and 125 laser pulses averaged) and precision (error less than 1% for Rhodamine 6G and Fluorescein solutions), without maximizing the sensing capabilities of the transient digitizer.

The autofluorescence intensity measured from biological tissues depends on several factors, including the excitation wavelength, fiber-probe geometry, and composition of the biological sample. It is likely that detected autofluorescence signals from biological tissues will be weaker than those from the stock fluorescent solutions used in this study. To compensate for this signal loss, system parameters can be changed to increase the detected fluorescence intensity. For example, the excitation fiber diameter can be increased in size to excite a larger sample volume and the detection fiber diameter can be increased to detect a larger portion of the emitted fluorescence photons. In addition, the

PMT gain can be increased in order to maximize the dynamic measurement range of the digitizer.

We note that the stretched behavior of the fluorescence decay curves from phantoms with increased scattering coefficients is under investigation. Preliminary results suggest that the Rhodamine B lifetime in the phantom is different than its value in cuvette solution, which may be due to the dependence of the fluorescence properties of Rhodamine B on its local environment[155]. Specifically, the lifetime of Rhodamine B within the phantoms may have been altered by the presence of the gelatin and microspheres. Studies are underway employing phantoms containing a more stable fluorophore (Rhodamine 6G[155]).

It is important to note that the system set-ups reported here were designed only for point measurements, not imaging. However, the system can be modified to perform scans of multiple points on a sample in order to generate spatially-resolved information. Spatial resolution can also be obtained by use of fiber-probes with multiple source-detector separations.

It is also important to note that the acquisition speed of this system is not fully optimized. Acquisition time depends on laser pulse repetition frequency, number of laser pulses averaged per waveform, and spectral resolution. In addition, there is the time overhead associated with moving from one wavelength to the next and downloading an averaged waveform. Much of the time needed to generate the WTM data presented in this report was consumed by data transfer to a computer and stepping of the monochromator. The actual time it takes for the stepper motor to advance to the next wavelength once the command has been received and recognized is very small. Likewise, the data transfer

time is very fast once the computer is alerted that data is ready for transfer and the computer communicates that it is ready to receive this data. Additional delays are caused by having the computer update the graphical display after each waveform.

Currently, waveform averaging is performed on the digitizer and, one at a time, the averaged waveforms are downloaded. However, the digitizer can store up to 4000 waveforms before its memory is full. If 100 laser pulses were averaged per waveform (including the 5X interleaving), the data associated with 40 such waveforms (corresponding to the wavelength range from 500 nm to 695 nm in steps of 5 nm) could be packed in memory. For a laser pulse repetition rate of 4000 Hz, the 100 pulses necessary per waveform are generated every 25 ms. The monochromator could be independently controlled to step every 25 ms without any intermediate communication once the sequence is initiated. In this scenario, the operator could hit a keystroke (or depress a foot pedal) to start the acquisition, then after a brief delay the full WTM would be collected in one second. Data transfer from the digitizer memory to the computer would take a few additional seconds, after which the system would be ready to repeat the process. The actual waveform averaging could then be performed on the computer, post data collection.

5.6 Conclusions

In this paper, we reported on the design and validation of novel technology for rapid, precise, and accurate acquisition of fluorescence wavelength-time matrices (WTMs) from fluorophore solutions and tissue-simulating phantoms. The clinically compatible technology employs a microchip laser with a 3 kHz repetition rate and a digitizer capable

of detecting at this rate. The system can rapidly acquire fluorescence WTMs with high signal-to-noise ratio (greater than 100 when averaging 125 laser pulses per emission wavelength). The compact size enables future system translation to a portable, clinically-compatible unit. Integrated fiber-optic probes to deliver excitation light and detect fluorescence emission provide the capability for remote sensing of fluorescence from biological tissues.

These results suggest that the system will be able to perform rapid and accurate measurements of time- and wavelength-resolved fluorescence in a biomedical environment. The accurate, rapid, and portable nature of the system, combined with the information-rich fluorescence data set supplied by WTM collection, suggest that the technology reported here is potentially useful for a number of biomedical optics applications in clinical settings.

Chapter 6.
Non-invasive assessment of implanted tissue-engineered constructs success *in situ* by quantitative diffuse reflectance spectroscopy

6.1 Introduction

Tissue-engineering and regenerative medicine promises improved clinical care for functional restoration of tissues damaged by disease or trauma. For example, implanting manufactured tissue-engineered constructs developed from a patient's own cells can heal oral wounds up to twice as fast as the current clinical standard-of-care [156]. Regulatory approval for such cell-based combinational devices requires reliable methods to assess pre-implantation construct viability *in vitro* and post-implantation construct success *in vivo* [157]. Unfortunately, current evaluation methods [158] are limited in that they are inherently qualitative, destructive, and time-consuming (*e.g.*, histology and immunohistochemical techniques) or are unreliable and lacking in spatial information (*e.g.*, molecular and biochemical assays) [159,160]. Non-invasive characterization techniques [159,161] are being developed to evaluate viability of *in vitro* tissue constructs, but are not compatible for rapid, portable measurement of constructs *in situ*.

Non-invasive evaluation techniques employed to assess tissue-engineered construct success *in situ* include computed tomography [162] and optical imaging [163-166]. However, these methods have limited ability to detect cellular proliferation and tissue neovascularization, both of which are tissue properties strongly associated with wound healing [167]. Therefore, in this study, we develop clinically compatible technology for real-time, quantitative diffuse reflectance spectroscopy (DRS) measurements on

engineered tissues *in situ*. This label-free, non-invasive approach is sensitive to tissue optical properties associated with cellular density and organization, as well as hemoglobin concentration and oxygenation [168,169]. Indeed, reflectance-based approaches have been employed for burn assessment [170] and wound analysis [169,171] studies. Here, we test the ability of quantitative DRS to assess post-implantation construct success *in situ* for a tissue engineered construct developed for oral soft tissue repair (*ex vivo* produced oral mucosal equivalents - EVPOME) [47,167].

6.2 Materials and methods

6.2.1 Construct culture protocol - Ex Vivo Produced Oral Mucosal Equivalents (EVPOME)

The clinical study protocol was approved by the University of Michigan (UM) Medical School Institutional Review Board. Human tissue samples were obtained from patients who provided written informed consent. All study practices were in accordance with the Declarations of Helsinki Guidelines.

EVPOMEs were manufactured over 11 days according to a previously reported protocol [47] using cells obtained from discarded surgical tissues from the UM Hospital. Primary human oral keratinocytes were enzymatically dissociated from the tissue samples and isolated keratinocyte cultures were established in a chemically-defined, serum-free culture medium (EpiLife and EDGS, Invitrogen) with 0.06 mM calcium, 25 μg/mL gentamicin, and 0.375 μg/mL fungizone (Sigma). Cells were twice passaged and cryopreserved. Prior to EVPOME manufacturing, donor cells were thawed and passaged up to two times. 200,000 cells/cm^2 were seeded onto a 1 cm diameter circular piece of acellular cadaver skin (AlloDerm®, LifeCell), hereafter referred to as the dermal

equivalent. Prior to seeding, the dermal equivalent was pre-soaked overnight in 0.05 μg/μL human type IV collagen at 4ºC. The seeded construct, now comprising keratinocytes and dermal equivalent, was submerged for 4 days (Days 1 to 4) in culture medium containing 1.2 mM calcium to promote cell proliferation. Then, the construct was raised to an air-liquid interface for an additional 7 days (Days 5 - 11) to induce cell stratification.

For all culture days, control constructs were maintained at 37ºC with 5% CO_2. Stressed constructs were maintained under those conditions for all culture days except for 24 hours from Days 9 to 10, when they were maintained at 43ºC [159]. This stressing condition was chosen to reduce cell viability and proliferation capabilities relative to experimental controls.

6.2.2 Study design – implantation cohort development and characterization

Study design in **Figure 6.1** details the development and characterization of 42 implanted constructs from 6 batches. A batch is defined as a set of control and stressed constructs from one distinct primary human cell donor (one patient). The study evaluated two implantation cohorts, constructs implanted for 1 week and those implanted for 3 weeks, and each cohort contained constructs from 5 distinct human patients. Replicates (duplicates and for Batch 6, triplicates) were included for all constructs in case any construct was compromised. (Indeed, surgical complications eliminated 3 of the 42 constructs from consideration, but their replicates were available for study.)

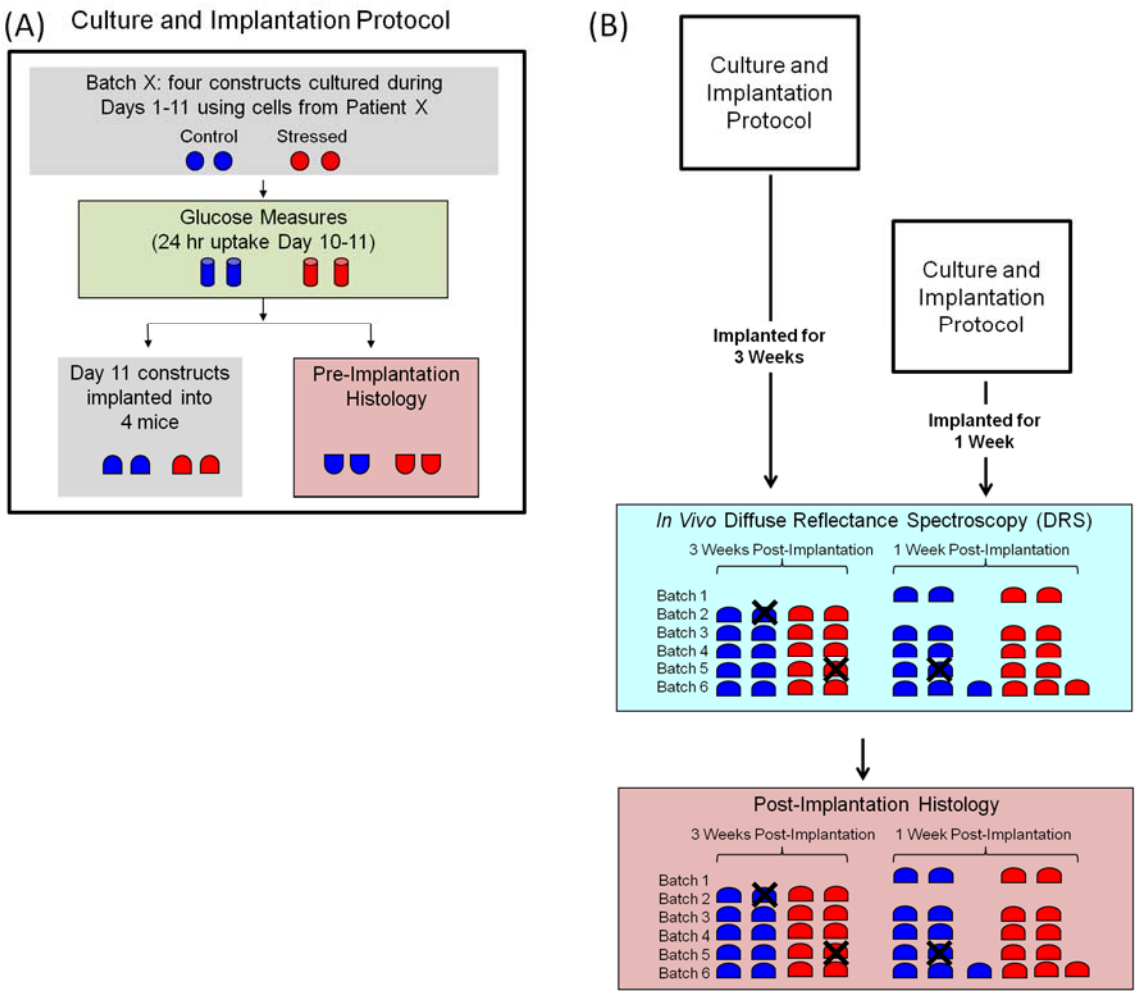

Figure 6.1. Study design.

Construct characterization prior to implantation included glucose measures and histology, while characterization after implantation included *in situ* optical DRS measurements and histology. Glucose concentration from stock media and Day 11 spent media were measured from ~1 µL aliquots with a glucose meter (ACCU-CHEK®, Aviva). Consumed glucose was calculated as Day 11 spent media glucose concentration subtracted from stock media glucose concentration. Percent glucose consumption was calculated as consumed glucose divided by stock media glucose concentration multiplied by 100.

Prior to implantation, a small (~2 mm wide) specimen of tissue near the edge of each manufactured (Day 11) construct was removed for histological examination. To process histology samples, the tissue specimen was fixed in 10% formalin, washed with phosphate buffered saline, and stored in a 70% ethanol solution. Specimens were stained with hematoxylin and eosin, cut into 5 μm sections, and preserved for future analysis and scoring on slides in duplicate or triplicate at the UM Dental School histology core. Representative histological sections from manufactured (Day 11) EVPOMES prior to implantation are shown in **Figure 6.2** Pre-implantation control EVPOMEs developed three characteristic layers: an air-exposed top keratin layer ~20-50 μm thick, a middle living cell layer ~30-50 μm thick, and a bottom dermal equivalent layer ~300-600 μm thick. Conversely, pre-implantation stressed EVPOMEs exhibited poorly defined keratin and living cell layers. These histological features led to the development of a quantitative histology score, described in 'Histology Scoring by Expert Panel.'

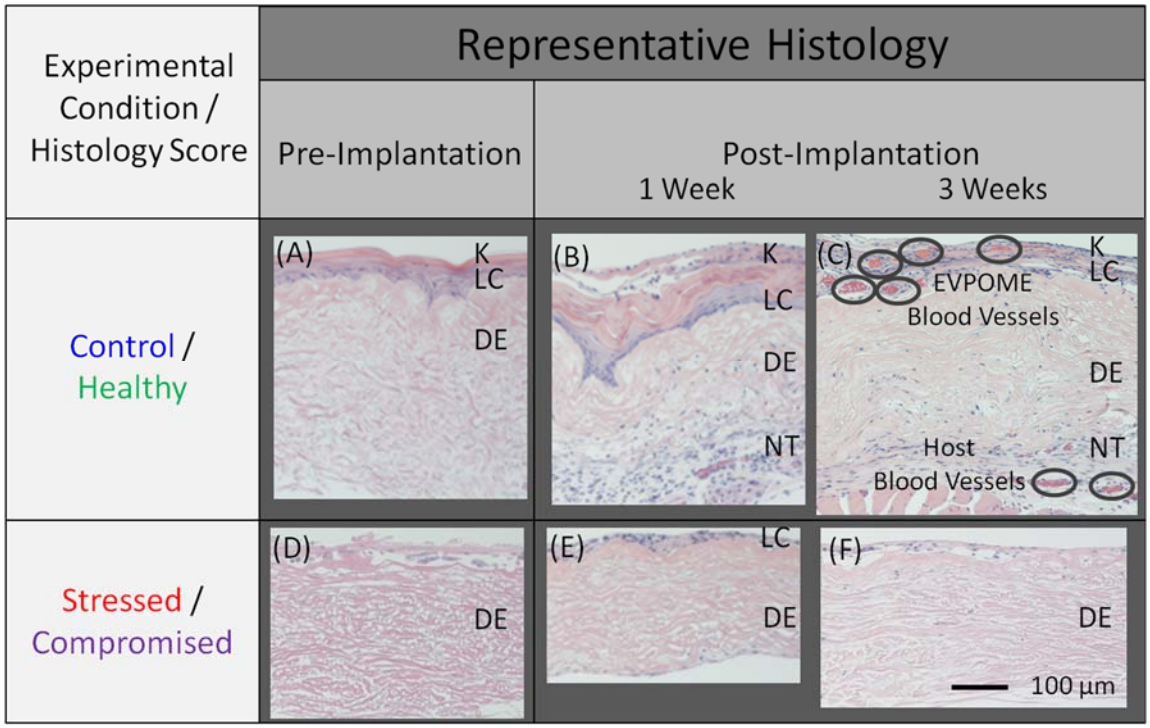

Figure 6.2. Representative hematoxylin and eosin (H&E) sections are shown from (A-C) control/healthy and (D-F) stressed/compromised constructs (A,D) pre- and (B-C,E-F) post-implantation sorted by experimental condition (control versus stressed) and histology score (healthy versus compromised). (A) Pre-implantation control histology section shows the three-layered EVPOME structure, with a top keratin layer (K), a middle living cell layer (LC), and a bottom dermal equivalent layer (DE). Mature healthy (majority of control) constructs developed keratin and living cell layers atop the dermal equivalent, whereas compromised (majority of stressed) constructs did not. Compared to (A) pre-implantation control/healthy constructs, (B,C) post-implantation control/healthy constructs showed (B,C) continued development of the keratin and living cell layers after 1 week and (C) visible revascularization after 3 weeks[16] post-implantation. Alternatively, stressed/compromised constructs had undefined keratin and living cell layers (D) pre-, (E) 1 week, and (F) 3 weeks post-implantation.

As shown in **Figure 6.3**, panel scores from destructive histological sections distinguished control from stressed Day 11 constructs, whereas non-invasive glucose measures were unable to reliably distinguish control from stressed Day 11 constructs.

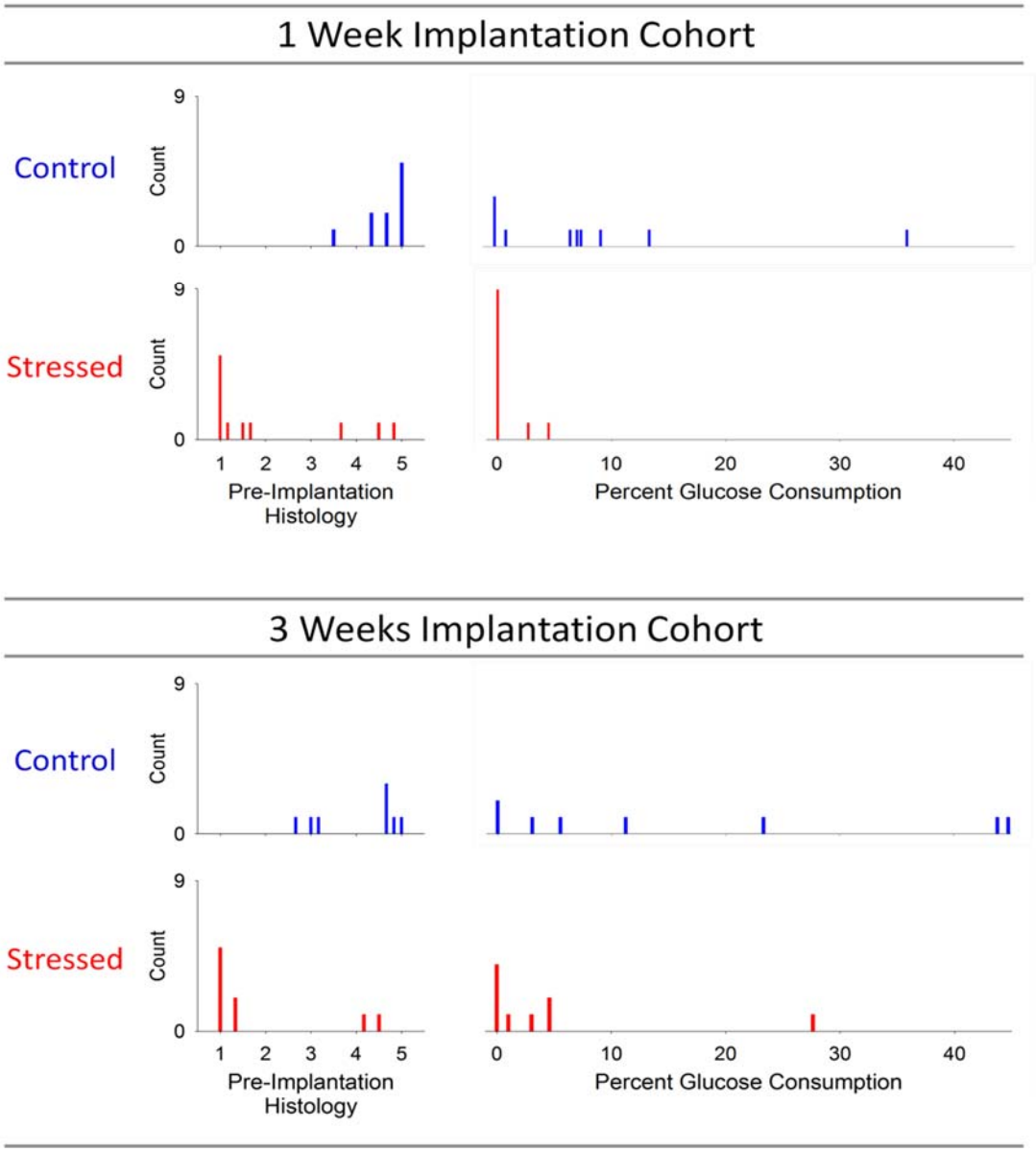

Figure 6.3. Pre-implantation construct success was characterized by histology and percent glucose consumption. (left column) Sorted by pre-implantation histology score, 100% of control constructs and only 25% of stressed constructs had a pre-implantation histology score > 2. (right column) Sorted by percent glucose consumption, only 61% of control constructs and 5% of stressed constructs had a percent glucose consumption > 5%. When sorted by cohort, pre-implantation histology score distinguished control from stressed constructs *(*p = 0.03 for constructs to be implanted for 1 week, p = 0.01 for constructs to be implanted for 3 weeks), whereas percent glucose consumption did not (p = 0.12 for constructs to be implanted for 1 week, p = 0.09 for constructs to be implanted for 3 weeks).

6.2.3 Construct implantation protocol – murine model

Day 11 EVPOMEs were implanted into 7 to 8-week old female severe combined immunodeficient (SCID) mice according to a previously developed protocol[167]. The UM Committee on Use and Care of Animals approved the study protocols.

To implant constructs, mice were anesthesized and their dorsal skin disinfected (betadine, Purdue Products L.P.) before a full-thickness curvilinear incision was made down to the panniculus carnosus to create a skin pouch. The skin pouch was ~2.0 cm^2, which was sufficient to house a ~1.0 cm^2 construct. Inside the pouch, the construct's dermal equivalent side was placed onto the animal's muscular fascia. The top keratin layer of the construct was covered with a thin silastic sheet (~130 μm thick) cut to twice the construct diameter to prevent adherence with the animal skin. The skin pouch was secured with Autoclip (Becton Dickinson).

As shown in the representative histology images in **Figure 6.2**, during post-implantation wound healing, control constructs developed an increased thickness of the top keratin and middle living cell layers and notable revascularization, whereas stressed constructs exhibited relatively less revascularization and a poorly defined or absent cell layer.

6.2.4 Tissue diffuse reflectance spectroscopy instrumentation

Diffuse reflectance spectra were collected on tissues *in situ* using a clinically-compatible prototype fiber-optic reflectance spectrometer[27,31]. Briefly, a fiber-optic probe (QF600-8-VIS/NIR, Ocean Optics), shown in **Figure 6.4**, directed broadband white light from a tungsten halogen lamp (HL 2000FHSA, Ocean Optics) to the sample. The fiber-optic probe comprised seven excitation fibers (600 μm diameter) beveled at 60º relative to tissue normal and a central, flat-tip 600 μm diameter optical fiber to collect photons

scattered out of the tissue. Compared to conventional flat tip optical fibers, beveled fibers increase interrogation of tissue near the construct surface (here, optimized for interrogating a tissue's top ~600 μm, the estimated average thickness of an EVPOME). Thus, employing a beveled fiber-optic probe enabled interrogating the thin tissue construct while mitigating interrogation of the native animal tissue. Ray-traced, non-sequential simulations in ZEMAX®, shown in **Figure 6.4**, visualized excitation light path from beveled fibers (red and green rays), elastic scattering from tissue within the construct, and emission light path (blue rays). Overlap of excitation light and emission light shows optical interrogation volume primarily constrained to within the construct's top 600 μm. Construct was modeled with optical scattering properties of dermal equivalent [35]. Collected photons were detected by a spectrograph (MS 125, Oriel Instruments) coupled to an intensified charge-coupled device camera (ICCD 2063, Andor Technology).

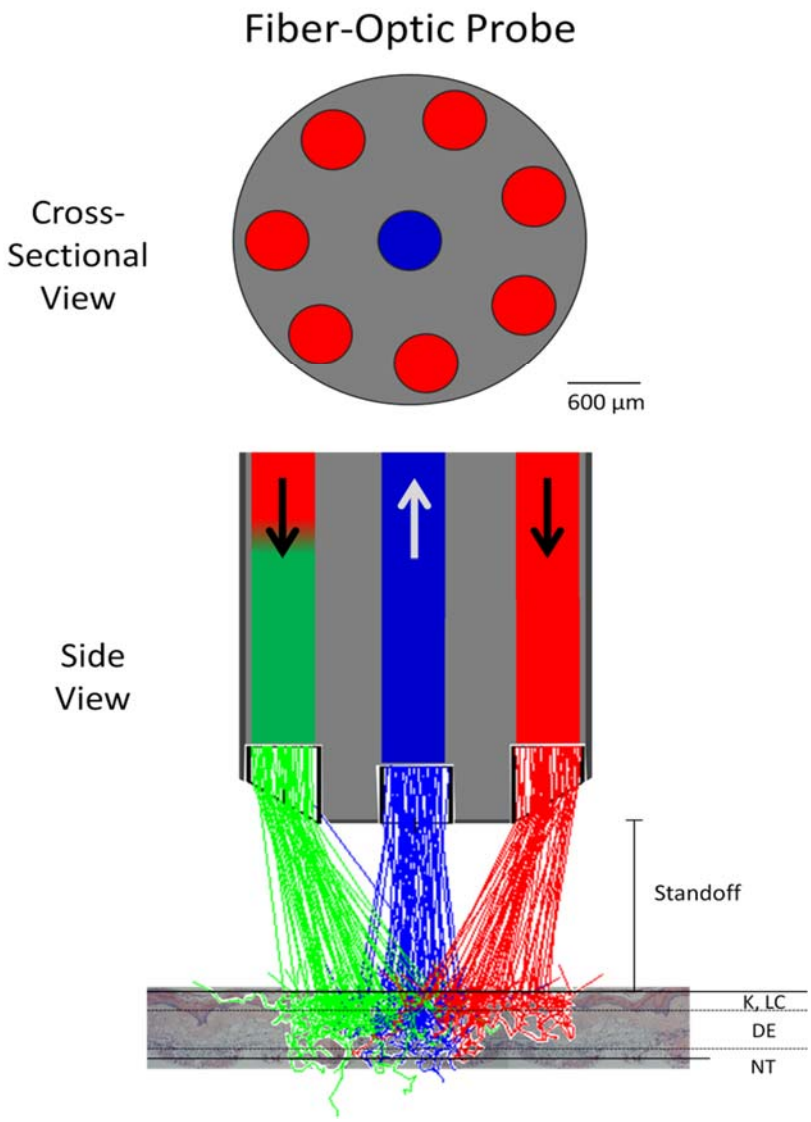

Figure 6.4. Diffuse reflectance spectroscopy instrumentation selectively interrogated mature EVPOME constructs. A standoff fiber-optic probe enabled rapid, portable, and repeatable measurements. Broadband light was delivered to and collected from the construct with a beveled fiber-optic probe, shown in cross-sectional and side view. A ray traced model, employed in ZEMAX® with tissue optical properties[18] of dermal equivalent, estimated the optical interrogation volume[18] in mature constructs. Cross-sectional view shows the (red) 7 excitation beveled fibers around a (blue) common detection fiber. Side view shows simulated (green and red) excitation photons overlap with (blue) emission photons within the constructs keratin, living cell, and dermal equivalent layers without interrogating the native tissue. One excitation fiber ray is colored green to illustrate the interactions of rays from different excitation fibers more clearly.

6.2.5 Diffuse reflectance spectroscopy measurement protocol

EVPOME constructs were measured optically after being implanted in the murine skin pouch for 1 week and 3 weeks, which were suitable time frames to promote wound healing [167,172]. Mice were administered buprenorphine subcutaneously for analgesia and isoflurane via a nose cone for anesthesia. To mimic future clinical studies on constructs implanted in human oral mucosa, a curvilinear incision was made through the animal's skin and the silastic sheet was removed, thereby exposing the constructs to air prior to optical measurement. Mice were placed prone onto a heating pad set to ~100°F. The mouse and heating pad were then placed on a stage capable of tilting so that the construct's surface could be oriented approximately perpendicular to the optical axis of the DRS fiber-optic probe. The DRS probe was mounted on a micrometer-guided 3-axis linear translational stage to position the probe at a controlled distance above a tissue measurement site. Up to three randomly selected construct sites per animal were measured at 1.0, 1.5, and 2.0 mm standoff distances above the tissue surface. An off-construct site was measured to characterize hemoglobin absorption from native animal tissue surrounding implanted constructs. Individual DRS measurements were acquired in 100 milliseconds. DRS investigators were blinded to a construct's experimental condition during these measurements.

6.2.6 Optical data set and pre-processing

Measured diffuse reflectance spectra were background-corrected for ambient light, corrected for the spectral instrument response, and smoothed with a ten-point moving average filter [27]. Corrected and smoothed spectra were normalized to peak intensity so that further quantitative analysis would characterize relative spectral differences in tissue

optical properties. Exclusion criteria were developed to eliminate measurements with excessive blood absorption, attributed either to thin dermal equivalent (< 400 μm) or to surgical complications that artificially increased local blood content. For constructs implanted for 1 week, spectra with normalized reflectance intensity greater than 0.55 at 410 nm or 0.75 at 586 nm were excluded. For constructs implanted for 3 weeks, spectra with normalized reflectance intensity greater than 0.2 at 410 nm or 0.5 at 575 nm were excluded. Resulting data set is shown in **Table 6.1**. Exclusion criteria differed between implantation cohorts, because constructs implanted for less time were expected to have less hemoglobin absorption. Applying the exclusion criteria eliminated 52 out of 135 measurements from constructs implanted for 1 week, and 32 out of 108 constructs implanted for 3 weeks.

Table 6.1. Number of batches, constructs, sites, and measurements in data set after employing exclusion criteria. Batches indicate control and stressed constructs cultured from one distinct primary human cell donor.

Post-Implantation	Batches	Constructs	Sites	Meas.		Batches	Constructs	Sites	Meas.
1 Week									
Control	5	9	19	50	Healthy	5	11	17	43
Stressed	5	7	13	33	Compromised	5	5	13	33
Total	5	16	32	83	Total	5	16	30	76
3 Weeks									
Control	5	11	23	59	Healthy	5	13	24	59
Stressed	4	5	9	24	Compromised	3	3	6	17
Total	5*	16	32	83	Total	5*	16	30	76

6.2.7 Quantitative reflectance spectral analysis

Measured reflectance spectra were analyzed with MATLAB® software using built-in principal component analysis function and home-built spectral intensity classifiers.

Figure 6.5 shows representative reflectance spectra from control and stressed constructs (at 2.0 mm standoff) and dermal equivalent compared to principal component 6 and hemoglobin absorption [168]. Principal component 6 accounted for key variations

attributed to hemoglobin absorption and cell scattering, whereas principal components 1-5 accounted for the similarities between control/healthy and stressed/compromised constructs. These similarities include optical contributions from dermal equivalent and absorption from baseline concentrations of hemoglobin.

Two spectral intensity classifiers were employed to classify constructs, named the total and oxygenated blood indicator and the total blood and cell scatterer indicator.

Total and oxygenated blood indicator:

$$[R(500\ nm) - R(422\ nm)] * [R(560\ nm) - R(542\ nm)]$$

Total blood and cell scatterer indicator:

$$[R(452\ nm) - R(422\ nm)] / [\text{slope from } 650 \text{ to } 760\ nm]$$

$R(\lambda)$ indicates the relative reflectance intensity value at λ. Spectral intensity classifiers characterized relative amount of hemoglobin absorption [173] (intensity differences between hemoglobin isosbestic points: 422, 452, and 500 nm), relative oxygenated hemoglobin (intensity differences between maximum and minimum oxygenated hemoglobin absorption wavelengths: 542 and 560 nm), and tissue scattering (slope from 650-760 nm [168]).

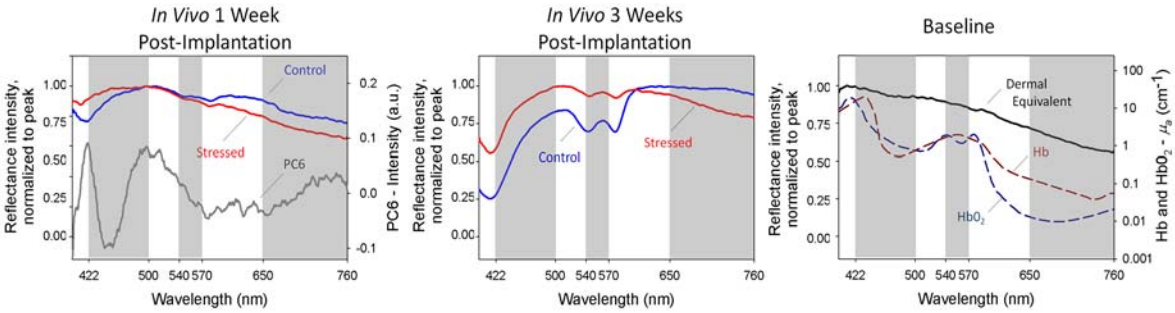

Figure 6.5. Representative DRS measurements at 2.0 mm standoff from (left) 1 week and (middle) 3 weeks post-implantation constructs compared to (right) dermal equivalent that was pre-soaked in phosphate buffered saline. (gray overlays) The primary wavelengths employed for spectral intensity classification correspond to (right) hemoglobin absorption bands[19], cellular and collagen scattering (slope from 650-760 nm), and the peaks and valleys of (left) principal component 6 (PC6). As expected, (right) hemoglobin absorption was lowest from (left) 1 week post-implantation stressed and greatest from (middle) 3 weeks post-implantation control constructs.

6.2.8 Histology scoring by expert panel

Histology scoring classification criteria were developed and implemented by a blinded panel of three expert readers. Readers evaluated construct pre-implantation viability and post-implantation construct success on a 5 point scale from 1-5, with 1 being least and 5 being most viable. Evaluation criteria were the health of the basal cell layer, the cellular organization of the living cell layer, and the structural quality of the keratin layer. For example, 1 indicated a construct with few to no cells, little or no cellular organization, and an unstructured keratin layer, while 5 indicated a construct with a thick layer of rounded basal cells, thick superficial layers comprised of many gradually flattening cells, and a compact keratin layer. Overall, control constructs had healthier basal cells, increased cellular organization, and better structural quality of the keratin than stressed constructs. Tissue revascularization was not reliably assessed with H&E staining and

therefore not an evaluation criterion. Readers internally calibrated by selecting histology images unanimously agreed to be 1 and 5. Then, readers scored each construct's histology slide while blinded to the constructs experimental condition and the other readers' scores.

6.2.9 Statistical analysis

Statistical analysis was performed at the batch level to account for the hierarchal nature of the measurements, including intra-batch and standoff related correlations. For example, a mixed-effects model accounted for correlations from standoff measurements from the same construct site, measurements from sites on the same construct, and measurements from constructs from the same batch. For each parameter, models calculated the mean difference between control/healthy and stressed/compromised constructs. All tests were conducted using a 0.05 significance level. If batch-level analysis was not significant, a less rigorous statistical test was performed by treating all measurements as independent with a Wilcoxin rank-sum test. Significance was determined with a 0.05 significance level.

6.3 Results

6.3.1 Glucose readings are non-invasive, but inherent measurement variability limits ability to distinguish control from stressed constructs

While non-invasive, glucose readings are highly variable (see **Figure 6.3**). Therefore, when percent glucose consumption was compared for individual cohorts, these readings did not distinguish control from stressed constructs (p = 0.12 and 0.09 for cohort constructs to be implanted for 1 week and 3 weeks, respectively). Because glucose

measurements were measured pre-implantation, readings from cohorts were grouped and reanalyzed, increasing the sample size and statistical power. When grouped, glucose did distinguish control from stressed constructs (p = 0.001). However, the high inherent variability of measurements (ranging from 0-40% consumption) indicates that glucose readings are an unreliable tool to distinguish control from stressed constructs.

6.3.2 Histology sections are able to distinguish control from stressed constructs, but are destructive

Figure 6.6 compares pre- and post-implantation histology scores for both implantation cohorts. Pre-implantation histology scores distinguished control from stressed constructs for both implantation cohorts (p = 0.03 and 0.01 for cohort constructs to be implanted for 1 week and 3 weeks, respectively, and $p < 0.001$ after combining cohorts) and post-implantation histology scores distinguished control from stressed constructs for both implantation cohorts (p = 0.02 and 0.03 for cohort constructs implanted for 1 week and 3 weeks, respectively). After implantation for 3 weeks, histology scores were significantly lower than corresponding pre-implantation histology scores (p = 0.04). The mean difference between histology scores of constructs from the 3 weeks implantation cohort and their corresponding pre-implantation histology scores was ~2.2, whereas corresponding difference in histology scores of constructs from the 1 week implantation cohort was ~0.7. This notable histology score decrease after 3 weeks of implantation was attributed to construct wound healing. As wounds healed, human cells slough off and are replaced by native animal cells. While our optical technology was sensitive to the recruited animal cells, our expert panel scored such constructs poorly because the constructs lacked human cells.

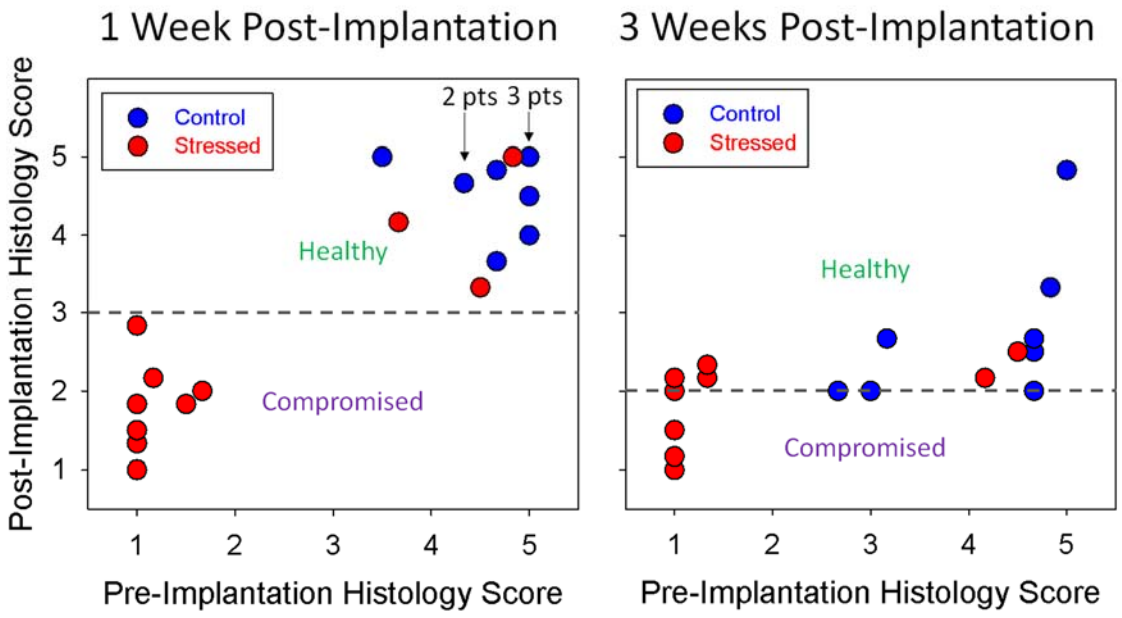

Figure 6.6. Pre-implantation histology scores from control and stressed constructs predicted post-implantation histology scores 1 week post-implantation, but not 3 weeks post-implantation. (left) Post-implantation histology scores from 1 week post-implantation constructs distinguished control from stressed constructs (p = 0.02). (right) At 3 weeks post-implantation, majority of constructs had average post-implantation histology score between 2 and 3. While histology score distinguished control and stressed constructs (p-value = 0.03), the decrease in histology score for control constructs indicated advanced stages of wound healing, where low histology scores indicated the invasion of host cells. Gray dotted lines indicate employed thresholds to characterize healthy and compromised constructs based on panel histology score (for **Figure 6.7**).

6.3.3 Reflectance spectra distinguish constructs sorted by experimental condition and post-implantation histology score

Figure 6.7 shows averaged reflectance spectra from both implantation cohorts sorted by experimental condition (*i.e.*, control versus stressed) and histology score (*i.e.*, healthy versus compromised determined by histology score threshold from **Figure 6.5**). Measured spectra have characteristics of hemoglobin absorption at ~420 nm and between ~510-575 nm and tissue scattering from ~650-760 nm [168]. Measured spectra from off-

construct sites showed greater hemoglobin absorption than construct sites, confirming that non-excluded reflectance spectra primarily interrogated the implanted construct and not native tissue (data not shown).

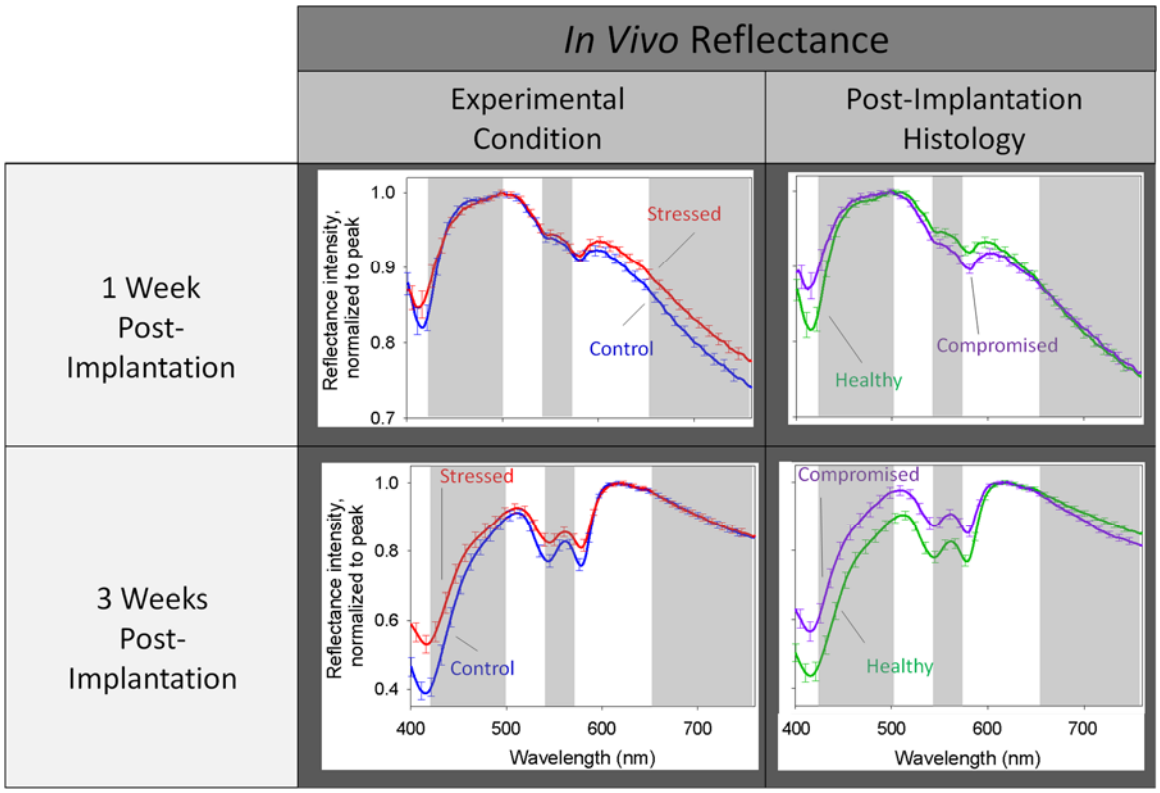

Figure 6.7. Diffuse reflectance measurements were normalized to peak, averaged, and renormalized to peak. These average diffuse reflectance measurements from (left column) 1 week and (right column) 3 weeks post-implantation constructs clearly distinguish measurements from constructs sorted by (left column) experimental condition and (right column) post-implantation histology score. The absorption bands near ~422 nm and ~540-570 nm were attributed to hemoglobin absorption [173], whereas the higher intensity regions near between 650-760 nm were attributed to sample scattering properties [168]. As expected, average reflectance spectra differed most when classifying constructs according to post-implantation histology, which accounted for stressed constructs that grew well *in vivo*. Gray overlays emphasize primary wavelength ranges of interest from **Figure 6.4**. Error bars represent standard error.

6.3.4 Reflectance parameters distinguish constructs sorted by experimental condition and histology score

Optical parameters classified measurements from constructs implanted for 1 week based on experimental condition and post-implantation histology analysis (**Figure 6.8**). Compared to experimental condition, constructs sorted by post-implantation histology classified stressed constructs that grew well as healthy. Higher absolute values of calculated metrics for spectral intensity classifiers indicate greater total and oxygenated hemoglobin absorption and tissue scattering.

Optical parameters did not significantly distinguish constructs implanted for 3 weeks at the batch level ($p > 0.05$). Based on the classification threshold in **Figure 6.6**, 2 of the 5 batches with constructs implanted for 3 weeks only had healthy constructs. Therefore, the batch-level study was effectively reduced to N = 3 batches. At the measurement-level, the total and oxygenated blood indicator distinguished measurements of healthy constructs from measurements of compromised constructs ($p = 0.04$).

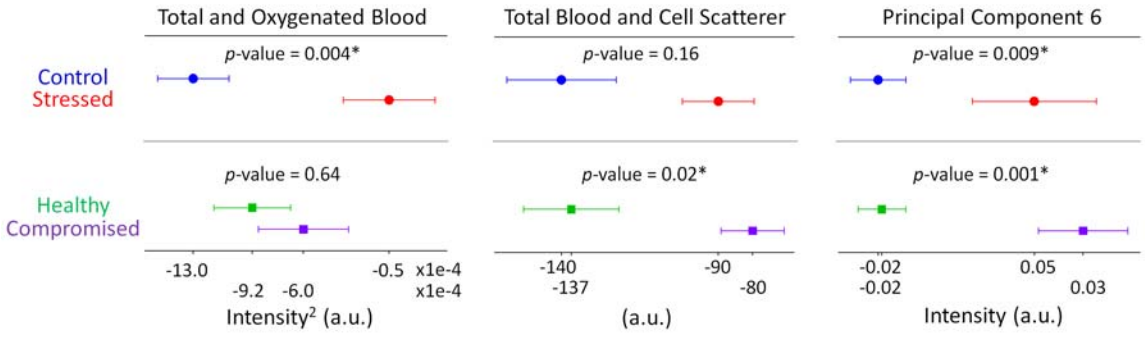

Figure 6.8. *In vivo*, non-invasive, and label-free reflectance spectra, characterized by 3 reflectance parameters, distinguish 1 week post-implantation constructs at the batch level after sorting by experimental condition (control versus stressed) and histology score (healthy versus compromised). Statistically significant parameters indicate that DRS characterizes tissue-engineered construct success *in vivo*. Error bars represent standard error.

6.4 Discussion

Measured reflectance spectra from EVPOMEs undergoing wound healing *in vivo* are sensitive to tissue absorption, attributed to revascularization, and tissue scattering, attributed to relative thickness of cell layer to dermal equivalent. In general, *in vitro* EVPOME morphology is homogeneous [156]. However, during *in vivo* wound healing, EVPOMEs may become heterogeneous. In our study, up to three unique sites were measured per construct. To account for local heterogeneities in tissue absorption and scattering, future work will include analyzing more sites to effectively map the construct's surface. Furthermore, tissue histology samples will be obtained from sites < 2 mm from the measurement to account for these heterogeneities, rather than collecting one representative histology sample per construct.

In this study, control constructs were compared to compromised constructs developed by pre-implantation thermal stressing. Histology scores confirmed that thermal stressing damaged the construct's morphology and biochemistry, consistent with previous reports [159,161]. Alternative stressing mechanisms to reduce the viability of tissue constructs include starvation [159], culturing constructs with higher-than-normal calcium concentrations [161], or altering cell biochemistry with immunosuppressant drugs [161]. For each stressing mechanism, histology confirmed constructs were compromised similar to thermal stressing, with notable damage to the keratin and living cell layers that alter a construct's tissue scattering and absorption properties. Therefore, the hallmarks of compromised constructs identified by DRS from thermal stressing are expected to be applicable to distinguish constructs compromised with alternative stressing mechanisms.

Measurements were collected with a variable standoff fiber-optic probe designed for interrogating ~600 μm into the sample, estimated as the average thickness of an

EVPOME. In practice, dermal equivalent was thinner than specified. Thin dermal equivalent manufactured EVPOMEs < 600 μm thick. Therefore, the interrogated sample area may have included EVPOME and native host tissue, introducing higher levels of tissue absorption from the vascularized muscle tissue underneath EVPOMEs. Exclusion criteria were developed to remove these measurements with excessive absorption, consistent with optical measurements from off-construct sites. Future work will employ a fiber-optic probe that interrogates < 600 μm into the sample to characterize constructs developed thin dermal equivalent (< 400 μm thick).

In this study, fiber-optic probe interrogated the superficial construct layers with a fixed standoff, controlled with micrometer translation stages. The standoff maximized interrogation of the construct, and thus minimized interrogation of the host tissue underneath. In clinical practice, a clinician will employ the fiber-optic probe by hand for remote sensing, requiring a fixed standoff achieved with an optical spacer. The optical spacer will control the standoff distance and minimize optical losses from light transport through air.

Histology scoring showed that EVPOMEs implanted for 3 weeks were at advanced stages of wound healing. That is, histology sections showed that native mouse cells had largely replaced human keratinocytes. Because our optical instrumentation cannot distinguish optical signatures from human and animal cells, DRS measurements were unable to distinguish healthy from compromised constructs implanted for 3 weeks at the batch level (but did distinguish healthy from compromised constructs at the measurement level). Future work will include studying intermittent stages of wound healing from constructs implanted for between 1 week and 3 weeks.

6.5 Conclusion

Diffuse reflectance spectroscopy (DRS) characterized tissue-engineered constructs implanted for 1week and 3 weeks. Compared to measurements of stressed constructs, measured reflectance spectra from control constructs had greater hemoglobin absorption, relative concentration of oxygenated hemoglobin, and tissue scattering from cell nuclei. Optical metrics characterized these differences to classify healthy from compromised constructs implanted for 1 week ($p < 0.01$ at batch level). After 3 weeks of implantation, most constructs had reached advanced stages of wound healing. Optical metrics were unable to distinguish healthy from compromised constructs at the batch level, but did distinguish healthy from compromised constructs at the measurement level ($p = 0.04$). Overall, DRS is a rapid, easy-to-use, and sensitive tool for the *in vivo* analysis of tissue-engineered construct wound healing that can be employed for future clinical studies with a portable, hand-held, fiber optic probe.

Chapter 7.
Clinical translation and commercialization of optical spectroscopy technology

7.1 Clinical applications

The sensitivity of optical measurements to disease-related biochemical and morphological changes in tissue has led to promising developments in reflectance- and fluorescence-based diagnostic technology for a wide variety of clinical applications. These applications range from cancer diagnostics to dental caries [174] to inflammatory diseases, such as arthritis [175] or Crohn's disease [176]. Potential future clinical applications include diabetes, neurological diseases, arthritis, and metabolic diseases [177]. Additionally, optical techniques have been developed and employed for clinical cancer diagnostics for nearly two decades, as chronicled in a recent review article [178]. Cancers are characterized by a number of biological and morphological tissue changes, which can be markedly different among tissue types, thus requiring specific optical instrumentation and analysis algorithms for accurate classification. A wide variety of cancers have been previously studied with fluorescence sensing methods, including head and neck [179] (including oral [180]), skin [181-184], breast [7,185], colon [6], brain [186], lung [187,188], stomach [189,190], prostate [191], cervix [119], ovarian [192], and pancreatic [3,23,35,101]. Although some of these studies were *ex vivo*, the fluorescence technology reported is clinically translatable and the research goal is to develop *in vivo* clinical technology.

7.2 Clinical design considerations

7.2.1 Regulatory issues

Device safety is charged to the device manufacturer, both during the FDA approval process and afterwards, when monitoring the device once it is employed for clinical use. To achieve FDA approval, Class III clinical devices (any device that is employed to support human life, prevents human harm, or presents an amount of unreasonable risk of patient injury or illness) must undergo FDA pre-market approval (PMA) to assess their safety and effectiveness, and to designate them as an adjunct or replacement technology [193]. For a specific technology that poses potential risk to patient health, safety, or welfare, an investigational device exemption (IDE) may be required. Devices employing laser sources add additional concerns regarding photosensitivity, including radiation hazards and thermal tissue heating [25,194].

The first regulation for clinical fluorescence technologies was enacted in 1990 with the Safe Medical Devices Act, shortly followed by Medical Devices Amendments in 1992. In 1997, the FDA outlined clear guidelines for developing fluorescence technology targeting cervical cancer [195], which can be extended to similar optical technologies. These FDA requirements outline the procedure for Investigational Device Exemption/Investigational New Drug (IDE/IND) approval and define the permitted clinical uses of the technology. Four uses were permitted: (1) adjunct tool to cytology, (2) screening device after abnormal cytology, (3) localize biopsy sites, and (4) primary screening as an alternative to cytology.

Optical clinical technologies typically indicate a significant risk device, requiring an IDE application, which must include all technology details, including the device description, a complete list of the patient-contacting materials, and software details. Preclinical testing

must conform to Good Laboratory Practices (GLP), which are general practice guidelines to ensure that biocompatible materials and optical radiation levels employed will not compromise patient safety [196].

For laser-based devices, safety must be demonstrated according to American National Standards Institute (ANSI) standards [197]. Before clinical trials begin, a local institutional review board (IRB) must review and approve the study. To gain IRB approval, technology must demonstrate two layers of safety, defined as either procedural or instrument based barriers to protect the patient from the technology and vice versa [198]. The detailed requirements for performing Phase I and II clinical trials are discussed in the Clinical Trials section below.

Also pertinent to study success is the sterilization of all materials that will contact the patient [199]. Detailed guidelines regarding disinfection and sterilization practices for healthcare facilities were outlined in 2008 by the Healthcare Infection Control Practices Advisory Committee (HICPAC) [200]. Specific to fiber-optic probes were sterilization guidelines for steam, flash steam, and ethylene oxide sterilization. Previous studies have outlined procedures used to sterilize fiber-optic probes and endoscopes [64,201]. A new probe disinfector has been FDA approved for disinfection of transesophageal ultrasound probes, but has yet to be employed for reflectance or fluorescence fiber-optic probes and endoscopes [202].

Recently, regulatory processes for medical imaging technology seeking FDA approval and clinical use were discussed for four separate medical imaging modalities (including near-infrared fluorescence and multispectral fluorescence imaging) [196]. The study concluded that each of the four technologies was at a different stage of the translational

pipeline (**Figure 7.1**) and that each group had taken a slightly different approach to gaining approval. This outcome suggested that a standardized pipeline would advance promising technology to a commercial stage more efficiently, returning greater value from the funding provided by both private and taxpayer dollars.

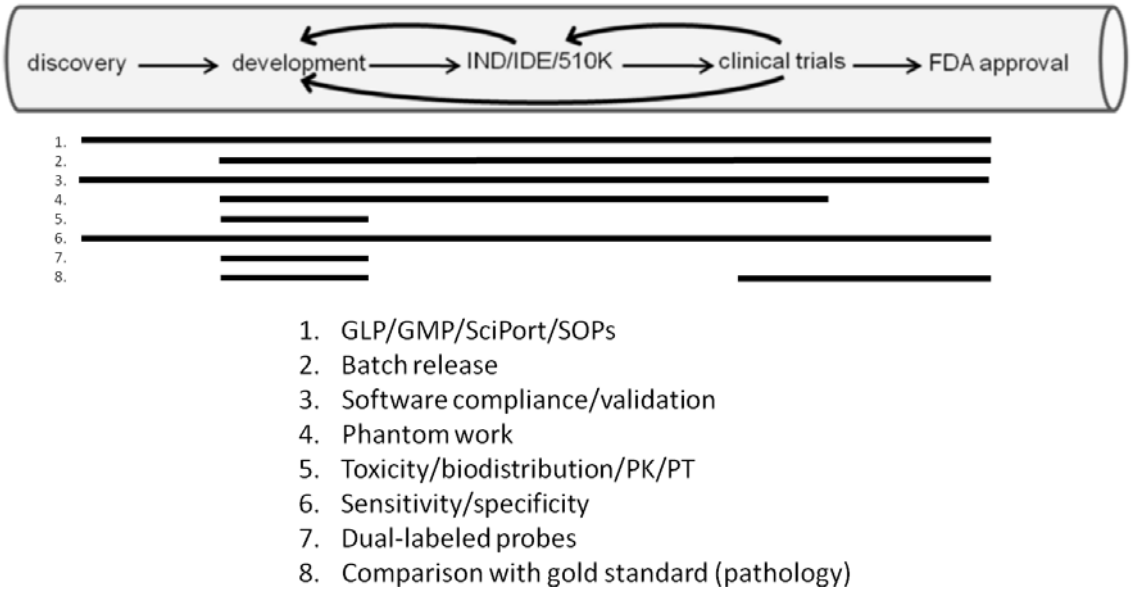

Figure 7.1. Schematic of the 'translational pipeline' from device discovery through FDA approval. An emphasis is placed on the iterative process during device development and clinical trials [196]. The goal of a common translational pipeline is to improve and standardize the approval process for medical imaging technologies. With faster approval times, and thereby expedited returns on investment, investors should be more apt to fund clinical imaging technology companies developing fluorescence instrumentation. (Adapted with permission from [196]).

7.2.2 Integration with hospital environment

To successfully integrate fluorescence technology into the clinic, it must possess several attributes to ensure adoption by physicians [203].

In clinical diagnostic and surgical procedures, clinicians make real-time decisions based on the findings of the procedure (e.g., the presence or absence of cancer). Therefore,

clinicians require instrumentation that immediately provides accurate, reliable diagnostics. Optical technologies must significantly improve upon a physician's current tools. If diagnostics are negligibly improved, the training time and equipment cost cannot be justified by the physician or hospital. The technology must also uphold IRB safety standards [198] and include back-up plans that protect the patient from potential device failure.

Optical instrumentation for disease detection may be used by clinicians throughout a procedure. For instance, optical instrumentation for cancer detection could be employed for both point detection and tumor margin analysis. Therefore, the technology should be designed to smoothly incorporate into the current clinical protocol. To achieve this goal, the instrument should be intuitive to use and it should provide the clinician with diagnostically-significant information that enables an improvement upon current methods for disease detection. This information should be easy for the clinician to interpret: for fluorescence imaging, displays should incorporate well-understood color schemes (*e.g.,* green for go, red for stop) and false coloring for clear distinction of healthy and diseased tissue; for point detection, the instrument should clearly indicate the presence or absence of disease (*e.g.,* H for healthy, D for diseased) on an easy-to-read interface within the clinical procedure room [204].

7.2.3 Clinical trials

Before a new medical technology can be made commercially available, it must successfully undergo a series of clinical trials [205][206]. Phase I clinical trials employ a group of 20-80 patients and are focused on evaluating the safety of the technology. Phase II clinical trials involve a patient set of 100-300 people and are employed to test both the

effectiveness and the safety of the technology. Phase III clinical trials include 1,000-3,000 patients, a large enough sample size to compare the new technology to currently-employed techniques and develop protocols for safe use of the technology. Phase IV clinical trials occur after marketing of the technology has begun, and they are designed to gain a more complete understanding of the advantages and drawbacks of the new technology so that a strategy for using of the technology can be optimized.

Numerous fluorescence-based techniques have undergone clinical trials. For example, from 2002-2009, the ability of a fluorescence-based device to detect cervical (pre-)cancer was tested in a clinical trial sponsored by the M. D. Anderson Cancer Center (Houston, TX) in collaboration with the National Cancer Institute [206]. In this trial, 100 patients who were undergoing colposcopy at one of five different clinical locations were also given a fluorescence-based cervical examination, and these results were employed to assess the diagnostic accuracy of the fluorescence technology. The same sponsor and collaborator conducted a larger clinical trial from 1998-2009 that enrolled 1,070 healthy patients [207]. In this trial, fluorescence and reflectance measurements were acquired from each of two sites on the cervix (one normal columnar site, one normal squamous site) and biopsies were obtained from both of these locations. The goal of this trial was to better characterize the optical spectra of normal cervical tissues, so that normal tissue, inflamed tissue, and pre-cancerous tissue could be better distinguished from each other using fluorescence- and reflectance-based techniques. Techniques assessed in these trials were employed to distinguish diseased tissues (moderate dysplasia, severe dysplasia, or malignant) from non-diseased tissues (mild dysplasia or non-dysplastic) with a sensitivity

of 100%, specificity of 71%, and area under the receiver operating characteristic (ROC) curve of 0.85 [208].

Optical devices that employ fluorescence for oral cancer detection are currently undergoing clinical trials. The Multispectral Digital Microscope (MDM) [180,209] obtains wide-field fluorescence images of the oral cavity under 365 nm, 405 nm, and 450 nm excitation, in addition to white-light reflectance and orthogonal polarization images. The FastEEM4 [210] excites tissue fluorescence at multiple wavelengths to measure spectrally-resolved fluorescence excitation-emission matrices (EEMs). (Previous versions of this instrument were employed in clinical trials for cervical cancer detection [211].) The PS2-Oral [212] incorporates an optical setup for fluorescence and reflectance imaging onto a surgical headlight system. A clinical trial employing the MDM, FastEEM4, and the PS2-Oral began in 2007 and is scheduled for completion in 2014 with an estimated enrollment of 200 patients [213].

7.3 Commercialized clinical fluorescence technologies

A number of clinically-compatible devices that employ fluorescence for disease detection are commercially available [214]. Typically, these devices provide tissue analysis using contrast from the tissue fluorescence measured at the surface, thereby assisting with visual diagnostic examination.

The VELscope (LED Dental Inc.) is a hand-held device (8.6” x 2.2” x 3.4”) that illuminates the oral mucosal tissue on the inside of the mouth with blue (400-460 nm [215,216]) light in order to detect malignant and pre-malignant lesions using endogenous tissue fluorescence. Normal tissue will emit fluorescent light that causes the surface of

the mouth to glow a green (> 480 nm [217]) color. However, cancerous and pre-cancerous tissue will not emit a notable amount of fluorescence, so the surfaces of diseased regions will appear darker than the surrounding normal tissue. The VELscope procedure can be easily incorporated into a dental exam, as the total time required to examine the patient with the device is only about 2 minutes. Recently, a study involving 620 patients [218] demonstrated that the VELscope was able to assist with detecting all 28 of the lesions that were not found during standard visual examination. However, the utility of this device is limited if the patient has inflamed tissue or if the device is interrogating a region with high pigmentation or prominent blood vessels near the tissue surface [215]. Under these circumstances, the fluorescence can be attenuated by tissue optical absorption from these features and the surface may appear dark even if there is no disease present.

The Identafi 3000 (DentalEZ) also uses tissue autofluorescence (similar to the VELscope) via a violet light source (Identafi). This device was approved by the FDA in 2009 for use in assisting with visual examinations of the oral cavity to detect cancerous and pre-cancerous lesions. It was also approved as a tool to assist with the identification of tumor margins during oral surgery. An ongoing clinical trial [219,220] is testing the ability of the instrument to identify oral neoplasia. This trial involves over 300 patients from two different comprehensive cancer centers that are independently researching the diagnostic accuracy of the device. The device employs 405 nm excitation to measure fluorescence images of stromal neovasculature and stromal breakdown, both associated with lesion growth. The device also employs white light for reflectance measurements and amber light (545 nm [219]) for improved detection of vasculature.

The WavSTAT optical biopsy system (SpectraScience) delivers laser light (410 nm [221]) onto human colon tissue via a fiber-optic probe incorporated into a pair of biopsy forceps inserted through the instrument channel of a colonoscope [222]. The detected endogenous fluorescence signal from the colon tissue is translated into a binary diagnostic result of "suspect" or "non-suspect" for the site of interest, thereby removing the need for the examiner to have expertise in analysis or interpretation of complex fluorescence spectra. Preliminary *in vivo* studies showed promise in distinguishing hyperplastic (benign, with no malignant potential) polyps and from adenomatous (pre-malignant) polyps in the colon [222].

The LUMA imaging system (SpectraScience) was approved by the FDA in 2006 for use by clinicians performing cervical cancer examinations, to determine if other regions of the cervix should be biopsied after colposcopy [214]. The device employs 337 nm laser light for fluorescence excitation and two flash lamps for reflectance [223]. The lamps and laser are coupled to a fiber-optic probe to deliver light to the tissue, and the system scans a region of 25 mm diameter, mapping a suspicious area of the cervix [223]. The scan takes roughly 12 seconds and the probe does not contact the tissue during this process [223]. In two randomized clinical trials, the true positive biopsy rate was found to increase by at least 25% when the LUMA device was employed along with colposcopy, and the corresponding increase in the false positive rate was only 4% [123,223].

7.4 Conclusions

Optical spectroscopy technologies can be applied to address a wide range of unmet clinical needs in tissue diagnostics. For successful clinical integration of these technologies, a clearly-defined "translational pipeline" should be further developed to

expedite the timeline from preliminary clinical trials to commercialization and adoption by the medical community. As additional optical technologies progress through the FDA approval process in the future, the impact of optical spectroscopy and imaging technologies on clinical patient care is expected to increase, directly addressing the need for cost-effective, real-time, objective, and non-invasive tissue diagnostics.

Chapter 8.
Conclusions and future directions

8.1 Major contributions of this dissertation

Optical technologies are commonly employed for non-invasive sensing of biological tissues because they are sensitive to tissue changes that may indicate disease status, including local changes in optical tissue properties, such as absorption and scattering, and microenvironment, such as binding status, temperature, and pH. The work presented in this dissertation describes the development, characterization, and employment of non-invasive optical sensing technologies, including steady-state diffuse reflectance, steady-state fluorescence, and time-resolved fluorescence, to address two primary clinical challenges: (1) improved detection of pancreatic disease state and (2) assessment of wound healing in implanted, *in situ* tissue-engineered constructs. First, we verified and validated a photon-tissue interaction (PTI) model that was then employed for the first ever characterization of *in vivo* reflectance spectra in a human pilot study with 6 patients. Results from PTI and ratiometric analysis models demonstrated quantitative similarity between the *in vivo* and corresponding *ex vivo* measurements. In a parallel study, we assessed the diagnostic utility of time-resolved fluorescence decays to classify human pancreatic disease *ex* and *in vivo*. Based on these promising results, we developed next generation, clinically-compatible wavelength-time matrix instrumentation to collect enhanced time-resolved fluorescence information from biological tissues and suitable for *in vivo* clinical use to study human tissues, such as those in the pancreas. Furthermore, we

employed diffuse reflectance spectroscopy to characterize wound healing in implanted tissue-engineered constructs *in situ*, distinguishing healthy from compromised constructs. These portable, hand-held, and sterilizable tools can be employed for real-time, quantitative sensing of biological tissues in clinics.

The major contribution of this dissertation can be summarized as follows:

Chapter 2

- We calibrated fitting parameters of two fiber-optic probes with a photon-tissue interaction (PTI) model. One probe was employed for proof-of-principle spectroscopic studies and a smaller second probe was employed for endoscopically-compatible measurements.
- We verified a PTI model to extract consistent optical scattering parameters from reflectance spectra measured from tissue-simulating phantoms with scattering parameters representative of pancreatic cell nuclei.
- We demonstrated that, with calibrated fiber-optic probes, the PTI model extracts consistent scattering properties when a measurement from a large, proof-of-principle probe is scaled to model a measurement from a smaller, endoscopically-compatible probe.
- We validated the ability of a PTI model to extract consistent biologically-relevant optical tissue parameters from *ex vivo* measurements of human tissue in the presence of varying hemoglobin concentrations, such as those that will occur during *in vivo* measurements.

Chapter 3

- We measured the first-ever, to our knowledge, *in vivo* optical spectra (steady-state fluorescence and reflectance) from human pancreatic tissues during open surgery.
- We showed that site-matched *in vivo* and *ex vivo* steady-state reflectance and fluorescence spectra qualitatively and quantitatively agreed. Quantitative similarity between *in* and *ex vivo* measurements was confirmed by comparing extracted parameters from ratiometric and PTI model analysis.
- We quantified differences between adenocarcinoma and normal tissues *in vivo*, confirming that diagnostic utility of optical spectroscopy is retained during *in vivo* measurements.
- We demonstrated that optical spectroscopy is a promising method for the improved diagnosis of pancreatic cancer *in vivo*.

Chapter 4

- We analyzed the first-ever, to our knowledge, time-resolved fluorescence decays collected from *ex vivo* human tissues with a rigorous classification algorithm that accounted for intrapatient correlations. Furthermore, we show the first-ever time-resolved fluorescence decays collected from *in vivo* human tissues.
- We employed an *ex vivo* fluorescence decay data set to train a rigorous classification algorithm for classification of *in vivo* measurements. Accurate diagnosis of *in vivo* measurements showed the clinical potential of *in vivo* time-resolved fluorescence measurements for improved detection of pancreatic disease.

- We demonstrate that time-resolved fluorescence decays collected with an endoscopically-compatible fiber-optic probe qualitatively agree with measurements from a larger, proof-of-principle fiber-optic probe.

Chapter 5

- We developed a novel, clinically-compatible, fiber-optic system that rapidly acquires fluorescence wavelength-time matrices (WTMs) with high signal-to-noise ratio. WTMs are information rich, three dimensional matrices containing both spectrally-resolved and time-resolved fluorescence information.
- We characterized the WTM system performance with measurements of fluorescence standards, reporting rapid, high signal-to-noise ratio measurements.
- We evaluated WTM system performance with measurements of tissue-simulating phantoms with varying scattering properties. WTM data contained characteristic contributions from increased scattering, consistent with diffusion theory predictions.

Chapter 6

- We employed diffuse reflectance spectroscopy (DRS), with a novel bevel-tipped fiber-optic probe, for label-free, non-invasive, and real-time assessment of thin implanted engineered oral tissues, preferentially interrogating the construct's top ~600 μm. Construct wound healing was assessed after 1 week and 3 weeks implantation in an *in situ* murine model.
- We validated DRS wound healing assessment by comparison with "gold standard" histological analysis, showing that healthiest *in situ* constructs had the

greatest relative amounts of hemoglobin absorption, hemoglobin oxygenation, and contributions from construct scattering.

Chapter 7

- We outlined the regulatory process and guidelines for successful clinical translation of optical spectroscopic instrumentation.

The work in this dissertation has been presented and documented as cited below:

Journal articles, book chapters, and manuscripts in preparation:

Chapter 1

Lloyd, W.R., Chen, L.-C., Wilson, R.H., and Mycek, M.-A.: "Clinical Fluorescence Detection" in Biomedical Technology and Devices Handbook, 2nd Edition, (D. Maitland and J. Moore, Ed.), Taylor & Francis (2013).

Lloyd, W.R., Chen, L.-C., and Mycek, M.-A.: "Fluorescence spectroscopy in regenerative medicine" in Optical Techniques in Regenerative Medicine, (S.P. Morgan, S.J. Matcher, F. Rose, Ed.), CRC Press (2013).

Chen, L.-C., **Lloyd, W.R.**, Change, C.-W., Sud, D., and Mycek, M.-A.: "Fluorescence Lifetime Imaging Microscopy for Quantitative Biological Imaging" in methods in Cell Biology - Digital Microscopy, 4th Edition, (G. Sluder and D.E. Wolf, Ed.), Elsevier (2013).

Chapter 2

Wilson, R.H.*, **Lloyd, W.R.***, Chandra, M., Chen, L.-C., Scheiman, J., Simeone, D., McKenna, B., and Mycek, M.-A., "Photon-tissue interaction model consistently distinguishes optical characteristics of human pancreatic disease," (in preparation). (*authors contributed equally to this work)

Wilson, R. H., Chandra, M., Chen, L.-C., **Lloyd, W. R.**, Scheiman, J., Simeone, D., Purdy, J., McKenna, B., and Mycek, M.-A., "Photon-tissue interaction model enables quantitative optical analysis of human pancreatic tissues," Opt. Express **18**, 21612-21621 (2010).

Chapter 3

Lloyd, W.R., Lee, S. Y., Wilson, R.H., Chandra, M., McKenna, B., Simeone, D., Scheiman, J., and Mycek, M.-A., "*In vivo* optical spectroscopy for improved detection of pancreatic adenocarcinoma: a feasibility study," Biomedical Optics Express (2014).

Lee, S. Y., **Lloyd, W.R.**, Chandra, M., Wilson, R.H., McKenna, B., Simeone, D., Scheiman, J., and Mycek, M.-A., "Characterizing human pancreatic cancer precursor using quantitative tissue optical spectroscopy," Biomedical Optics Express 4:2828-2834 (2013).

Chapter 4

Lloyd, W.R., Chandra, M., Wilson, R.H., Chen, L.-C., Lee, O., Taylor, J., Scheiman, J., Simeone, D., McKenna, B., and Mycek, M.-A., "Improved detection of pancreatic disease with time-resolved fluorescence spectroscopy," (in preparation).

Chapter 5

Lloyd, W. R., Wilson, R. H., Chang, C.-W., Gillispie, G. D., and Mycek, M.-A., "Instrumentation to rapidly acquire fluorescence wavelength-time matrices of biological tissues," Biomed. Opt. Express **1**, 574-586 (2010).

Chapter 6

Lloyd, W.R., Lee, S.Y., Elahi, S.F., Chen, L.-C., Kuo, S., Kim, H.M., Marcelo, C.L., Feinberg, S.E., and Mycek, M.-A., "Non-invasive assessment of implanted tissue-engineered construct success *in situ* by quantitative diffuse reflectance spectroscopy," (in preparation).

Chen, L.-C., **Lloyd, W.R.**, Kuo, S., Kim, H.M., Marcelo, C.L., Feinberg, S.E., and Mycek, M.-A., "Nonlinear optical molecular microscopy to noninvasively characterize tissue-engineered constructs and assess local viability," (in preparation).

Chapter 7

Lloyd, W.R., Chen, L.-C., Wilson, R.H., and Mycek, M.-A.: "Clinical Fluorescence Detection" in Biomedical Technology and Devices Handbook, 2nd Edition, (D. Maitland and J. Moore, Ed.), Taylor & Francis (2013).

Conference proceedings:

Chapter 2

Wilson, R.H., Chandra, M., **Lloyd, W.R.**, Chen, L.-C., Scheiman, J., Simeone, D., McKenna, B., and Mycek, M.-A., "Optical spectroscopy for quantitative sensing in human pancreatic tissues," Clinical and Biomedical Spectroscopy and Imaging II, Proceedings of SPIE-OSA Biomedical Optics, paper 8087-36 (2011).

Chapter 3

Wilson, R.H., Chandra, M., **Lloyd, W.R.**, Chen, L.-C., Scheiman, J., Simeone, D., McKenna, B., and Mycek, M.-A., "Optical spectroscopy for quantitative sensing in human pancreatic tissues," Clinical and Biomedical Spectroscopy and Imaging II, Proceedings of SPIE-OSA Biomedical Optics, paper 8087-36 (2011).

Wilson, R. H., Chandra, M., **Lloyd, W. R.**, Scheiman, J., Simeone, D., Purdy, J., McKenna, B., and Mycek, M.-A., "Quantitative optical spectroscopy for pancreatic cancer detection." OSA Biomedical Optics Topical Meeting (2010).

Chapter 4

Wilson, R.H., Chandra, M., **Lloyd, W.R.**, Chen, L.-C., Scheiman, J., Simeone, D., McKenna, B., and Mycek, M.-A., "Optical spectroscopy for quantitative sensing in human pancreatic tissues," Clinical and Biomedical Spectroscopy and Imaging II, Proceedings of SPIE-OSA Biomedical Optics, paper 8087-36 (2011).

Wilson, R. H., Chandra, M., **Lloyd, W. R.**, Scheiman, J., Simeone, D., Purdy, J., McKenna, B., and Mycek, M.-A., "Quantitative optical spectroscopy for pancreatic cancer detection." OSA Biomedical Optics Topical Meeting (2010).

Chapter 5

Lloyd, W.R., Wilson, R.H., Chen, L.-C., Gillispie, G.D., and Mycek, M.-A., "Fluorescence wavelength-time matrix acquisition for biomedical tissue diagnostics," Clinical and Biomedical Spectroscopy and Imaging II, Proceedings of SPIE-OSA Biomedical Optics, paper 8087-31 (2011).

Lloyd, W. R., Chang, C.-W., Wilson, R., Gillispie, G., and Mycek, M.-A., "Novel clinical technology for rapid detection of tissue fluorescence wavelength-time matrices." OSA Biomedical Optics Topical Meeting (2010).

Chang, C.-W., **Lloyd, W.R.**, Wilson, R., Gillispie, G. D., and Mycek, M.-A., "Clinically compatible instrumentation for accurate detection of fluorescence intensity and lifetime in turbid media." Proc. SPIE (2010).

Chapter 6

Chen, L.-C., **Lloyd, W.R.**, Chandra, M., Kuo, S., Kim, H.M., Marcelo, C.L., Feinberg, S.E., and Mycek, M.-A., "Label-free optical molecular imaging to assess engineered tissues," Optical Molecular Probes, Imaging, and Drug Delivery Topical Meeting, paper MT3C.7 (2013).

Lloyd, W.R., Chen, L.-C., Kuo, S., Marcelo, C.L., Feinberg, S.E., and Mycek, M.-A., "Fluorescence lifetime imaging microscopy (FLIM) studies of living primary human cells for applications in tissue regeneration," Multiphoton Microscopy in the Biomedical Sciences XII, Proceedings of SPIE, paper 8226-8 (2012).

Chen, L.-C., **Lloyd, W.R.**, Kuo, S., Marcelo, C.L., Feinberg, S.E., and Mycek, M.-A., "Label-free multiphoton fluorescence imaging monitors metabolism in living primary human cells used for tissue engineering," Imaging, Manipulation, and Analysis of Biomolecules, Cells, and Tissues X, Proceedings of SPIE, paper 8225-18 (2012).

Chen, L-C, **Lloyd, W.R.**, Wilson, R.H., Kuo, S., Marcelo, C.L., Feinberg, S.E., and Mycek, M.-A., "Nonlinear Optical Molecular Imaging Enables Metabolic Redox Sensing in Tissue-engineered Constructs," Molecular Imaging III, Proceedings of SPIE-OSA Biomedical Optics, paper 8089-18 (2011).

Wilson, R.H., Chen, L-C, **Lloyd, W.R.**, Kuo, S., Marcelo, C.L., Feinberg, S.E., and Mycek, M.-A., "Mesh-based Monte Carlo Code for Fluorescence Modeling in Complex Tissues with Irregular Boundaries," Novel Biophotonic Techniques and Applications. Proceedings of SPIE-OSA Biomedical Optics, paper 8090-14 (2011).

Chen, L.-C., **Lloyd, W.R.**, Chandra, M., Izumi, K., Kuo, S., Marcelo, C.L., Feinberg, S.E., and Mycek, M.-A., "Optical Redox Imaging of Endogenous

Contrast for Tissue-engineered Construct Viability," Optical Molecular Probes, Imaging, and Drug Delivery Topical Meeting (2011).

8.2 Future work

Combining time-resolved fluorescence, steady-state fluorescence, and steady-state reflectance data for improved detection of pancreatic disease

Building upon the human pancreatic classification analysis with time-resolved fluorescence data described in Chapter 4, extracted optical parameters from time-resolved fluorescence, steady-state fluorescence, and steady-state reflectance will be simultaneously employed for tissue classification with a classification algorithm developed from General Estimating Equations to account for intrapatient measurements. The complementary information measured with reflectance and fluorescence are expected to improve classification results compared to either reflectance or fluorescence parameters alone.

The following manuscript is in preparation:

R.H. Wilson*, W.R. Lloyd*, M. Chandra, L.-C. Chen, J. Scheiman, D. Simeone, B. McKenna, O.E. Lee, J.M.G. Taylor, and M.-A. Mycek, "Combined steady-state and time-resolved optical spectroscopy improves pancreatic disease diagnostics" (in preparation). (*denotes equal contribution)

Collecting wavelength-time matrices to classify pancreatic disease

Chapter 4 discussed the diagnostic utility of time-resolved fluorescence decays *ex* and *in vivo*. While adenocarcinoma was shown to be reliably assessed, broadband time-resolved fluorescence spectroscopy, steady-state fluorescence spectroscopy, and steady-state reflectance spectroscopy showed limited potential to reliably detect chronic pancreatitis. In this study, we employ our clinically-compatible WTM technology to improve detection of chronic pancreatitis.

Unified analysis of time-resolved fluorescence and steady-state fluorescence

Fluorescence measurements of pancreatic tissues were simultaneously collected in the steady-state and time-resolved domain. That is, emission photons from pancreatic tissue were simultaneously collected as steady-state and time-resolved data, with equivalence expected between each such pair of measurements. A model is being developed to compare the fluorescence contributions of endogenous tissue fluorophores in both data modalities. For broad-band time-resolved fluorescence, corrections will be made for detector sensitivity, fluorescence quantum yields, and non-uniform contributions of hemoglobin absorption.

Direct-Fit Photon-Tissue Interaction Model for Real-Time, Quantitative Analysis of Ex Vivo and In Vivo Data

Previously, a photon-tissue interaction model was developed based on scaling an *a priori* "canonical normal" to unknown tissue data. Here, a direct-fit model, developed by scaling an empirical steady-state reflectance equation, will be developed for real-time, quantitative analysis of pancreatic tissue data requiring no *a priori* information. The

direct-fit model will be evaluated on previously collected *ex vivo* and *in vivo* pancreatic data sets.

Effect of Modeled Scattering on a Photon-Tissue Interaction Model

Previously, a photon-tissue interaction model estimated tissue scattering as the linear combination of scattering from cell nuclei and collagen fibers, evaluated as spherical and cylindrical Mie scattering. In the last decade, numerous alternative models to the simplistic Mie scattering models have been proposed and validated. Here, alternative scattering models, including incorporation of power laws and wavelength-dependent phase functions and anisotropies to model scattering will be developed and compared to the Mie scattering model.

Validating Confidence Interval of Extracted Parameters from a Photon-Tissue Interaction Model

A photon-tissue interaction model extracts biophysically relevant optical tissue parameters from measured steady-state reflectance and fluorescence spectra, including contributions from tissue scattering parameters attributed to cell nuclei diameter and collagen fiber density. Here, a rigorous model will be developed to characterize the confidence intervals of extracted parameters and the subsequent impact on tissue classification.

Validating an Endoscopically-Compatible Fiber-Optic Probe

Previously, optical spectroscopy was employed to characterize pancreatic disease in human patients *ex vivo*, with subsequent *in vivo* verification with human patients

(Chapter 3). To be compatible with current clinical standard-of-care (*e.g.*, endoscopic ultrasound-guided fine needle aspiration), the fiber-optic probe diameter will need to be reduced at least three-fold (see time-resolved data in Chapter 4). This reduced fiber diameter will reduce the center-to-center spacing between excitation and emission fibers, and thus the average path length and number of scattering steps for reflectance and fluorescence photons. Here, we continue the validation discussed in Chapter 2 with more optical tissue scattering phantoms, *ex vivo* animal tissues, and with *ex vivo* human tissue data.

Photon-Tissue Interaction Modeling of Diffuse Reflectance Spectra from Tissue-Engineered Constructs

Chapter 6 discusses the ability of diffuse reflectance spectroscopy to distinguish control from stressed tissue-engineered constructs with ratiometric parameters developed from spectral intensities. Here, a photon-tissue interaction model, based on the models developed and employed for pancreatic tissue classification (see Chapter 2), will be employed to extract biophysically relevant optical tissue scattering and absorption parameters from diffuse reflectance spectra of constructs to distinguish healthy from compromised tissues.

Pre-Implantation Analysis of Tissue-Engineered Constructs

Chapter 6 discussed diffuse reflectance spectroscopy for post-implantation characterization of tissue-engineered constructs based on detecting variation in local tissue scattering and absorption. While tissue absorption changes primarily depend on neovascularization *in situ*, tissue scattering changes are attributed to the morphology of

keratin and living cell layers of a tissue-engineered construct that develop *in vitro* and continue development after implantation. From histology analysis, we found that pre-implantation control constructs have similar morphology (structured, dense keratin layer and a proliferated, living cell layer atop dermal equivalent) as those constructs implanted for 1 week. In a pilot study (N = 2 constructs, 1 control and 1 stressed), diffuse reflectance spectroscopy showed promise to characterize the differences of *in vitro* control and stressed constructs. This work will employ diffuse reflectance spectroscopy on an expanded construct set to distinguish healthy and compromised constructs *in situ*.

References

1. J.R. Lakowicz. Principles of Fluorescence Spectroscopy. 3rd ed. New York: Springer; 2006.
2. J.D. Pitts, M.-A. Mycek. Design and development of a rapid acquisition laser-based fluorometer with simultaneous spectral and temporal resolution. Rev Sci Instrum. 2001;72(7):3061-72
3. M. Chandra, R. H. Wilson, J. Scheiman, D. Simeone, B. McKenna, J. Purdy, M.-A. Mycek. Optical spectroscopy for clinical detection of pancreatic cancer. Proc SPIE. 2009;7368:73681G
4. T. J. Pfefer, D. Y. Paithankar, J. M. Poneros, K. T. Schomacker, N. S. Nishioka. Temporally and spectrally resolved fluorescence spectroscopy for the detection of high grade dysplasia in Barrett's esophagus. Laser Surg Med. 2003;32(1):10-6
5. M. Chandra, J. Scheiman, D. Simeone, B. McKenna, J. Purdy, M.-A. Mycek. Spectral areas and ratios classifier algorithm for pancreatic tissue classification using optical spectroscopy. J Biomed Opt. 2010;15(1):010514
6. M.-A. Mycek, K. Schomacker, N. Nishioka. Colonic polyp differentiation using time resolved autofluorescence spectroscopy. Gastrointest Endosc. 1998;48(4):390-4
7. Z. Volynskaya, A. S. Haka, K. L. Bechtel, M. Fitzmaurice, R. Shenk, N. Wang, J. Nazemi, R. R. Dasari, M. S. Feld. Diagnosing breast cancer using diffuse reflectance spectroscopy and intrinsic fluorescence spectroscopy. J Biomed Opt. 2008;13(2):024012
8. P. Uehlinger, T. Gabrecht, T. Glanzmann, J.-P. Ballini, A. Radu, S. Andrejevic, P. Monnier, G. Wagnières. *In vivo* time-resolved spectroscopy of the human bronchial early cancer autofluorescence. Journal of Biomedical Optics. 2009;14(2):024011
9. M.-A. Mycek, B. W. Pogue, editors. Handbook of Biomedical Fluorescence. New York: Marcel Dekker, Inc.; 2003.
10. M. H. Lee, J. A. Arcidiacono, A. M. Bilek, J. J. Wille, C. A. Hamill, K. M. Wonnacott, M. A. Wells, S. S. Oh. Considerations for tissue-engineered and regenerative medicine product development prior to clinical trials in the United States. Tissue Engineering Part B 2010;16(1):41-54
11. Michael B Wallace, Adam Wax, David N Roberts, Robert N Graf. Reflectance spectroscopy. Gastrointest Endosc Clin N Am. 2009;19(2):233-42
12. Nada N Boustany, Stephen A Boppart, Vadim Backman. Microscopic imaging and spectroscopy with scattered light. Annual review of biomedical engineering. 2010;12:285

13. G. Wagnieres, W. Star, B. Wilson. In vivo fluorescence spectroscopy and imaging for oncological applications. Photochem Photobiol. 1998;68(5):603-32

14. K. Vishwanath, M.-A. Mycek. Do fluorescence decays remitted from tissues accurately reflect intrinsic fluorophore lifetimes? Optics Letters. 2004;29(3):1512-4

15. Matthieu Zellweger. Fluorescence Spectroscopy of Exogenous, Exogenously-Induced and Endogenous Fluorophores for the Photodetection and Photodynamic Therapy of Cancer. Lausanne: Ecole Polytechnique Federale de Lausanne; 2000.

16. A. A. Heikal. Intracellular coenzymes as natural biomarkers for metabolic activities and mitochondrial anomalies. Biomark Med. 2010;4(2):241-63

17. Binil Starly, Anuja Choubey. Enabling sensor technologies for the quantitative evaluation of engineered tissue. Ann Biomed Eng. 2008;36(1):30-40

18. J. P. Celli, B. Q. Spring, I. Rizvi, C. L. Evans, K. S. Samkoe, S. Verma, B. W. Pogue, T. Hasan. Imaging and Photodynamic Therapy: Mechanisms, Monitoring, and Optimization. Chem Rev. 2010;110(5):2795-838

19. E. Kuwana, E. M. Sevick-Muraca. Fluorescence lifetime spectroscopy for pH sensing in scattering media. Anal Chem. 2003;75(16):4325-9

20. J. Q. Brown, K. Vishwanath, G. M. Palmer, N. Ramanujam. Advances in quantitative UV-visible spectroscopy for clinical and pre-clinical application in cancer. Current Opinion in Biotechnology. 2009;20(1):119-31

21. S. Andersson-Engels, J. Johansson, U. Stenram, K. Svanberg, S. Svanberg. Time-resolved laser-induced fluorescence spectroscopy for enhanced demarcation of human atherosclerotic plaques. Journal of Photochemistry and Photobiology B. 1990;4(4):363-9

22. N. Ramanujam. Fluorescence spectroscopy of neoplastic and non-neoplastic tissues. Neoplasia. 2000;2(1-2):89-117

23. R. H. Wilson, M. Chandra, L.-C. Chen, W. Lloyd, J. Scheiman, D. Simeone, J. Purdy, B. McKenna, M.-A. Mycek. Photon-tissue interaction model enables quantitative optical analysis of human pancreatic tissues. Optics Express. 2010;18(21):21612-21

24. W. Lloyd, R. H. Wilson, C.-W. Chang, G. D. Gillispie, M.-A. Mycek. Instrumentation to rapidly acquire fluorescence wavelength-time matrices of biological tissues. Biomedical Optics Express. 2010;1(2):574-86

25. Markolf H. Niemz. Laser-Tissue Interactions: Fundamentals and Applications. 3 ed. Germany: Springer; 2007.

26. X. Michalet, O. H. W. Siegmund, J. V. Vallerga, P. Jelinsky, J. E. Millaud, S. Weiss. Detectors for single-molecule fluorescence imaging and spectroscopy. J Mod Optic. 2007;54(2-3):239-81

27. M. Chandra, K. Vishwanath, G.D. Fichter, E. Liao, S.J. Hollister, M.-A. Mycek. Quantitative molecular sensing in biological tissues: an approach to non-invasive optical characterization. Optics Express. 2006;14(13):6157-71

28. C.A. Buhler, U. Graf. Multidimensional fluorescence spectroscopy using a streak camera based pulse florometer. Rev Sci Instrum. 1998;63(3):1512-8

29. P. Urayama, W. Zhong, J. A. Beamish, F. K. Minn, R. D. Sloboda, K. H. Dragnev, E. Dmitrovsky, M. A. Mycek. A UV-visible-NIR fluorescence lifetime imaging microscope for laser-based biological sensing with picosecond resolution. Appl Phys B-Lasers O. 2003;76(5):483-96

30. L. Marcu, J. A. Jo, Q. Y. Fang, T. Papaioannou, T. Reil, J. H. Qiao, J. D. Baker, J. A. Freischlag, M. C. Fishbein. Detection of rupture-prone atherosclerotic plaques by time-resolved laser-induced fluorescence spectroscopy. Atherosclerosis. 2009;204(1):156-64

31. M. Chandra, J. Scheiman, D. Heidt, D. Simeone, B. McKenna, M.-A. Mycek. Probing pancreatic disease using tissue optical spectroscopy. J Biomed Opt. 2007;12(6):060501

32. K. Vishwanath, M.-A. Mycek. Time-resolved photon migration in bi-layered tissue models. Optics Express. 2005;13(19):7466-82

33. K. Vishwanath, B.W. Pogue, M.-A. Mycek. Quantitative fluorescence lifetime spectroscopy in turbid media: comparison of theoretical, experimental and computational methods. Physics in Medicine and Biology. 2002;47:3387-405

34. R. Richards-Kortum, E. Sevick-Muraca. Quantitative optical spectroscopy for tissue diagnosis. Annu Rev Phys Chem. 1996;47:555-606

35. M. Chandra, R. H. Wilson, W.-L. Lo, K. Vishwanath, K. Izumi, S.E. Feinberg, M.-A. Mycek. Sensing metabolic activity in tissue engineered constructs. Proc SPIE. 2007;6628:66280B

36. W. F. Cheong, S. A. Prahl, A. J. Welch. A Review of the Optical-Properties of Biological Tissues. Ieee J Quantum Elect. 1990;26(12):2166-85

37. T. Bernas, J. P. Robinson, E. K. Asem, B. Rajwa. Loss of image quality in photobleaching during microscopic imaging of fluorescent probes bound to chromatin. J Biomed Opt. 2005;10(6):064015

38. B. W. Pogue, J. D. Pitts, M. A. Mycek, R. D. Sloboda, C. M. Wilmot, J. F. Brandsema, J. A. O'Hara. In vivo NADH fluorescence monitoring as an assay for cellular damage in photodynamic therapy. Photochem Photobiol. 2001;74(6):817-24

39. K. Rivoire, A. Nath, D. Cox, E. N. Atkinson, R. Richards-Kortum, M. Follen. The effects of repeated spectroscopic pressure measurements on fluorescence intensity in the cervix. Am J Obstet Gynecol. 2004;191(5):1606-17

40. Liang Lim, Narasimhan Rajaram, Brandon Nichols, James W. Tunnell, editors. Time Resolved Study of Probe Pressure Effects on Skin Fluorescence and Reflectance Spectroscopy Measurements. Biomedical Optics; 2010: OSA Technical Digest (CD).

41. R. Reif, M. S. Amorosino, K. W. Calabro, O. A'Amar, S. K. Singh, I. J. Bigio. Analysis of changes in reflectance measurements on biological tissues subjected to different probe pressures. Journal of Biomedical Optics. 2008;13(1):010502

42. J. Pitts, R. Sloboda, K. Dragnev, E. Dmitrovsky, M.-A. Mycek. Autofluorescence characteristics of immortalized and carcinogen-transformed human bronchial epithelial cells. Journal of Biomedical Optics. 2001;6(1):31-40

43. W. Zhong, M. Wu, C. W. Chang, K. A. Merrick, S. D. Merajver, M. A. Mycek. Picosecond-resolution fluorescence lifetime imaging microscopy: a useful tool for sensing molecular interactions in vivo via FRET. Optics Express. 2007;15(26):18220-35

44. G. M. Palmer, P. J. Keely, T. M. Breslin, N. Ramanujam. Autofluorescence spectroscopy of normal and malignant human breast cell lines. Photochem Photobiol. 2003;78(5):462-9

45. Q. Liu, T. Vo-Dinh. Spectral filtering modulation method for estimation of hemoglobin concentration and oxygenation based on a single fluorescence emission spectrum in tissue phantoms. Medical Physics. 2009;36(10):4819-29

46. S. Alberti, D. R. Parks, L. A. Herzenberg. A Single Laser Method for Subtraction of Cell Autofluorescence in Flow-Cytometry. Cytometry. 1987;8(2):114-9

47. K. Izumi, J. Song, S. E. Feinberg. Development of a tissue-engineered human oral mucosa: from the bench to the bed side. Cells Tissues Organs. 2004;176(1-3):134-52

48. B. Chance, B. Schoener, R. Oshino, F. Itshak, Y. Nakase. Oxidation-Reduction Ratio Studies of Mitochondria in Freeze-Trapped Samples - Nadh and Flavoprotein Fluorescence Signals. Journal of Biological Chemistry. 1979;254(11):4764-71

49. N. D. Kirkpatrick, J. B. Hoying, S. K. Botting, J. A. Weiss, U. Utzinger. In vitro model for endogenous optical signatures of collagen. Journal of Biomedical Optics. 2006;11(5):054021

50. C.-W. Chang, M. Wu, S. D. Merajver, M.-A. Mycek. Physiological fluorescence lifetime imaging microscopy improves Forster resonance energy transfer detection in living cells. J Biomed Opt. 2009;14(6):060502

51. Melissa C. Skala, Kristin M. Riching, Damian K. Bird, Annette Gendron-Fitzpatrick, Jens Eickhoff, Kevin W. Eliceiri, Patricia J. Keely, Nirmala Ramanujam. In vivo multiphoton fluorescence lifetime imaging of protein-bound and free nicotinamide adenine dinucleotide in normal and precancerous epithelia. Journal of Biomedical Optics. 2007;12(2):024014

52. H. D. Vishwasrao, A. A. Heikal, K. A. Kasischke, W. W. Webb. Conformational dependence of intracellular NADH on metabolic state revealed by associated fluorescence anisotropy. Journal of Biological Chemistry. 2005;280(26):25119-26

53. J. R. Lakowicz, G. Weber. Quenching of fluorescence by oxygen. A probe for structural fluctuations in macromolecules. Biochemistry. 1973;12(21):4161-70

54. D. Chorvat, A. Chorvatova. Multi-wavelength fluorescence lifetime spectroscopy: a new approach to the study of endogenous fluorescence in living cells and tissues. Laser Phys Lett. 2009;6(3):175-93

55. D. Elson, J. Requejo-Isidro, I. Munro, F. Reavell, J. Siegel, K. Suhling, P. Tadrous, R. Benninger, P. Lanigan, J. McGinty, C. Talbot, B. Treanor, S. Webb, A. Sandison, A. Wallace, D. Davis, J. Lever, M. Neil, D. Phillips, G. Stamp, P. French. Time-domain fluorescence lifetime imaging applied to biological tissue. Photoch Photobio Sci. 2004;3(8):795-801

56. Javier A. Jo, Qiyin Fang, Thanassis Papaioannou, J. Dennis Baker, Amir H. Dorafshar, Todd Reil, Jian-Hua Qiao, Michael C. Fishbein, Julie A. Freischlag, Laura Marcu. Laguerre-based method for analysis of time-resolved fluorescence data: application to in-vivo characterization and diagnosis of atherosclerotic lesions. Journal of Biomedical Optics. 2006;11(2):021004

57. M. A. Digman, V. R. Caiolfa, M. Zamai, E. Gratton. The phasor approach to fluorescence lifetime imaging analysis. Biophysical Journal. 2008;94(2):L14-L6

58. J. M. Muretta, A. Kyrychenko, A. S. Ladokhin, D. J. Kast, G. D. Gillispie, D. D. Thomas. High-performance time-resolved fluorescence by direct waveform recording. Rev Sci Instrum. 2010;81(10)

59. C. F. Zhu, E. S. Burnside, G. A. Sisney, L. R. Salkowski, J. M. Harter, B. Yu, N. Ramanujam. Fluorescence Spectroscopy: An Adjunct Diagnostic Tool to Image-Guided Core Needle Biopsy of the Breast. Ieee T Bio-Med Eng. 2009;56(10):2518-28

60. A. Sahar, T. Boubellouta, J. Lepetit, E. Dufour. Front-face fluorescence spectroscopy as a tool to classify seven bovine muscles according to their chemical and rheological characteristics. Meat Sci. 2009;83(4):672-7

61. R. S. Bradley, M. S. Thorniley. A review of attenuation correction techniques for tissue fluorescence. J R Soc Interface. 2006;3(6):1-13

62. A. Kim, M. Khurana, Y. Moriyama, B. C. Wilson. Quantification of in vivo fluorescence decoupled from the effects of tissue optical properties using fiber-optic spectroscopy measurements. Journal of Biomedical Optics. 2010;15(6):067006

63. R. H. Wilson, M.-A. Mycek. Models of light propagation in human tissue applied to cancer diagnostics. Technology in Cancer Research and Treatment. 2011;10:121-34

64. Urs Utzinger, Rebecca R. Richards-Kortum. Fiber optic probes for biomedical optical spectroscopy. Journal of Biomedical Optics. 2003;8(1):121-47

65. R. H. Wilson, L.-C. Chen, W. R. Lloyd, S. Kuo, C. L. Marcelo, S. E. Feinberg, M.-A. Mycek. Mesh-based Monte Carlo code for fluorescence modeling in complex tissues with irregular boundaries Proc SPIE. 2011

66. A. Kienle, M.S. Patterson. Improved solutions of the steady-state and the time-resolved diffusion equations for reflectance from a semi-infinite turbid medium. Journal of the Optical Society of America A. 1997;14(1):246-54

67. D. Yudovsky, L. Pilon. Modeling the local excitation fluence rate and fluorescence emission in absorbing and strongly scattering multilayered media. Appl Optics. 2010;49(31):6072-84

68. T.J. Pfefer, K.T. Schomacker, M.N. Ediger, N.S. Nishioka. Multiple-fiber probe design for fluorescence spectroscopy in tissue. Appl Optics. 2002;41(22):4712-21

69. K. Vishwanath, M.-A. Mycek, editors. Simulations of time-resolved autofluorescence decays in epithelial tissue for differing probe geometries. Biomedical Topical Meetings on CD-ROM; 2004: The Optical Society of America.

70. G. K. Bhowmick, N. Gautam, L. M. Gantayet. Design optimization of fiber optic probes for remote fluorescence spectroscopy. Opt Commun. 2009;282(14):2676-84

71. L. Wang, S.L. Jacques, L. Zheng. MCML - Monte Carlo modeling of photon transport in multi-layered tissues. Comput Meth Prog Bio. 1995;47:131-46

72. R. H. Wilson, M. Chandra, W.-L Lo, K. Vishwanath, K. Izumi, S. E. Feinberg, M.-A. Mycek. Simulated fiber-optic interrogation of autofluorescence from superficial layer of tissue-engineered construct. Frontiers in Optics 2008 Technical Digest (Optical Society of America). 2008:FTuK6

73. A. G. Mignani, F. Baldini. Biomedical sensors using optical fibres. Rep Prog Phys. 1996;59(1):1-28

74. C. Fang, D. Brokl, R. E. Brand, Y. Liu. Depth-selective fiber-optic probe for characterization of superficial tissue at a constant physical depth. Biomedical Optics Express. 2011;2(4):838-49

75. R. A. Schwarz, W. Gao, D. Daye, M. D. Williams, R. Richards-Kortum, A. M. Gillenwater. Autofluorescence and diffuse reflectance spectroscopy of oral epithelial tissue using a depth-sensitive fiber-optic probe. Appl Optics. 2008;47(6):825-34

76. J. Mo, W. Zheng, Z. Huang. Fiber-optic Raman probe couples ball lens for depth-selected Raman measurements of epithelial tissue. Biomedical Optics Express. 2010;1(1):17-30

77. T. J. Pfefer, K. T. Schomacker, M. N. Ediger, N. S. Nishioka. Light propagation in tissue during fluorescence spectroscopy with single-fiber probes. Ieee J Sel Top Quant. 2001;7(6):1004-12

78. R. A. Schwarz, D. Arifler, S. K. Chang, I. Pavlova, I. A. Hussain, V. Mack, B. Knight, R. Richards-Kortum, A. M. Gillenwater. Ball lens coupled fiber-optic probe for depth-resolved spectroscopy of epithelial tissue. Optics Letters. 2005;30(10):1159-61

79. L. T. Nieman, M. Jakovljevic, K. Sokolov. Compact beveled fiber optic probe design for enhanced depth discrimination in epithelial tissues. Optics Express. 2009;17(4):2780-96

80. C. Fang, D. Brokl, R. E. Brand, Y. Liu. Depth-selective fiber-optic probe for characterization of superficial tissue at a constant physical depth. Biomed Opt Express. 2011;2(4):838-49

81. U. Utzinger, R. Richards-Kortum. Fiber optic probes for biomedical optical spectroscopy. Journal of Biomedical Optics. 2003;8(1):121-47

82. T. J. Pfefer, L. S. Matchette, A. M. Ross, M.N. Ediger. Selective detection of fluorophore layers in turbid media: the role of fiber-optic probe design. Optics Letters. 2003;28(2):120-2

83. T. J. Pfefer, K. T. Schomacker, N. S. Nishioka. Effect of fiber optic probe design on fluorescent light propagation in tissue. Laser-Tissue Interaction Xii: Photochemical, Photothermal, and Photomechanical. 2001;2(14):410-6

84. Q. Liu, N. Ramanujam. Experimental proof of the feasibility of using an angled fiber-optic probe for depth-sensitive fluorescence spectroscopy of turbid media. Optics Letters. 2004;29(17):2034-6

85. M. C. Skala, G. M. Palmer, C. Zhu, Q. Liu, K. M. Vrotsos, C. L. Marshek-Stone, A. Gendron-Fitzpatrick, N. Ramanujam. Investigation of fiber-optic probe designs for optical spectroscopic diagnosis of epithelial pre-cancers. Lasers Surg Med. 2004;34(1):25-38

86. F. Jaillon, W. Zheng, Z. Huang. Beveled fiber-optic probe couples a ball lens for improving depth-resolved fluorescence measurements of layered tissue: Monte Carlo simulations. Physics in Medicine and Biology. 2008;53(4):937

87. L. C. Chen, W. R. Lloyd, S. Kuo, C. L. Marcelo, S. E. Feinberg, M. A. Mycek. Nonlinear optical molecular imaging enables metabolic redox sensing in tissue-engineered constructs. Proc Spie. 2011;8089

88. D. S. Gareau, P. R. Bargo, W. A. Horton, S. L. Jacques. Confocal fluorescence spectroscopy of subcutaneous cartilage expressing green fluorescent protein versus cutaneous collagen autofluorescence. Journal of Biomedical Optics. 2004;9(2):254-8

89. A. Pena, M. Strupler, T. Boulesteix, M. Schanne-Klein. Spectroscopic analysis of keratin endogenous signal for skin multiphoton microscopy. Opt Express. 2005;13(16):6268-74

90. T. Theodossiou, G.S. Rapti, V. Hovhannisyan, E. Georgiou, K. Politopoulos, D. Yova. Thermally Induced Irreversible Conformational Changes in Collagen Probed by Optical Second Harmonic Generation and Laser-Induced Fluorescence. Laser Surg Med. 2002;17:34-41

91. T. Kutsuna, M. Sato, M. Ishihara, K. S. Furukawa, T. Nagai, M. Kikuchi, T. Ushida, J. Mochida. Noninvasive Evaluation of Tissue-Engineered Cartilage with Time-Resolved Laser-Induced Fluorescence Spectroscopy. Tissue Eng Part C-Me. 2010;16(3):365-73

92. M. Ishihara, I. Bansaku, M. Sato, J. Mochida, M. Kikuchi. Multifunctional characterization of engineered cartilage using nano-pulsed laser. Ifmbe Proc. 2009;25(10):69-70

93. Charlie Schmidt. Early Detection Tools for Pancreatic Cancer. J Natl Cancer I. 2012;104(15):1117-8

94. G. Zonios, L.T. Perelman, V. Backman, R. Manoharan, M. Fitzmaurice, J.V. Dam, M.S. Feld. Diffuse reflectance spectroscopy of human adenomatous colon polyps *in vivo*. Appl Optics. 1999;38(31):6628-37

95. S. K. Chang, Y. N. Mirabal, E. N. Atkinson, D. Cox, A. Malpica, M. Follen, R. Richards-Kortum. Combined reflectance and fluorescence spectroscopy for in vivo detection of cervical pre-cancer. J Biomed Opt. 2005;10(2):024031

96. I. Georgakoudi, M.S. Feld. The combined use of fluorescence, reflectance, and light-scattering spectroscopy for evaluating dysplasia in Barrett's esophagus. Gastrointest Endosc Clin N Am. 2004;14(3):519-37

97. A.E. Cerussi, N. Shah, D. Hsiang, A. Durkin, J. Butler, B. J. Tromberg. In vivo absorption, scattering, and physiologic properties of 58 malignant breast tumors determined by broadband diffuse optical spectroscopy. J Biomed Opt. 2006;11(4):044005

98. Stephen C. Kanick, Cor van der Leest, Remco S. Djamin, Andre M. Janssens, Henk C. Hoogsteden, Henricus J. C. M. Sterenborg, Arjen Amelink, Joachim G. J. V. Aerts. Characterization of Mediastinal Lymph Node Physiology In Vivo by Optical Spectroscopy during Endoscopic Ultrasound-Guided Fine Needle Aspiration. Journal of Thoracic Oncology. 2010;5(7):981-7 10.1097/JTO.0b013e3181ddbc0e

99. G. O. Angheloiu, J. T. Arendt, M. G. Müller, A. S. Haka, I. Georgakoudi, J. T. Motz, O. R. Šćepanović, B. D. Kuban, J. Myles, F. Miller, E. A. Podrez, M. Fitzmaurice, J. R. Kramer, M. S. Feld. Intrinsic fluorescence and diffuse reflectance spectroscopy identify superficial foam cells in coronary plaques prone to erosion. Arteriosclerosis, Thrombosis, and Vascular Biology. 2006;26(7):1594-600

100. M. N. Kim, T. Durduran, S. Frangos, B. L. Edlow, E. M. Buckley, H. E. Moss, C. Zhou, G. Yu, R. Choe, E. Maloney-Wilensky, R. L. Wolf, M. S. Grady, J. H. Greenberg, J. M. Levine, A. G. Yodh, J. A. Detre, W. A. Kofke. Noninvasive measurement of cerebral blood flow and blood oxygenation using near-infrared and diffuse correlation spectroscopies in critically brain-injured adults. Neurocritical Care. 2010;12:173-80

101. R. H. Wilson, M. Chandra, J. Scheiman, D. Simeone, B. McKenna, J. Purdy, M.-A. Mycek. Optical spectroscopy detects histological hallmarks of pancreatic cancer. Optics Express. 2009;17:17502-16

102. M. Chandra, D. Heidt, D. Simeone, B. McKenna, J. Scheiman, M.-A. Mycek. Pancreatic tissue assessment using fluorescence and reflectance spectroscopy. Proc SPIE. 2007;6628:66281R

103. Gregory M. Palmer, Changfang Zhu, Tara M. Breslin, Fushen Xu, Kennedy W. Gilchrist, Nirmala Ramanujam. Monte Carlo-based inverse model for calculating

tissue optical properties. Part II: Application to breast cancer diagnosis. Appl Optics. 2006;45(5):1072-8

104. D. C. G. de Veld, M. Skurichina, M. J. H. Witjes, R. P. W. Duin, H. J. C. M. Sterenborg, J. L. N. Roodenburg. Autofluorescence and diffuse reflectance spectroscopy for oral oncology. Laser Surg Med. 2005;36:356-64

105. S. C. Kanick, C. van der Leest, J. G. J. V. Aerts, H. C. Hoogsteden, S. Kaščáková, H. J. C. M. Sterenborg, A. Amelink. Integration of single-fiber reflectance spectroscopy into ultrasound-guided endoscopic lung cancer staging of mediastinal lymph nodes J Biomed Opt. 2010;15(1):017004

106. A. C. Koong, V. K. Mehta, Q. T. Le, G. A. Fisher, D. J. Terris, J. M. Brown, A. J. Bastidas, M. Vierra. Pancreatic tumors show high levels of hypoxia. International Journal of Radiation Oncology, Biology, Physics. 2000;48(4):919-22

107. S. Kersting, R. Konopke, F. Kersting, A. Volk, M. Distler, H. Bergert, H.-D. Saeger, R. Grützmann, A. Bunk. Quantitative Perfusion Analysis of Transabdominal Contrast-Enhanced Ultrasonography of Pancreatic Masses and Carcinomas. Gastroenterology. 2009;137(6):1903-11

108. M. D. Keller, S. K. Majumder, M. C. Kelley, I. M. Meszoely, F. I. Boulos, G. M. Olivares, A. Mahadevan-Jansen. Autofluorescence and diffuse reflectance spectroscopy and spectral imaging for breast surgical margin analysis. Laser Surg Med. 2010;42:15-23

109. R. Reif, O. A'Amar, I. J. Bigio. Analytical model of light reflectance for extraction of the optical properties in small volumes of turbid media. Appl Optics. 2007;46(29):7317-28

110. L.T. Perelman, V. Backman, M. Wallace, G. Zonios, R. Manoharan, A. Nusrat, S. Shields, M. Seiler, C. Lima, T. Hamano, I. Itzkan, J. Van Dam, J.M. Crawford, M.S. Feld. Observation of periodic fine structure in reflectance from biological tissue: a new technique for measuring nuclear size distribution. Physical Review Letters. 1998;80(3):627-30

111. I. S. Saidi, S. L. Jacques, F. K. Tittel. Mie and Rayleigh Modeling of Visible-Light Scattering in Neonatal Skin. Appl Optics. 1995;34(31):7410-8

112. J. C. Finlay, T. H. Foster. Hemoglobin oxygen saturations in phantoms and in vivo from measurements of steady-state diffuse reflectance at a single, short source-detector separation. Medical Physics. 2004;31:1949-59.

113. R. L. P. van Veen, W. Verkruysse, H. J. C. M. Sterenborg. Diffuse-reflectance spectroscopy from 500 to 1060 nm by correction for inhomogeneously distributed absorbers. Optics Letters. 2002;27(4):246-8

114. T. Imamura, H. Iguchi, T. Manabe, G. Ohshio, T. Yoshimura, Z. H. Wang, H. Suwa, S. Ishigami, M. Imamura. Quantitative analysis of collagen and collagen subtypes I, III, and V in human pancreatic cancer, tumor-associated chronic pancreatitis, and alcoholic chronic pancreatitis. Pancreas. 1995;11(4):357-64

115. Cancer Facts & Figures 2013. American Cancer Society; 2013 [updated 2013; cited]; Available from: www.cancer.org.

116. Theresa Pluth Yeo, Ralph H. Hruban, Steven D. Leach, Robb E. Wilentz, Taylor A. Sohn, Scott E. Kern, Christine A. Iacobuzio-Donahue, Anirban Maitra, Michael Goggins, Marcia I. Canto, Ross A. Abrams, Daniel Laheru, Elizabeth M. Jaffee, Manuel Hidalgo, Charles J. Yeo. Pancreatic cancer. Current Problems in Cancer. 2002;26(4):176-275

117. A. Fritscher-Ravens, L. Brand, W. T. Knöfel, C. Bobrowski, T. Topalidis, F. Thonke, A. de Werth, N. Soehendra. Comparison of endoscopic ultrasound-guided fine needle aspiration for focal pancreatic lesions in patients with normal parenchyma and chronic pancreatitis. Am J Gastroenterol. 2002;97(11):2768-75

118. W. R. Lloyd, L.-C. Chen, R. H. Wilson, M.-A. Mycek. Biophotonics: Clinical Fluorescence Spectroscopy and Imaging. In: Moore JE, Maitland DJ, editors. Biomedical Technology and Devices Handbook, Second Edition2013.

119. S. K. Chang, N. Marin, M. Follen, R. Richards-Kortum. Model-based analysis of clinical fluorescence spectroscopy for *in vivo* detection of cervical intraepithelial dysplasia. J Biomed Opt. 2006;11(2):024008

120. Eric J Seibel, Teresa A Brentnall, Jason A Dominitz. New endoscopic and cytologic tools for cancer surveillance in the digestive tract. Gastrointest Endosc Clin N Am. 2009;19(2):299

121. P. A. Testoni, A. Mariani, B. Mangiavillano, P. G. Arcidiacono, S. Di Pietro, E. Masci. Intraductal optical coherence tomography for investigating main pancreatic duct strictures. Am J Gastroenterol. 2007;102(2):269-74

122. P. A. Testoni, B. Mangiavillano, L. Albarello, P. G. Arcidiacono, A. Mariani, E. Masci, C. Doglioni. Optical coherence tomography to detect epithelial lesions of the main pancreatic duct: an *ex vivo* study. Am J Gastroenterol. 2005;100(12):2777-83

123. Vani J Konda, Alexander Meining, Laith H Jamil, Marc Giovannini, Kenneth J Chang, Joo Ha Hwang, Michael B Wallace, Uzma D Siddiqui, Harry R Aslanian, Simon K Lo. An International, Multi-Center Trial on Needle-Based Confocal Laser Endomicroscopy (nCLE): Results From the In Vivo CLE Study in the Pancreas With Endosonography of Cystic Tumors (INSPECT). Gastroenterology. 2012;142(5):S-620-S-1

124. V. R. Kondepati, J. Zimmermann, M. Keese, J. Sturm, B. C. Manegold, J. Backhaus. Near-infrared fiber optic spectroscopy as a novel diagnostic tool for the detection of pancreatic cancer. J Biomed Opt. 2005;10(5):054016

125. H. Subramanian, P. Pradhan, Y. Liu, I. R. Capoglu, J. D. Rogers, H. K. Roy, R. E. Brand, V. Backman. Partial-wave microscopic spectroscopy detects subwavelength refractive index fluctuations: an application to cancer diagnosis. Opt Lett. 2009;34(4):518-20

126. W. Y. Hu, G. Zhao, C. Y. Wang, J. G. Zhang, L. Fu. Nonlinear Optical Microscopy for Histology of Fresh Normal and Cancerous Pancreatic Tissues. PLoS One. 2012;7(5)

127. Y. Liu, R. E. Brand, V. Turzhitsky, Y. L. Kim, H. K. Roy, N. Hasabou, C. Sturgis, D. Shah, C. Hall, V. Backman. Optical markers in duodenal mucosa predict the presence of pancreatic cancer. Clin Cancer Res. 2007;13(15 Pt 1):4392-9

128. V. Turzhitsky, Y. Liu, N. Hasabou, M. Goldberg, H. K. Roy, V. Backman, R. Brand. Investigating population risk factors of pancreatic cancer by evaluation of optical markers in the duodenal mucosa. Dis Markers. 2008;25(6):313-21

129. Daqing Piao, Kenneth E. Bartels, Russell G. Postier, G. Reed Holyoak, Jerry W. Ritchey. Toward transduodenal diffuse optical tomography of proximal pancreas. Optics Letters. 2013;38(20):4142-5

130. R. H. Wilson*, W. R. Lloyd*, M. Chandra, L.-C. Chen, J. Scheiman, D. Simeone, B. McKenna, M.-A. Mycek. Photon-tissue interaction model consistently distinguishes optical characteristics of human pancreatic disease. (submitted to J Biophotonics). 2013

131. Seung Yup Lee, William R Lloyd, Malavika Chandra, Robert H Wilson, Barbara McKenna, Diane Simeone, James Scheiman, Mary-Ann Mycek. Characterizing human pancreatic cancer precursor using quantitative tissue optical spectroscopy. Biomedical Optics Express. 2013;4(12):2828-34

132. Cancer Facts & Figures 2010. American Cancer Society; 2010 [updated 2010; cited]; Available from: www.cancer.org.

133. W. Hartwig, L. Schneider, M. K. Diener, F. Bergmann, M. W. Büchler, J. Werner. Preoperative tissue diagnosis for tumours of the pancreas. Br J Surg. 2009;96:5-20

134. P. V. Butte, Q. Fang, J. A. Jo, W. H. Yong, B. K. Pikul, Black. K. L., L. Marcu. Intraoperative delineation of primary brain tumors using time-resolved fluorescence spectroscopy. J Biomed Opt. 2010;15(2):027008

135. L. Marcu, J. A. Jo, P. V. Butte, W. H. Yong, B. K. Pikul, K. L. Black, R. C. Thompson. Fluorescence lifetime spectroscopy of glioblastoma multiforme. Photochem Photobiol. 2004;80:98-103

136. L. Marcu. Fluorescence lifetime in cardiovascular diagnostics J Biomed Opt. 2010;15:011106

137. J. Blackwell, K. M. Katika, L. Pilon, K. M. Dipple, S. R. Levin, A. Nouvong. *In vivo* time-resolved autofluorescence measurements to test for glycation of human skin. J Biomed Opt. 2008;13(1):014004

138. William R Lloyd, Robert H Wilson, Seung Yup Lee, Malavika Chandra, Barbara McKenna, Diane Simeone, James Scheiman, Mary-Ann Mycek. In vivo optical spectroscopy for improved detection of pancreatic adenocarcinoma: a feasibility study. Biomedical Optics Express. accepted

139. A. S. Dabir, C. A. Trivedi, Y. Ryu, P. Pande, J. A. Jo. Fully automated deconvolution method for on-line analysis of time-resolved fluorescence

spectroscopy data based on an iterative Laguerre expansion technique. J Biomed Opt. 2009;14:024030

140. Paritosh Pande, Javier A. Jo. Automated analysis of fluorescence lifetime imaging microscopy (FLIM) data based on the Laguerre deconvolution method. IEEE transactions on bio-medical engineering. 2011;58(1):172-81

141. J. A. Hanley, A. Negassa, M. D. deB. Eduardes, J. E. Forrester. Statistical Analysis of Correlated Data Using Generalized Estimating Equations: An Orientation Am J Epidemiol. 2003;157:364-75

142. M. A. Mycek, B. W. Pogue, Eds. Handbook of Biomedical Fluorescence. New York, New York: Marcel-Dekker Inc.; 2003.

143. Qiyin Fang, T. Papaioannou, J.A. Jo, R. Vaitha, K. Shastry, L. Marcu. Time-domain laser-induced fluorescence spectroscopy apparatus for clinical diagnostics. Rev Sci Instrum. 2004;75(1):151-62

144. Y. S. Fawzy, H. Zeng. Intrinsic fluorescence spectroscopy for endoscopic detection and localization of the endobronchial cancerous lesions J Biomed Opt. 2008;13:064022

145. W. H. Yong, P. V. Butte, B. K. Pikul, J. A. Jo, Q. Y. Fang, T. Papaioannou, Black. K. L., L. Marcu. Distinction of brain tissue, low grade and high grade glioma with time-resolved fluorescence spectroscopy. Front Biosci. 2006;11:1255-63

146. N. Lois, J. V. Forrester. Fundus Autofluorescence. Philadelphia: Lippincott Williams & Wilkins; 2009.

147. F. G. Holz, R. F. Spaide. Medical Retina: Focus on Retinal Imaging. Berlin: Springer-Verlag; 2010.

148. K. Vishwanath, W. Zhong, M. Close, M.-A. Mycek. Fluorescence quenching by polystyrene microspheres in UV-visible and NIR tissue-simulating phantoms. Optics Express. 2006;14:7776-88

149. A. J. Bystol, T. Thorstenson, A. D. Campiglia. Laser-induced multidimensional fluorescence spectroscopy in Shpol'skii matrixes for the analysis of polycyclic aromatic hydrocarbons in HPLC fractions and complex environmental extracts. Environmental Science & Technology. 2002;36(20):4424-9

150. A.J. Bystol, A.D. Campiglia, G.D. Gillispie. Laser-Induced Multidimensional Fluorescence Spectroscopy in Shpol'skii Matrices with a Fiber Optic Probe at Liquid Helium Temperature. Anal Chem. 2001;73(23):5762-70

151. A.J. Bystol, A.D. Campiglia, G.D. Gillispie. Time-resolved Laser Excited Shpol'skii Spectrometry with a Fiber Optic Probe and ICCD Camera. Appl Spectrosc. 2000;54(6):910-7

152. M. Raghavan, N. D. Sahar, R. H. Wilson, M.-A. Mycek, N. Pleshko, D. H. Kohn, M. D. Morris. Quantitative polarized Raman spectroscopy in highly turbid bone tissue J Biomed Opt. 2010;15:037001

153. S.A. Prahl, M.J.C. van Gemert, A.J. Welch. Determining the optical properties of turbid media by using the adding-doubling method. Appl Optics. 1993;32(4):559-68

154. Du Hai, Fuh Ru-Chun Amy, Li Junzhong, L. Andrew Corkan, S. Lindsey Jonathan. PhotochemCAD: A Computer-Aided Design and Research Tool in Photochemistry. Photochemistry and Photobiology. 1998;68(2):141-2

155. D. Magde, G. E. Rojas, P. G. Seybold. Solvent dependence of the fluorescence lifetimes of xanthene dyes. Photochem Photobiol. 1999;70(5):737-44

156. K. Izumi, S. E. Feinberg, A. Iida, M. Yoshizawa. Intraoral grafting of an *ex vivo* produced oral mucosa equivalent: a preliminary report. Int J Oral Maxillofac Surg. 2003;32(2):188-97

157. Joseph J Pancrazio, Fei Wang, Christine A Kelley. Enabling tools for tissue engineering. Biosensors and Bioelectronics. 2007;22(12):2803-11

158. Gerwen Lammers, Pauline DHM Verhaegen, Magda MW Ulrich, Joost Schalkwijk, Esther Middelkoop, Daniela Weiland, Suzan TM Nillesen, Toin H Van Kuppevelt, Willeke F Daamen. An overview of methods for the in vivo evaluation of tissue-engineered skin constructs. Tissue Engineering Part B: Reviews. 2010;17(1):33-55

159. L. C. Chen, W. R. Lloyd, S. Kuo, H.M. Kim, C. L. Marcelo, S. E. Feinberg, M. A. Mycek. Label-free nonlinear optical molecular microscopy non-invasively characterizes viability of engineered human tissue constructs. 2013, to submit

160. Alyssa A. Appel, Mark A. Anastasio, Jeffery C. Larson, Eric M. Brey. Imaging challenges in biomaterials and tissue engineering. Biomaterials. 2013;34(28):6615-30

161. Alexander Khmaladze, Arindam Ganguly, Shiuhyang Kuo, Mekhala Raghavan, Raghu Kainkaryam, Jacqueline H. Cole, Kenji Izumi, Cynthia L. Marcelo, Stephen E. Feinberg, Michael D. Morris. Tissue-engineered constructs of human oral mucosa examined by Raman spectroscopy. Tissue engineering Part C, Methods. 2013;19(4):299-306

162. Zohreh Izadifar, Dean Chapman, Daniel Chen. Computed tomography diffraction enhanced imaging for in situ visualization of tissue scaffolds implanted in cartilage. Tissue Engineering. 2013(ja)

163. CW Han, CR Chu, N Adachi, A Usas, FH Fu, J Huard, Y Pan. Analysis of rabbit articular cartilage repair after chondrocyte implantation using optical coherence tomography. Osteoarthritis and cartilage. 2003;11(2):111-21

164. C Mason, JF Markusen, MA Town, P Dunnill, RK Wang. Doppler optical coherence tomography for measuring flow in engineered tissue. Biosensors and Bioelectronics. 2004;20(3):414-23

165. Sean M White, Ryan Hingorani, Rajan PS Arora, Christopher CW Hughes, Steven C George, Bernard Choi. Longitudinal in vivo imaging to assess blood flow and oxygenation in implantable engineered tissues. Tissue Engineering Part C: Methods. 2012;18(9):697-709

166. Ingo Kutschka, Ian Y Chen, Theo Kofidis, Georges von Degenfeld, Ahmad Y Sheikh, Stephen L Hendry, Grant Hoyt, Jeremy Pearl, Helen M Blau, Sanjiv S Gambhir. In vivo optical bioluminescence imaging of collagen-supported cardiac cell grafts. The Journal of heart and lung transplantation. 2007;26(3):273-80

167. K. Izumi, S. E. Feinberg, H. Terashi, C. L. Marcelo. Evaluation of transplanted tissue-engineered oral mucosa equivalents in severe combined immunodeficient mice. Tissue Eng. 2003;9(1):163-74

168. Christine S. Mulvey, Kexiong Zhang, Wei-Han Bobby Liu, David J. Waxman, Irving J. Bigio. Wavelength-dependent backscattering measurements for quantitative monitoring of apoptosis, part 1: early and late spectral changes are indicative of the presence of apoptosis in cell cultures. Journal of Biomedical Optics. 2011;16(11):117001

169. Michael S Weingarten, Elisabeth S Papazoglou, Leonid Zubkov, Linda Zhu, Michael Neidrauer, Guy Savir, Kim Peace, John G Newby, Kambiz Pourrezaei. Correlation of near infrared absorption and diffuse reflectance spectroscopy scattering with tissue neovascularization and collagen concentration in a diabetic rat wound healing model. Wound Repair and Regeneration. 2008;16(2):234-42

170. Meghann Kaiser, Amr Yafi, Marianne Cinat, Bernard Choi, Anthony J. Durkin. Noninvasive assessment of burn wound severity using optical technology: A review of current and future modalities. Burns. 2011;37(3):377-86

171. Michael Neidrauer, ElisabethS Papazoglou. Optical Non-invasive Characterization of Chronic Wounds. In: Gefen A, editor. Bioengineering Research of Chronic Wounds: Springer Berlin Heidelberg; 2009. p. 381-404.

172. Michiko Yoshizawa, Takahiro Koyama, Taku Kojima, Hiroko Kato, Yukiko Ono, Chikara Saito. Keratinocytes of Tissue-Engineered Human Oral Mucosa Promote Re-Epithelialization After Intraoral Grafting in Athymic Mice. J Oral Maxil Surg. 2012;70(5):1199-214

173. Optical Absorption of Hemoglobin [database on the Internet]. Oregon Medical Laser Center. 1999. Available from: http://omlc.ogi.edu/spectra/hemoglobin/index.html.

174. Shiny Sara Thomas, Soumyakant Mohanty, J. L. Jayanthi, Jolly Mary Varughese, Anitha Balan, Narayanan Subhash. Clinical trial for detection of dental caries using laser-induced fluorescence ratio reference standard. Journal of Biomedical Optics. 2010;15(2):027001

175. S. G. Werner, H. E. Langer, S. Ohrndorf, M. Bahner, P. Schott, C. Schwenke, M. Schirner, H. Bastian, G. Lind-Albrecht, B. Kurtz, G. R. Burmester, M. Backhaus. Inflammation assessment in patients with arthritis using a novel in vivo fluorescence optical imaging technology. Ann Rheum Dis. 2011

176. G. Hundorfean, A. Agaimy, R. Atreya, J. Mudter, M. F. Neurath, H. Neumann. Confocal laser endomicroscopy for characterization of Crohn's disease-associated duodenitis. Endoscopy. 2012;44 Suppl 2 UCTN:E80

177. Ronald L. Kirschner. The Future of Medical Devices. Pharmaceutical and Biomedical Project Management in a Changing Global Environment: John Wiley & Sons, Inc.; 2010. p. 345-57.

178. Quan Liu. Role of optical spectroscopy using endogenous contrasts in clinical cancer diagnosis. World J Clin Oncol. 2011;2(1):50-63

179. Jeremy D. Meier, Hongtao Xie, Yang Sun, Yinghua Sun, Nisa Hatami, Brian Poirier, Laura Marcu, D. Gregory Farwell. Time-resolved laser-induced fluorescence spectroscopy as a diagnostic instrument in head and neck carcinoma. Otolaryngol Head Neck Surg. 2010;142(6):838-44

180. Darren Roblyer, Rebecca Richards-Kortum, Konstantin Sokolov, Adel K. El-Naggar, Michelle D. Williams, Cristina Kurachi, Ann M. Gillenwater. Multispectral optical imaging device for in vivo detection of oral neoplasia. Journal of Biomedical Optics. 2008;13(2):024019

181. Darrell S. Rigel, Julie Russak, Robert Friedman. The evolution of melanoma diagnosis: 25 years beyond the ABCDs. CA Cancer J Clin. 2010;60(5):301-16

182. P. A. A. De Beule, C. Dunsby, N. P. Galletly, G. W. Stamp, A. C. Chu, U. Anand, P. Anand, C. D. Benham, A. Naylor, P. M. W. French. A hyperspectral fluorescence lifetime probe for skin cancer diagnosis. Rev Sci Instrum. 2007;78(12):123101-7

183. Masao Fujiwara, Takahide Mizukami, Ayano Suzuki, Hidekazu Fukamizu. Sentinel lymph node detection in skin cancer patients using real-time fluorescence navigation with indocyanine green: preliminary experience. Journal of plastic, reconstructive & aesthetic surgery : JPRAS. 2009;62(10):e373-8

184. K. Konig, A. Ehlers, I. Riemann, S. Schenkl, R. Buckle, M. Kaatz. Clinical two-photon microendoscopy. Microsc Res Techniq. 2007;70(5):398-402

185. A. Poellinger, S. Burock, D. Grosenick, A. Hagen, L. Ludemann, F. Diekmann, F. Engelken, R. Macdonald, H. Rinneberg, P. M. Schlag. Breast cancer: early- and late-fluorescence near-infrared imaging with indocyanine green--a preliminary study. Radiology. 2011;258(2):409-16

186. Pramod V. Butte, Adam N. Mamelak, Miriam Nuno, Serguei I. Bannykh, Keith L. Black, Laura Marcu. Fluorescence lifetime spectroscopy for guided therapy of brain tumors. Neuroimage. 2011;54 Suppl 1:S125-35

187. Y. Kusunoki, F. Imamura, H. Uda, M. Mano, T. Horai. Early detection of lung cancer with laser-induced fluorescence endoscopy and spectrofluorometry. Chest. 2000;118(6):1776-82

188. M. Kobayashi, K. Shibuya, H. Hoshino, T. Fujisawa. Spectroscopic analysis of the autofluorescence from human bronchus using an ultraviolet laser diode. J Biomed Opt. 2002;7(4):603-8

189. B. Mayinger, M. Jordan, T. Horbach, W. Hohenberger, E. Hahn. Influence of collagen in endoscopic fluorescence spectroscopy for gastric cancer. Gastrointest Endosc. 2004;59(5):Ab172-Ab

190. B. Mayinger, M. Jordan, T. Horbach, P. Horner, C. Gerlach, S. Mueller, W. Hohenberger, E. G. Hahn. Evaluation of in vivo endoscopic autofluorescence spectroscopy in gastric cancer. Gastrointest Endosc. 2004;59(2):191-8

191. Jerome Boutet, Lionel Herve, Mathieu Debourdeau, Laurent Guyon, Philippe Peltie, Jean-Marc Dinten, Laurent Saroul, Francois Duboeuf, Didier Vray. Bimodal ultrasound and fluorescence approach for prostate cancer diagnosis. Journal of Biomedical Optics. 2009;14(6):064001

192. Gooitzen M. van Dam, George Themelis, Lucia M. A. Crane, Niels J. Harlaar, Rick G. Pleijhuis, Wendy Kelder, Athanasios Sarantopoulos, Johannes S. de Jong, Henriette J. G. Arts, Ate G. J. van der Zee, Joost Bart, Philip S. Low, Vasilis Ntziachristos. Intraoperative tumor-specific fluorescence imaging in ovarian cancer by folate receptor-[alpha] targeting: first in-human results. Nat Med. 2011;17(10):1315-9

193. A. A. A. Aarts, O. Srivannavit, K. D. Wise, E. Yoon, R. Puers, C. Van Hoof, H. P. Neves. Fabrication technique of a compressible biocompatible interconnect using a thin film transfer process. J Micromech Microeng. 2011;21(7):074012

194. J. Y. Lo, B. Yu, H. L. Fu, J. E. Bender, G. M. Palmer, T. F. Kuech, N. Ramanujam. A strategy for quantitative spectral imaging of tissue absorption and scattering using light emitting diodes and photodiodes. Optics Express. 2009;17(3):1372-84

195. Electro-optical Sensors for the In Vivo Detection of Cervical Cancer and its Precursors: Submission Guidance for an IDE/PMA, (1997).

196. Melissa B. Aldrich, Milton V. Marshall, Eva M. Sevick-Muraca, Greg Lanza, John Kotyk, Joseph Culver, Lihong V. Wang, Jashim Uddin, Brenda C. Crews, Lawrence J. Marnett, Joseph C. Liao, Chris Contag, James M. Crawford, Ken Wang, Bill Reisdorph, Henry Appelman, D. Kim Turgeon, Charles Meyer, Tom Wang. Seeing it through: translational validation of new medical imaging modalities. Biomed Opt Express. 2012;3(4):764-76

197. Kim Seong-Jin, Yoon Euisik. Label-Free CMOS Bio Sensor With On-Chip Noise Reduction Scheme for Real-Time Quantitative Monitoring of Biomolecules. Biomedical Circuits and Systems, IEEE Transactions on. 2012;6(3):189-96

198. M. L. Marcus, B. R. Biersach. Regulatory requirements for medical equipment. Instrumentation & Measurement Magazine, IEEE. 2003;6(4):23-9

199. William A. Rutala, David J. Weber. Disinfection and Sterilization in Health Care Facilities: What Clinicians Need to Know. Clinical Infectious Diseases. 2004;39(5):702-9

200. Guideline for Disinfection and Sterilization in Healthcare Facilities, 2008, (2008).

201. W. A. Rutala, M. F. Gergen, D. J. Weber. Disinfection of a probe used in ultrasound-guided prostate biopsy. Infect Cont Hosp Ep. 2007;28(8):916-9

202. FDA Clears New Automated Probe Disinfector. Infection Control Today; 2011 [updated 2011; cited 2012 April 20]; Available from:

http://www.infectioncontroltoday.com/news/2011/08/fda-clears-new-automated-probe-disinfector.aspx.

203. Quan Liu. Role of optical spectroscopy using endogenous contrasts in clinical cancer diagnosis. World J Clin Oncol. 2010;2(1):14

204. Jennifer L. Martin, Beverley J. Norris, Elizabeth Murphy, John A. Crowe. Medical device development: the challenge for ergonomics. Appl Ergon. 2008;39(3):271-83

205. ClinicalTrials.gov. A service of the U.S. National Institutes of Health; [cited]; Available from: clinicaltrials.gov.

206. Nicusor Iftimia, Sevdenur Cizginer, Vikram Deshpande, Martha Pitman, Servet Tatli, Nicolae-Adrian Iftimia, Daniel X Hammer, Mircea Mujat, Teoman Ustun, R Daniel Ferguson. Differentiation of pancreatic cysts with optical coherence tomography (OCT) imaging: an ex vivo pilot study. Biomedical Optics Express. 2011;2(8):2372-82

207. U.S. National Institutes of Health. Fluorescence and Reflectance Spectroscopy During Colposcopy in Detecting Cervical Intraepithelial Neoplasia and Dysplasia in Healthy Participants With a History of Normal Pap Smears. 2011 [updated 2011; cited 2012 May 31]; Available from: http://clinicaltrials.gov/ct2/show/NCT00084903?term=fluorescence&rank=11.

208. Choon-Kiat Ho, Jörg Kleeff, Helmut Friess, Markus W Büchler. Complications of pancreatic surgery. HPB. 2005;7(2):99-108

209. Sun Young Park, Tom Collier, Jesse Aaron, Mia Markey, Rebecca Richards-Kortum, Konstantin Sokolov, Nick Mackinnon, Calum MacAulay, Lezlee Coghlan, Andrea Milbourne, Michele Follen. Multispectral digital microscopy for in vivo monitoring of oral neoplasia in the hamster cheek pouch model of carcinogenesis. Opt Express. 2005;13(3):749-62

210. J. Adrian Freeberg, Dan M. Serachitopol, Nick McKinnon, Roderick Price, E. Neely Atkinson, Dennis D. Cox, Calum MacAulay, Rebecca Richards-Kortum, Michele Follen, Brian Pikkula. Fluorescence and reflectance device variability throughout the progression of a phase II clinical trial to detect and screen for cervical neoplasia using a fiber optic probe. Journal of Biomedical Optics. 2007;12(3):034015

211. Y. Maeda, D. Hirasawa, N. Fujita, T. Obana, T. Sugawara, T. Ohira, Y. Harada, T. Yamagata, K. Suzuki, Y. Koike, J. Kusaka, M. Tanaka, Y. Noda. A prospective, randomized, double-blind, controlled trial on the efficacy of carbon dioxide insufflation in gastric endoscopic submucosal dissection. Endoscopy. 2013;45(5):335-41

212. Mohammed Rahman, Pankaj Chaturvedi, Ann M. Gillenwater, Rebecca Richards-Kortum. Low-cost, multimodal, portable screening system for early detection of oral cancer. Journal of Biomedical Optics. 2008;13(3):030502

213. Treatment of Pancreatic Cancer. 2013 [updated 2013; cited 2013 June 19]; Available from: pancreasfoundation.org.

214. US Food and Drug Administration. Medical Devices - Recently-Approved Devices. 2012 [updated 2012 4/1/2012; cited]; Available from: http://www.fda.gov/MedicalDevices/ProductsandMedicalProcedures/DeviceApprovalsandClearances/Recently-ApprovedDevices/default.htm.

215. Benjamin D. Smith, Grace L. Smith, Arti Hurria, Gabriel N. Hortobagyi, Thomas A. Buchholz. Future of Cancer Incidence in the United States: Burdens Upon an Aging, Changing Nation. Journal of Clinical Oncology. 2009;27(17):2758-65

216. Thomas C. Kwee, Taro Takahara, Reiji Ochiai, Dow-Mu Koh, Yoshiharu Ohno, Katsuyuki Nakanishi, Tetsu Niwa, Thomas L. Chenevert, Peter R. Luijten, Abass Alavi. Complementary roles of whole-body diffusion-weighted MRI and 18F-FDG PET: the state of the art and potential applications. Journal of nuclear medicine : official publication, Society of Nuclear Medicine. 2010;51(10):1549-58

217. Oh Hyoung-Seok, Taeksang Song, Yoon Euisik, Choong Kim, x, Ki. A power-efficient injection-locked class-E power amplifier for wireless sensor network. Microwave and Wireless Components Letters, IEEE. 2006;16(4):173-5

218. Edmond L. Truelove, David Dean, Samuel Maltby, Matthew Griffith, Kimberly Huggins, Mickealla Griffith, Stuart Taylor. Narrow band (light) imaging of oral mucosa in routine dental patients. Part I: Assessment of value in detection of mucosal changes. Gen Dent. 2011;59(4):281-9; quiz 90-1, 319-20

219. Pierre Lane, Michele Follen, Calum MacAulay. Has Fluorescence Spectroscopy Come of Age? A Case Series of Oral Precancers and Cancers Using White Light, Fluorescent Light at 405 nm, and Reflected Light at 545 nm Using the Trimira Identafi 3000. Gender Medicine. 2012;9(1, Supplement):S25-S35

220. Pierre Lane, Sylvia Lam, Michele Follen, Calum MacAulay. Oral Fluorescence Imaging Using 405-nm Excitation, Aiding the Discrimination of Cancers and Precancers by Identifying Changes in Collagen and Elastic Breakdown and Neovascularization in the Underlying Stroma. Gender Medicine. 2012;9(1, Supplement):S78-S82.e8

221. Hiroyuki Isayama, Yousuke Nakai, Peter V Draganov. The role of Endoscopic Ultrasound (EUS) in the management of patients with pancreatic cancer: now bigger than ever. Journal of gastrointestinal oncology. 2013;4(2):121

222. MohamadA Eloubeidi, Shyam Varadarajulu, Shilpa Desai, Rhett Shirley, MartinJ Heslin, Mohit Mehra, JuanP Arnoletti, Isam Eltoum, CharlesM Wilcox, SelwynM Vickers. A Prospective Evaluation of an Algorithm Incorporating Routine Preoperative Endoscopic Ultrasound-Guided Fine Needle Aspiration in Suspected Pancreatic Cancer. J Gastrointest Surg. 2007;11(7):813-9

223. James E. Kendrick, Warner K. Huh, Ronald D. Alvarez. LUMA Cervical Imaging System. Expert Review of Medical Devices. 2007;4(2):121-9